UNIVERSITY OF OKLAHOMA

GRADUATE COLLEGE

SEM INVESTIGATION OF THE FRACTURE NETWORK (STIMULATED RESERVOIR VOLUME) INDUCED BY HYDRAULIC FRACTURING

A THESIS

SUBMITTED TO THE GRADUATE FACULTY

In partial fulfillment of the requirements for the

Degree of

MASTER OF SCIENCE

By

CHRISTOPHER W. RATZLAFF
Norman, Oklahoma
2018

SEM INVESTIGATION OF THE FRACTURE NETWORK (STIMULATED RESERVOIR VOLUME) INDUCED BY HYDRAULIC FRACTURING

A THESIS APPROVED FOR THE
MEWBOURNE SCHOOL OF PETROLEUM AND GEOLOGICAL ENGINEERING

BY

Dr. Carl Sondergeld, Chair

Dr. Chandra Rai

Dr. Mark Curtis

Dr. Deepak Devegowda

Dedicated to
My Professors, Family, and Friends

Acknowledgements

I would like to thank Dr. Carl Sondergeld and Dr. Chandra Rai for the opportunity to obtain a Petroleum Engineering degree while performing state-of-the-art research. They have tested my knowledge and pushed my ability further than I knew possible. Combined with constant support and generosity, they have molded me into the professional I needed to become and allowed me to receive a job with BP. Some of their courses such as Rock Properties, Seismic Reservoir Modeling, and Well Logs were the toughest, yet most rewarding classes I have taken and prepared me for my future career as a petrophysicist. If it was not for the risk they took, by accepting a geologist into the petroleum engineering graduate department, I surely would not have the amazing career that has been laid out before me. Thank you for allowing me to be a part of your team.

I would also like to thank Dr. Mark Curtis, for always being patient and showing kindness throughout the years. Dr. Curtis answered my questions without hesitation or judgment. He has helped me with all my experiments and raised me in SEM. Dr. Curtis displayed peace throughout the storm.

I would also like to thank all my IC^3 colleagues, especially Jeremy Jernigen and Mikki Langevin for taking time out of their day to answer my questions and aid in laboratory experiments, Saurabh for being my friend and partner in the lab while growing together academically, and Sidi for always understanding the situation and being an awesome office mate.

Finally, I would like to thank my parents, Mike and Debbie Ratzlaff, for their constant support, understanding, and patience, and my siblings, Jonathan and Andrea

Ratzlaff, who were always there to take me out of the academic world to have a little bit of fun.

Table of Contents

List of Tables

List of Figures

Abstract

Tight formations often have an ultra-low permeability that prohibits fluid migration from the reservoir. To counter this issue, large fracture networks are created to connect pore space and increase permeability. The total volume created by hydraulic fracturing is the stimulated reservoir volume (SRV) and is used as a correlation parameter for well performance and to quantify the fracture network **(Mayerhofer et al., 2010).** The uncertainty that arises in the dimensions of SRV is caused mainly by the complexity of the fracture network. On a field scale, fractures are modeled using methods such as PKN-C and P-3D-C, but these models only take the primary fractures into consideration, which dismisses the secondary fracture network entirely. This research illustrates that secondary microfractures in the elastic zone can triple the amount of stimulated area and pore connections within a reservoir. This is made possible by a constant supply of energy pulsating around the primary fracture during propagation. This pressure wave has enough energy to create a large fracture network that acts to connect pores to the primary fracture. As the demand for reservoir stimulation increases, efforts are being directed towards quantifying microfractures to see how they impact reservoir production.

In this work, scanning electron microscopy (SEM) analysis is used to study hydraulically fractured Tennessee sandstone, Marcellus shale, and pyrophyllite. A series of high-resolution images were taken to investigate microfractures and their contribution to SRV. A total of 3 cores, 9 plugs, and 25 samples were prepared for SEM analysis. Over 75,000 high-resolution images were recorded from the primary and secondary fracture networks to extract statistics such as fracture density, distribution, orientation, symmetry, length, width, mechanical twinning, crystal orientations, and stimulated reservoir area

(SRA). In addition to SEM analysis, X-ray, confocal, and petrophysical measurements were performed as well.

Results show that microfractures have a large impact on the reservoir by increasing the total fractured volume by 25-fold and tripling the connected pore space. By propagating in a direction perpendicular to the primary fracture, secondary fractures act as a means of connecting micropores that were originally isolated. The fracture tip poses interesting findings by increasing the SRV, which suggests a change in physics in the elastic/plastic transition of a terminating fracture. It was further found that primary fractures with low velocities create larger SRV’s while the termination zone creates the largest SRV. This indicates that a start-stop pumping process during hydraulic fracturing would be most beneficial. Hydraulic fracturing was further found to induce Dauphiné twins in quartz crystals while also changing the orientation of grains during fracture propagation. These crystallographic alterations aid in fracture propagation by causing slip and changing plane orientations. Shale and pyrophyllite analysis provide insight on fracture morphology in unconventional formations. It was found that secondary fracture networks significantly decrease in unconventional reservoirs, but the complexity of each secondary fracture is far greater. A high number of tertiary nanofractures are stimulated around the primary and secondary fractures creating micro damage zones. Furthermore, the fracture length and width consistently increase from the Tennessee sandstone, to Marcellus shale, to pyrophyllite.

Chapter 1: Introduction

1.1 Motivation and Problem Statement

In the last 20 years, tight reservoirs and organic shales have emerged as a major source of production in the United States. Prior to hydraulic fracture stimulation, economic production was impossible due to naturally ultra-low permeabilities and porosities. Combining new technology such as multi-stage hydraulic fracturing and horizontal drilling has made tight plays accessible and economical. Today, nearly 16 trillion cubic feet (Tcf) of natural gas is produced from shale and tight oil resources in the United States that is attributed to hydraulic fracturing **(EIA, 2018).**

Hydraulic fracturing is implemented into plays such as shales, tight sands, carbonates, and coalbeds. **Fig. 1** and **2** illustrate maps of the U.S major shale and tight gas plays in the lower 48 states, while **Fig. 3** shows the north Alaskan oil and gas field that is home to the 10th biggest natural gas field in the United States (containing 45 Tcf), and the 3rd largest oil field (containing 25 billion barrels (Gbbl)) **(AOGA, 2018; Wilkinson, 2017)**. In recent years, additional plays have been discovered in the Alaskan region such as the ‘Tulimaniq’, and ‘Horseshoe’, which are expected to carry a combined 12 billion barrels of oil but will require large stimulation efforts **(Montgomery, 2017)**. New plays such as these assure the constant need for research and development in reservoir stimulation.

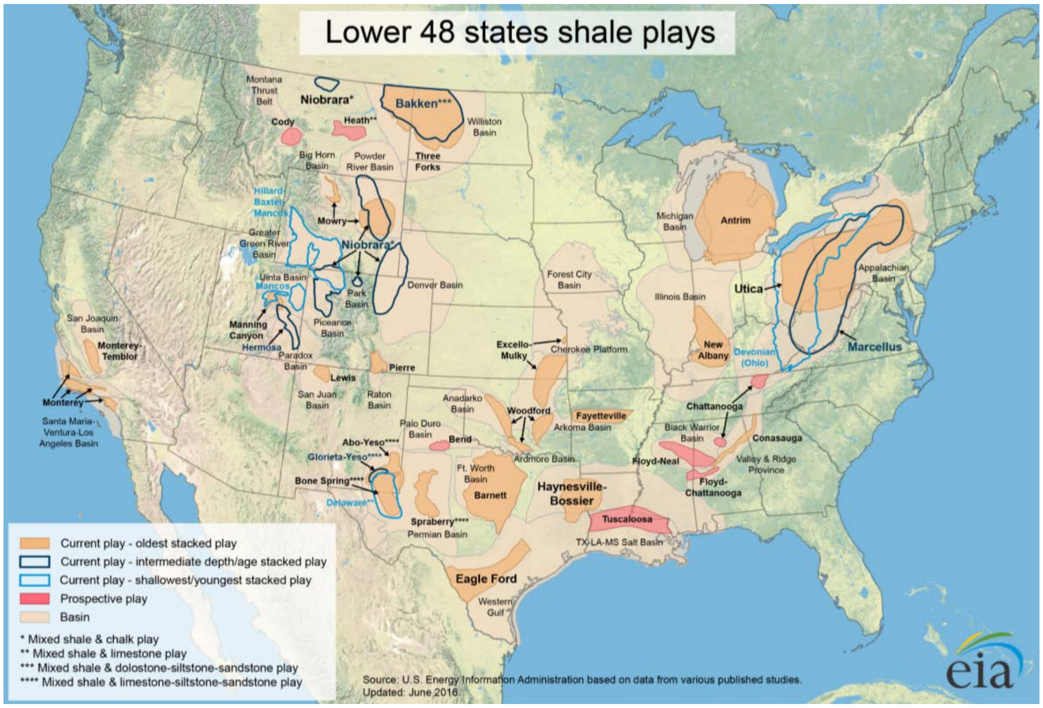

Figure 1: Map of the U.S. major shale plays in the lower 48 (EIA, 2016).

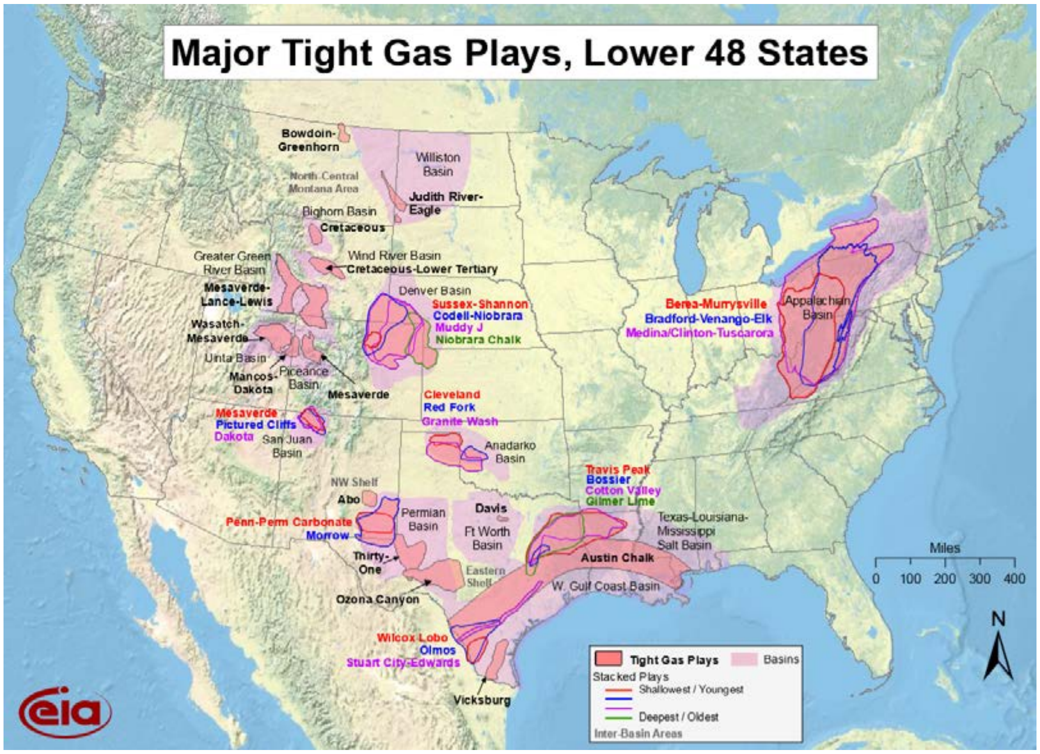

Figure 2: Map of the U.S. major tight gas plays in the lower 48 states (EIA, 2010)

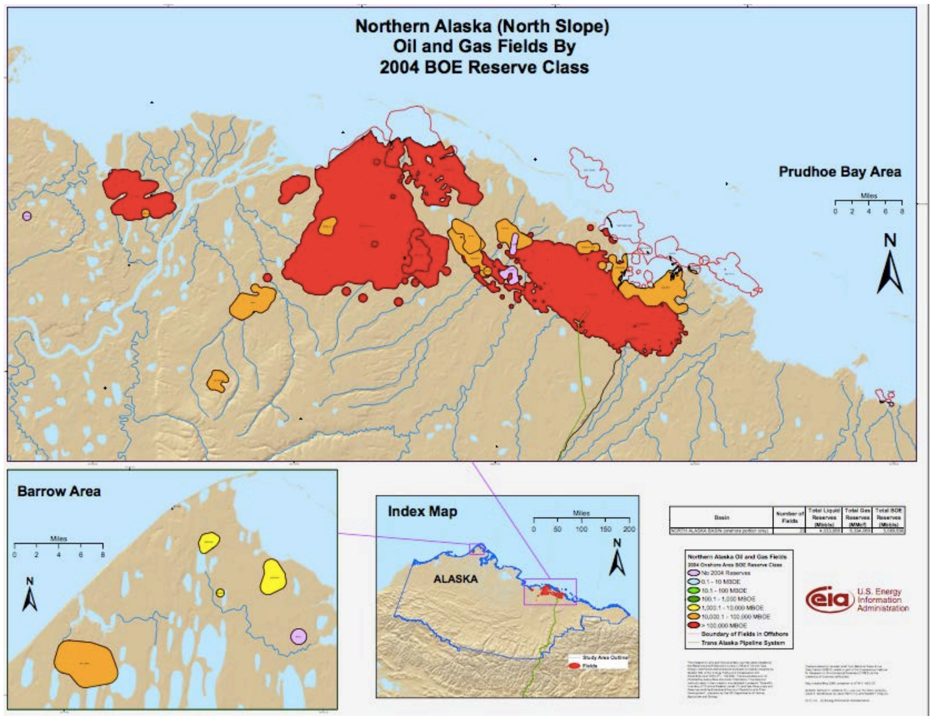

Figure 3: Map of the northern Alaska oil and gas fields (North Slope) by 2004 BOE reserve class (EIA, 2008)

Hydraulic fracturing is implemented to connect pore networks and increase the permeability of a reservoir to allow fluid to flow. The lower the permeability, the higher the cost of extraction due to required stimulation. One method to diagnose the stimulation productivity is by determining the stimulated reservoir volume (SRV). SRV is a measure of the total amount of connected volume created by hydraulic fracturing. This measurement can provide a correlation parameter for performance and completions, making the actual value of SRV very important **(Mayerhofer et al., 2010**). Two common field methods for determining SRV are 3-D microseismic and fluid injection, which map SRV based on acoustic emission analysis and fluid loss. The problem with these methods is the lack of precision, which results in a severe underestimate of the true SRV potential. Secondary microfractures are fractures that branch off the primary fracture and provide secondary stimulation for the reservoir. Commonly overlooked, secondary microfractures can play a significant role in SRV. To understand the microfracture network, it is necessary to use a powerful microscope that permits micron resolution but still analyzes a large enough surface area to prove reliable. It has been seen that optical and scanning acoustic microscopy can provide the field of view needed but does not deliver adequate resolution **(Prasad et al., 2002; Prasad et al., 2009; Bocangel et al., 2013; Ko et al., 2017)**. On the other hand, scanning electron microscopy (SEM) permits high-resolution imaging but suffers in observing an adequate surface size. This problem has been overcome by a new software that allows a mosaic of high-resolution images to be stitched together to expand the field of view. This method allows high-resolution images from SEM combined with a greater area of study.

Observational and statistical work has previously been accomplished in fracture analysis **(Entov et al., 2007; Dong, 2008; Pouya et al., 2014; Varfolomeev et al., 2016)** but many of these works were performed on large areas of interest (millimeter to feet scale) and suffer significant uncertainty on the micro scale. SEM analysis has also been performed, specifically in the industrial engineering, physics, geology, and petroleum engineering departments **(Kranz, 1983; Wong et al., 1989; Blochwitz and Tirschler, 2005; Wei and Yongming, 2011)** but their focus has remained on the primary fracture network. Thus, determining the effect of the secondary fracture network and microscopic alterations associated with hydraulic fracturing would introduce a more accurate characterization of SRV and generate a better understanding of induced permeability and flow networks **(Bhagat et al., 2012; El Monier, 2016)**.

1.2 Scope of the Thesis

The focus of this thesis is to determine the secondary fracture statistics and possible crystallographic effects due to hydraulic fracturing using high-resolution SEM imaging. Analysis is performed in the elastic and plastic zones associated with the primary fracture and the fracture tip. A comparison is made illustrating the similarities and differences between the plastic and elastic zones and how they relate to previous studies. Crystallographic effects are studied to determine grain misorientation and the possibility of inducing twins during hydraulic fracturing. Some of the statistics that will be shown are secondary fracture quantity, density, spatial distribution, orientation, length, width, and SRV. In addition, geological observations and energy distributions associated with linear elastic and plastic fracture mechanics are discussed. X-ray, confocal, and petrophysical measurements were also performed to support SEM observations.

The motivation for this thesis is to understand the secondary fracture network and microscopic changes associated with hydraulic fracturing in Tennessee sandstone, Marcellus shale, and pyrophyllite. These topics have long been overlooked due to the difficulty of analysis and the inability to accurately map the effects on a large scale. However, these components cannot be disregarded due to their ability to connect pores and increase SRV. In addition, the ability for the hydraulic fracture to alter the orientation of surrounding grains and possibly produce quartz twins would control the fracture direction, propagation, and termination, while also changing the fracture plane orientation, allowing further slip to occur and increasing fracture length.

By analyzing the induced microfracture statistics and crystallographic effects, more accurate fracture patterns and SRV models can be created.

1.3 Organization of the Thesis

This thesis is presented into five chapters and is organized as follows

- Chapter 2 introduces the background research undertaken for this thesis. It includes a brief literature review on fracture mechanics, microfracture statistics, and pressure induced Dauphiné twinning.
- Chapter 3 reviews the equipment, methodologies, and experimental procedures for sample characterization, hydraulic fracturing, and SEM analysis.
- Chapter 4 contains the results acquired from SEM analysis as well as discussion.
- Chapter 5 ends with conclusions and a review of the most significant findings.

Chapter 2: Background Research and Literature Review

2.1 Fracture Mechanics

2.1.1 Reservoir Stimulation

Hydraulic fracturing is a well stimulation technique that involves the injection of fluids into a formation at a rate sufficient to exceed the breakdown pressure of a formation. Once injection has ended, pressures begin to subside and the fracture closes. Proppants are used with the injection fluid to keep the fractures open and to maintain fluid migration (**Lindley, 2011).** Hydraulic fracturing is performed to remediate damage around the wellbore, improve well productivity, and to alter the fluid flow patterns of the reservoir **(Damani, 2013).** Diverters are commonly used in fracture designs to redirect the injection fluids to designated locations. The ability to divert proppant into isolated reservoir zones or new pockets is considered one of the key components to hydraulic fracture success **(Strother et al., 2013)**. After fracture completion, factors such as pressure drop, compaction, formation creep, stress, proppant crushing, embedment, and pore plugging start to decrease production and a well can be evaluated for a refracture job. Refracturing is particularly economical due to its ability to create new fractures, restore conductivity, eliminate blockages, enhance depleted reservoir pressures, and reorient fracture angles that could potentially access a new reservoir **(Jacobs, 2014 and 2015).** Fracture networks not only provide an increased permeability for fluid flow but also access portions of a reservoir not yet connected. Understanding hydraulic fracture networks could lead to more economical fracture designs.

2.1.2 Historical Development of Fracture Analysis

A British physicist named Alan Arnold Griffith (1920) illustrated the energy-based analysis of cracks. Griffith conducted research on glass and metal sheets to understand the failure strength of materials. He determined that a material would fail at a much lower stress than the theoretical fracture strength E/10 **(Dieter, 1988)**, where E is Young's modulus, due to the stress amplification caused by elliptical microcracks within the material. He found that the weakening of material due to cracks could be treated as an equilibrium problem where the energy needed to create crack surfaces could be associated with the increase of surface energy **(Ceriolo and Di Tommaso, 1998)**. Griffith was the first to demonstrate propagation criterion for an elliptical crack in an elastic plate.

$$\sigma^2 \geq 2\gamma E/\pi\alpha \tag{2.1}$$

$$2\gamma = G \tag{2.2}$$

Where σ is applied stress, γ is the required energy to separate atomic bonds per unit surface area and create two new surfaces (J/cm^2), E is Young's modulus, α is half the crack length, and G is the strain energy release rate **(Griffith, 1920)**. However, it was not until after World War II when failures in war materiel promoted a greater interest in the effects of microcracks.

Griffith's theory showed exceptional correlation with lab data on brittle materials, but for ductile materials, the surface energy from Griffith's theory is unrealistically high due to not taking plastic deformation into consideration. George Rankine Irwin (1957) determined a line-crack is more fitting than an elliptical crack in understanding the friction within crack walls **(Anderson, 2017)**. He replaced Griffith's strain energy release rate (G) with a new term called the stress intensity factor (K_I) and replaced surface energy density with fracture toughness. His work in fracture propagation lead to the criteria for crack growth, which states that the critical work ($\mathcal{G}_c$) to create a new fracture must be less than the strain energy (G) released **(Roylance, 2001)**. In addition to fracture propagation, Irwin determined that the area of the fracture tip is entirely controlled by K_I, regardless of mode I (loading), II (sliding), or III (tearing). Equations 2.3 and 2.4 give the strain energy and stress intensity factor **(Ceriolo and Di Tommaso, 1998)**.

$$G = \frac{\sigma^2 \pi a}{E} \tag{2.3}$$

$$K_I = \sigma\sqrt{\pi a} \tag{2.4}$$

Cohesive forces in crack tip faces began to be incorporated in 1959 and 1960 by Barenblatt and Dugdale **(Ceriolo and Di Tommaso, 1998)**. Barenblatt was the first to make a cohesive crack model but failed to acknowledge the distribution of forces and assumed most cohesiveness occurred at the fracture tip (**Barenblatt, 1959)**. Dugdale added a continuous supply of closing stresses for a perfectly plastic model and thus took the Barenblatt method a step further **(Dugdale, 1960)**. Hillerborg (1976) proposed a method that introduced fracture mechanics into finite element analysis that yields results regarding crack formation, propagation, and failure with limited computer work. This method introduced energy absorption (Gc) within the energy balance system and fracture energy (GF) that represents the tensile strength and softening load **(Hillerborg et al., 1976)**. Hillerborg found two distinct zones in the fractures: a pseudo-fracture in front of the actual fracture that includes the relaxing of tension so that there are no stresses being transferred to the fracture tip, and then an extension in the process zone where stresses are being transported.

In 1963, the Paris' Law was established, which relates the stress intensity factor and fracture propagation. The relation was used to create a fatigue crack growth model that predicts the change in crack length (*da*) compared to the change in stress load (*dN*) **(Paris, 1961)**. The Paris Law can be simply written as,

$$\frac{da}{dN} = C\Delta K_I^m \tag{2.5}$$

Where da/dN is the crack extension per cycle of load, C is the material constant, K_I is the stress intensity factor for fracture opening, and m is a constant. Many derivatives have been produced from the Paris law, but the form of all crack propagation laws follow:

$$\frac{da}{dN} = f(\sigma, a, C_i) \tag{2.6}$$

where σ is the stress range **(Paris and Erdogan, 1963)**.

Micro-geometric models were developed in 1974 by Kuster and Toksoz and then 1976 by O'Connell and Budiansky, which incorporated more detail about the void space within a rock. **O'Connell and Budiansky (1976)** illustrated that the change in energy is determined by specific pore shapes and calculated crack density.

$$\emptyset_{crack} = \frac{4\pi\varepsilon}{3}\Lambda \tag{2.7}$$

$$\varepsilon = N\frac{2}{\pi}\{\frac{Area^2}{Perim}\} \tag{2.8}$$

Where $\emptyset_{crack}$ is crack porosity, ε is crack density, Λ is the aspect ratio of a two-dimensional crack or pore, and N is the number of fractures per unit volume.

Carpinteri (1980) studied concrete structure size and how it affects the brittleness behavior. This effect is called the brittle-ductile transition and determined that a small sample will fracture under ductile response while a big sample will fracture under brittle behavior **(Ceriolo and Di Tommaso, 1998)**. Quantifying this transition, Carpinteri (1981) proposed the concrete structural brittleness equation:

$$s = \frac{K_{IC}}{\sigma_0 b^{1/2}} \tag{2.9}$$

Where K_{IC} is critical fracture toughness, σ_0 is closing traction, and b is the characteristic length of the structure **(Carpinteri et al., 2009)**. The structural brittleness equation addresses the two primary problems of size effect, which are: 1) uncracked specimens show signs of brittleness when size increases, and 2) fractured specimens do not experience the effect of fractures when the structure size is small. Condition 2 is due to the decrease in stress at the fracture tip and increase in ductility **(Carpinteri, 1984)**. Carpinteri (1985) proposed the Brittleness Number, which is a foundation of fracture mechanics in brittle materials.

$$S_e = \frac{G_F}{\sigma_u h} \tag{2.10}$$

Where G_F is the amount of energy absorbed per unit crack area, σ_u is tensile stress, and h is height of sample body **(Carpinteri, 1985)**.

2.1.3 Fracture Dimensions

Solutions for 2-D fracture dimensions have been proposed by **Perkins and Kern (1961)**; they determined which operating conditions, such as injection rate and fluid viscosity, controlled the width of the crack. **Perkins and Kern (1961)** along with **Geertsma and De Klerk (1969)** developed charts and equations which permitted estimations of fracture dimensions that are used to model fracture networks. Common assumptions made in the models are that the formation is homogeneous and isotropic; that vertical pressure and fracture height are constant, and there is laminar fluid flow

(Anderson, 2017). The geometry of a simplified fracture can be explained by the two basic constant height models: PKN **(Perkins-Kern-Nordgren)** (1961) and GDK **(Geertsma-de Klerk-Khristianovic)** (1969) seen in **FIG. 4**. The early hydraulic fracture jobs were designed by using one of these two models. However, the mechanics between the two are significant **(Yew and Weng, 2014)**. For the KGD model, two more assumptions are made besides constant height: 1) Plane strain in the horizontal plane and 2) the fracture tip is cusped, which is used to remove the stress at the fracture tip. This model is typically used when fracture height is greater than fracture width. There are also two additional assumptions for the PKN model: 1) Plane strain in a vertical plane and 2) fracture toughness does not affect the fracture geometry **(Yew and Weng, 2014)**. The PKN model is typically used when fracture length is much greater than fracture height.

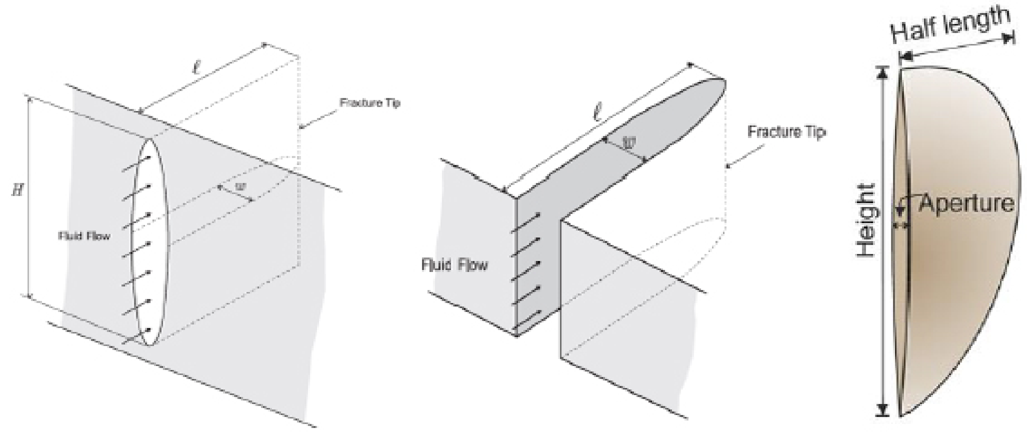

Figure 4: PKN (left), GDK (middle), and penny-shaped (right) showing the common geometries for the two models. (Adachi et al., 2007).

Although the assumptions made are unrealistic for reservoir conditions, they allow a foundation for 2-D fracture modeling. The most accurate form of modeling is 3-D, which permit fracture dimensions and orientations to fluctuate with changing scenarios. Improved modeling techniques have allowed a general overview of the fracture network caused by hydraulic fracturing, but these methods are anything but accurate or take months on super computers to model **(Rahman and Rahman, 2010)**. Natural phenomena such as pre-existing fractures, disconformities, geologic changes, and heterogeneities result in a very difficult prediction of fracture networks despite the technological advances **(Broberg, 1999)**. In addition, secondary microfractures branching off primary fractures are still not included in fracture modeling, causing inaccurate SRV predictions. The uncertainty in fracture modeling and increase in the number of fracture stimulation demand more accurate fracture analyses.

2.1.4 Fracture Orientation

Fracture orientation is typically represented as a penny-shaped structure like that of **Fig. 5 (Tran and Rahman, 2006).** The dip is the angle at which the fracture is inclined from the horizontal surface (between 0 and 90 degrees) and is typically measured perpendicular to strike. The azimuth is the direction of the fracture in the horizontal plane to the true magnetic north, which is measured clockwise (between 0 and 180 degrees). The fracture orientation is governed by the direction and magnitude of applied stresses, along with the intrinsic anisotropy and heterogeneity.

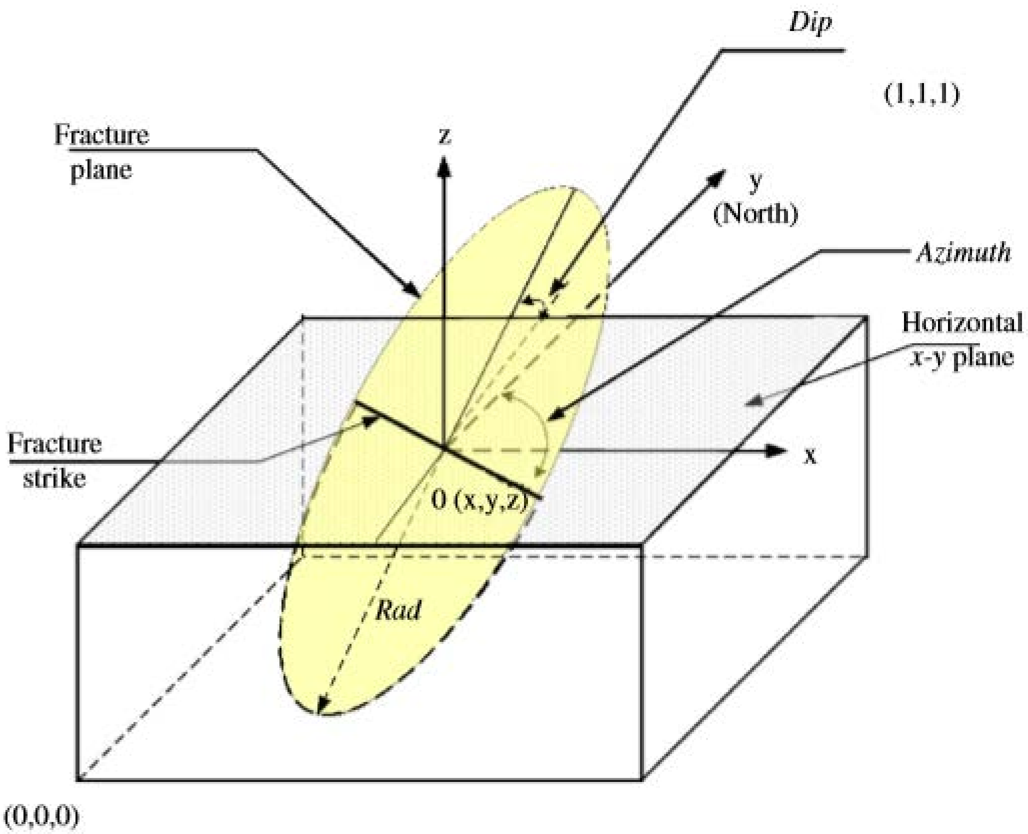

Figure 5: Penny shaped fracture model illustrating the parameters that define a 3D fracture (Tran and Rahman, 2006).

2.1.5 Fracture Termination

Fracture fatigue comes in three stages. The first stage is fracture initiation (stage I), the second stage is fracture growth (stage II) and the third is fracture propagation (stage III) **(Perez, 2004).** An important topic for stage I is the amount of elastic energy a specimen can store. Avoiding kinetics for simplification, the elastic energy can be calculated by determining the required work to cause failure.

$$W = \int_0^{\Delta l} f(x)dx = k\int_0^{\Delta l} x dx = k\frac{\Delta l^2}{2} = \frac{l_0 AE\varepsilon_f^2}{2} = \frac{VE\varepsilon_f^2}{2} = V\frac{\varepsilon_f\sigma_f}{2} = V\frac{\sigma_f^2}{2E} \qquad (2.11)$$

Where k = Hooke’s constant and is the stiffness of the body,

$$k = \frac{f}{x} = \frac{\sigma_{xx}A}{\varepsilon_{xx}l_0} = \frac{AE}{l_0} \qquad (2.12)$$

f = ma, A = area, x = elongation in the x-direction caused by stress acting in the x-direction, σ_{xx}= f/A and is the stress operating in the x-direction, $\varepsilon_{xx} = \frac{x}{l_0} = \frac{\sigma_{xx}}{E}$ and is a non-dimensional variable, l_0= initial length, Δl = the final elongation caused by stress, $\varepsilon_f = \Delta l / l_0$ (final strain), $\sigma_f = E\varepsilon_f$ = final stress, $\frac{1}{\varepsilon} = \frac{E}{\sigma}$, E = Young's modulus, and V = the initial volume **(Bahat et al., 2009)**. By dividing W by V in equation 2.11, the energy per unit volume is

$$\frac{W}{V} = \frac{1}{2}\sigma\varepsilon = \frac{1}{2}E\varepsilon^2 = \frac{1}{2}\frac{\sigma^2}{E} \tag{2.13}$$

The final equation is divided by two to represent the amount of energy stored in 1 end of a bar acted upon by uniaxial force.

Elasticity is built on a model in static equilibrium (**Fig. 6**). These stresses are elements of the stress tensor σ_{ij}, where i is the direction normal to the surface upon which it is acting, and j is the direction of acting stress, j = 1, 2, 3 = x, y, z.

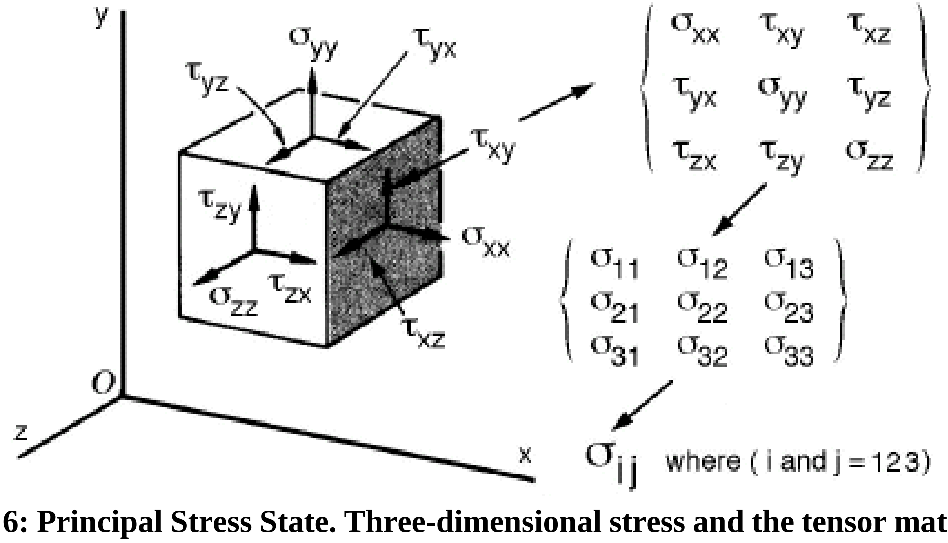

Figure 6: Principal Stress State. Three-dimensional stress and the tensor matrix are shown for different elements (Perez, 2004).

The discovery of natural fractures, or "flaws", within the system permits a basis of energy reduction around the fracture due to the stress concentrating at the fracture tip

(Broberg, 1999). The total energy reduction around the fracture is dictated by the volume of the fracture and thus the length c and thickness b. For simplification, equation 2.14 is the volume for a 2D eclipse.

$$V \sim \frac{1}{2}\pi c^2 b \tag{2.14}$$

By knowing the average length of the internal flaws, the total energy relieved can be calculated by multiplying the last equation in 2.13 by V to get 2.15 **(Bahat et al., 2009)**.

$$W_E \sim V\frac{\sigma^2}{2E} = \frac{\pi\sigma_0^2}{4E}c^2 b \tag{2.15}$$

Griffith stated that all energy acting on the sample will be distributed to the newly formed fracture surface. This being true, we can calculate the energy required to create a new fracture surface if we assume the surface energy needed (γ) is constant.

$$\Delta W_s = 2\gamma b\Delta c \tag{2.16}$$

Equation 2.16 is the work required to initiate two new surfaces (1 fracture) based on the flaw’s dimensions. This equation holds true for the energy balance equation which requires that the release of energy must be equal to the newly created surface energy **(Bahat et al., 2009)**.

For brittle material, there are two primary methods for forecasting fractures in a specimen. The first follows the conservation of energy. The second pertains to the amplitude of stress at the tip of a flaw and if that stress reaches the critical value to separate atoms. This value is the stress intensity factor K and is calculated from the crack size, shape, geometry, load level, and loading configuration **(Saxena, 1998).** The value of K depends on the geometries of the specimen. For hydraulic fractures, the number of cycles being pulsated into the formation or the “number of fatigue cycles” N over a period will determine the cumulative formation damage. These fatigue cycles are correlated with the fracture growth per cycle and is labeled $\frac{da}{dN}$ and relies on the stress intensity factor range ΔK and the number of fatigue cycles N **(Perez, 2004)**. A simplified version of ΔK is given by:

$$\Delta K_{th} = \psi \Delta \sigma_{th} \sqrt{\pi \alpha} \tag{2.17}$$

Where ψ is a function of fracture length over width, $f\left(\frac{a}{w}\right)$, and is known as the geometric correction value, α = fracture length, w = fracture width, and σ_{th} = fatigue limit. If $\Delta\sigma < \Delta\sigma_{th}$ then the fracture will not propagate. Equation 2.18 shows how the fracture growth per cycle relates to the stress intensity factor, which was given in the Paris laws for fatigue crack growth in stage II.

$$\frac{da}{dN} = A(\Delta K_{th})^n \tag{2.18}$$

Where A is a constant $\left(\frac{MPa^{-n} * m^{1-n/2}}{cycles}\right)$ and n is an exponent **(Perez, 2004).**

2.1.6 Fracture Tip

The normalized shapes of the von Mises and Tresca diagrams at a crack tip are shown in **Fig. 7**. It is apparent that the von Mises and Tresca diagrams are very different, however, the plane strain condition always produces a smaller plastic zone than the plane stress condition, illustrating smaller plastic zones for maximum constraint on thick bodies. The plastic zone analyzed in this paper is best represented by the Tresca yielding criterion for plane stress. However, it is seen that the plastic zone starts much further behind the fracture tip, then what is shown in **Fig. 7**.

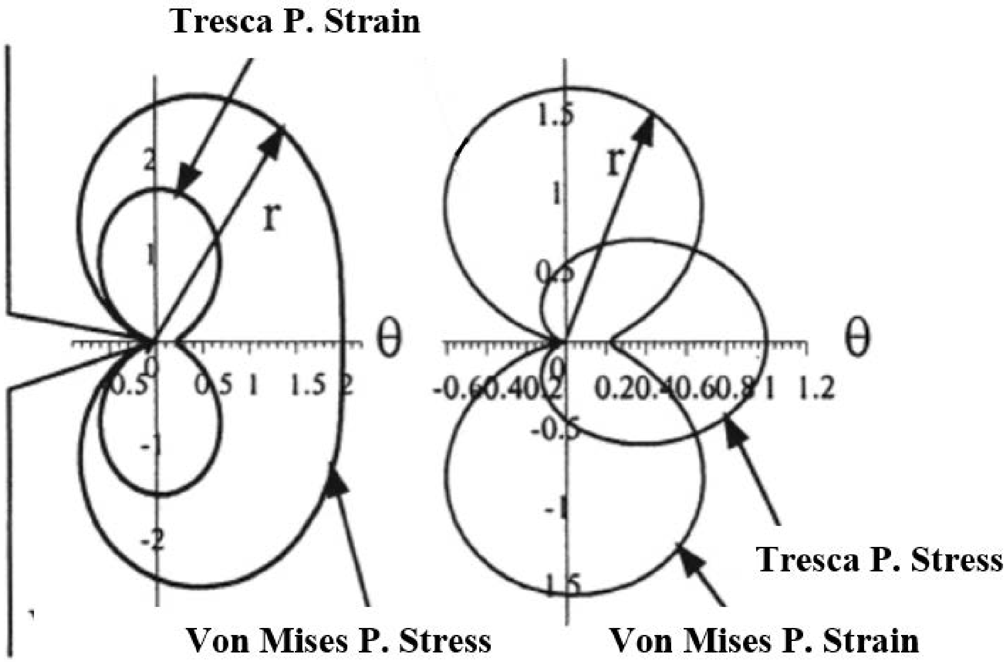

Figure 7: Von Mises and Tresca plastic zone shapes. The Tresca and Von Mises are very different, but the plane strain is always smaller than the plane stress (Modified from Perez, 2004).

When fracture tip pressure becomes greater than pore pressure, a pressure wave emanates in front of the tip and causes alterations to the fracture propagation pattern. This pressure wave travels normal to the fracture and along the fracture growth direction **(Entov et al., 2007)**. The pressure wave can alter leak-off rates as well as create microcracks ahead of the primary fracture. The result is potentially new fracture propagation paths and needs to be taken into consideration when modeling fracture propagation. To determine fracture direction, parameters such as aperture, stored energy, notch tip, pressure distribution, roughness, rate of leak-off, formation pressure, and cross flow rates need to be determined **(Dong and de Pater, 2008)**. In negligible leak-off, an increase in viscosity imposes a stronger pressure wave that causes a greater amount of alterations; fluid viscosity effects energy consumption, and thus net pressure calculations.

Permeability plays an important role in pressure alterations near the fracture tip. If permeability is high, fluid will enter the fracture when hydraulic pressure is below formation pressure. This influx of fluid may drastically change the pressure distribution and strain intensity factor near the fracture tip **(Mikhailov et al., 2011)**.

2.2 Microfracture Statistics

2.2.1 Historical Development

Wawersik and Brace (1971) conducted research on thin sections of fractured granite rocks. Their research focused on the characterization of microfractures with respect to confining pressure and found that an increase in confining pressure decreased intergranular fractures.

Peng and Johnson (1972) developed fracture density maps for thin sections of stressed rocks that included length and orientation with respect to applied stress. Their work in granite showed that microfractures are initially random but become more oriented and dense as failure is approached.

Hallbauer (1973) performed a series of triaxial compression tests to document macroscopic and microscopic images for fracture density maps in deformed sandstone thin sections. He determined that high fracture density zones coalesced into one macroscopic fracture and grain on grain contact under stress is a common point for fracture initiation.

Sprunt and Brace (1974) began analyzing microfractures using an SEM. They developed the current standard for cutting, grinding, polishing, ion-milling, and sputter coating the sample prior to SEM investigation. The use of the SEM instrument began a more detailed account for fracture statistics. **Sprunt and Brace (1974)** used the SEM in their evaluation of intergranular fractures and found fracture-free boundaries in gabbro but varied fracture quantities in granites. They determined that the mineralogy of the sample had a factor in fracture initiation.

Simmons and Richter (1976) suggested that microfracture characteristics (such as length, width, and quantity) vary significantly and the variation is largely due to the pressure and temperature which they were formed. Primarily based in igneous rocks, **Simmons and Richter (1976)** produced photomicrographs from thin section and SEM images to classify fracture types. They also determined that discriminating between grain boundaries and microfractures is difficult and a dye should be implemented to distinguish the two.

Tapponnier and Brace (1976) illustrated that the magnification needed for proper microfracture analysis in compression tests was on a micron scale. The increased magnification reduced the surface area being analyzed, which lowered the amount of data being collected. To increase surface area, they manually stitched SEM images together to analyze fracture densities with applied stress. Their results showed fracture density doubled at peak stress.

Hadley (1976) and Brace (1977) focused their attention on fracture length, width, aspect ratio, and orientations for stressed and unstressed granites. Using photomicrographs, they established fracture parameters based on changes of stress and mineralogy.

Kranz (1979) used the SEM to study the effects of crack growth development during creep. This study showed the effects of fracture velocity on the microfracture network. He compared the difference between fracture growth as a function of time with a constant stress, to fracture growth as a function of stress with a constant strain rate. **Kranz (1979)** determined that with a constant load, fractures continue to extend with time, while new cracks are generated.

Swanson and Spetzler (1979) determined that a larger quantity of intergranular fractures were created in rocks that were loaded at slow stress rates as opposed to shock loading, which created more intragranular fractures.

Atkinson (1979a) determined intergranular and intragranular fractures were strongly controlled with calcite cleavage planes. **Atkinson (1979b)** documented fracture toughness and strain energy release rates that are used to measure the amount of resistance to fracture propagation. In addition, he studied the effects of water on propagation rates within quartz and found that subcritical crack growth could be caused by chemical reactions between the siloxane quartz bonds and water.

Friedman and Johnson (1978) and **Friedman et al. (1982)** studied the effects of rock strength and fractures as a function of temperature in granodiorite. They determined that microcracking starts at a temperature (200˚C for sandstone) but varies depending on the thermal development of the rock. Once the rock rises above the previous greatest temperature, grain boundaries start to separate and intergranular fractures appear, as monitored by acoustic emissions. It was found that intragranular fractures were typically perpendicular to grain boundaries and fractures were prone to following cleavage planes in minerals. Furthermore, the addition of water during fracture propagation did not increase the amount of microfractures but reduced the amount of stress needed for fracture initiation.

The use of acoustic emissions (AE) began in the early 1960s by **Mogi (1962, 1963)** who determined there was a strong correlation between the microfractures produced by earthquakes and those produced within the lab. **Scholz (1968a)** described the physical basis for microfracture and seismicity, which displays differences between the mechanisms of fracture processes but greater similarities between the properties of rocks in the laboratory and Earth's crust. AE can detect thousands of emissions over the course of fracture initiation, propagation, and termination, which conveys a new approach to fracture analysis. Using this technique, one can investigate how the fracture reacts to its surroundings in real time. The downside to AE is that the location accuracy is near 1 millimeter, making detailed microfracture analysis difficult (**Sondergeld and Etsy, 1981**).

Nemati (1997) hydraulically fractured a concrete sample under a uniaxial load with lateral confinement using Wood's metal to illuminate the fracture patterns in SEM and CT analysis. The Wood's metal provides a high-density contrast leading to more accurate fracture analysis.

Grain orientation studies became increasingly popular in the 1940s-1950s when importance in sediment transport and depositions of environment was discovered **(Dapples and Rominger, 1945; Griffiths, 1950; Schwarzacher, 1951)**. This procedure was first conducted on microscopes but proved uneconomical due to the small sample area or the length of acquisition time needed for sufficient data. **Zimmerle and Bonham (1962)** advanced grain orientation analysis by developing an electronic spot scanner that accurately determined grain orientation in sandstone within minutes. Today, grain orientation can be readily determined by using automated software on optical, spectroscopy, transverse shear microscopy (TSM), transition electron microscopy (TEM), and SEM instruments **(Kalihari et al., 2008)**.

Nohava (2003) used an EBSD detector to analyze cleavage cracks in steel. His work determined that secondary fracture propagation is primarily controlled by the angle of orientation between grains. The secondary fractures were more likely to terminate if the grain orientation was greater than 55° to the direction of propagating fracture and were most likely to propagate if the grain orientation was less than 10° of the direction of propagating fracture.

Nasseri (2006) used AE to monitor fracture toughness in static loading conditions in brittle rocks. Results illustrated that the fracture mechanism prior to failure was tensile, but post-failure was tensile and shear. He also noticed a rapid increase in AE at the fracture termination point, suggesting a change in physics in the fracture tip. **Nasseri (2006)** stated that the formation of the fracture process zone could be accurately tracked by AE.

Padin et al. (2014), studied microfracture propagation in kerogen rich shales through field observations of exploratory wells in the Vaca Muerta and Eagle Ford. They determined the most significant factors that control fracture propagation are the mineralogy, TOC content, anisotropy of fabric between clay and non-clay minerals, anisotropy of stresses, orientation of pre-existing fractures, elastic moduli, and over pressure conditions.

Rho et al. (2017) used finite element simulations to model fracture propagation in layered mudstones with weak interfaces. This research shows that layer boundaries with high permeability will shorten the length of the propagating fracture due to the fracture's desire to follow the path of minimum energy. They observed that the higher the pore connectivity between mud layers, the shorter the fracture. Furthermore, fracture dimensions were also affected by Young's modulus, suggesting a low Young's modulus created a short and wide fracture while a high Young's modulus created a long and thin fracture.

2.2.2 Fracture Statistic Techniques

Counting fractures is a tedious task that requires acute attention to detail and knowledge within the fields of geology and fracture mechanics. The techniques used today follow the same methods that have been used for the past 100 years with an addition of new technology. These techniques are observational, recording characteristics such as length, width, orientation, quantity, azimuth, and process zone. Today, much of fracture counting has become automated with new software. However, the accuracy for automated micro and nano statistics remain low.

The first techniques developed used the naked eye. This method is good for large scale fractures such as faults that have propagated to the Earth's surface. Data was collected by simply observing the fracture network and documenting statistics. Later this method was accompanied by aerial and satellite imagery.

With Griffith's (1920) discovery of microfractures and their effect on structural integrity, statistical techniques were altered to take small fractures into consideration. Thin sections with optical observations at high magnification were the most common technique in the early stages of microfracture investigation. This procedure allowed a quantification of microfracture statistics.

Technological advancements and the interest in microfractures lead to analysis using scanning electron microscopes, which permit a nano-scale imaging, and for the first time, allowed the observation of secondary microfractures and nano-pores in very fine-grained samples. With this instrument, high resolution images are captured and stitched together to form large scale, high resolution mosaic images. The development of automatic imaging and stitching software has greatly reduced the data acquisition and processing time.

Alternate techniques such as AE, can be used to monitor the fracturing process. This is beneficial due to its ability to track the fracture as it matures through initiation, propagation and termination. However, the spatial accuracy of AE locations and time resolution prohibit the registration of AE and SEM observation.

2.2.3 Fracture Analysis Using SEM

SEM has allowed additional contribution to fracture analysis by providing information on subjects such as, crystal orientation, porosity, permeability, roughness, and microstructural heterogeneity, which play important roles in fracture initiation and propagation **(Chesnutt and Spurling 1977; Nohava et al., 2002; Sondergeld et al., 2010; Lemmens et al., 2011; Suri 2011; Damani et al., 2012; Curtis et al., 2013a and 2013b)**.

Two types of fractures arise during propagation: 1) intergranular, which suggest that the fracture follows along the outside of the grain boundary, and 2) intragranular, fractures that propagate through the grain. This modality is strongly controlled by the stress that is imposed onto the sample, grain orientation, and sample ductility. **Nohava (2002)** used SEM imaging to illustrate that secondary fractures propagate homogeneously despite the crystallographic planes that are being traversed ({100}, {110}, {112}, and {123}). The higher ductile zones, however, reduced the energy in the fracture and promote more intergranular fractures, while brittle zones showed signs of more intragranular fractures **(Nohava et al., 2002)**.

SEM imaging has allowed a simultaneous examination of fracture networks and microstructure. Surface aspects such as fracture roughness and topography were examined by **Chesnutt and Spurling (1977)** and **Bahat (1999)**, who developed correlations between fractures and surface heterogeneities.

Recent SEM analysis on the secondary fracture network have been conducted (**Ortega et al., 2006; Bhagat 2012; El-Monier 2016)** but have not been accurately documented due to sample preparation artifacts. By hydraulically fracturing the samples with an epoxy or liquid metal, the fractures can be uniquely distinguished, providing more accurate statistics.

2.3 Stress Induced twinning

Mechanical twinning is the occurrence of two separate crystals sharing the same crystal lattice. This is usually induced by pressure at low temperatures and high rates of loading (shock loading). For quartz, twinning occurs at stresses around 72,000 psi **(Bertagnolli et al., 1979)** and is pervasive at 145,000 psi at ambient temperatures **(Tullis and Tullis, 1972)**. At elevated temperatures and pressures, twinning is already initiated at stresses between 7,000 and 29,000 psi **(Wenk et al., 2006, 2007)**. The constant Critical Resolved Shear Stress (CRSS) for twinning in calcite is 1,450 psi **(Lacombe, 2001)** and findings in impact craters show an abundance of calcite twinning at 14,500 psi **(Lindgren et al., 2012)**. We investigate the possibility that hydraulic fracturing can produce twins in nearby grains; this could alter fracture plane orientation and promote further slippage. The twin boundary that is formed between the crystals results in a plane of weakness, which could alter the fracture’s path and cause it to deviate from its original course. The determination of induced crystallographic effects can aid in fracture propagation models and stimulation patterns that result in energy loss.

Mechanical twinning was first documented by **Schubnikov and Zinserling (1932)**; they determined that twins can be produced under pressure. **Tullis (1970)** found that Dauphiné twins were most prevalent in quartz and were unique in comparison to Japan and Brazilian twinning. The oddity of the Dauphiné twin is that the host-twin relationship possesses a 180-degree rotation about the c-axis of trigonal quartz, thus producing no contrast in a petrographic microscope and therefore cannot be seen optically **(Wenk et al., 2011)**. This aspect not only eliminates the use of petrographic microscopes but most SEM detectors as well. The best method to study the effect of Dauphiné twins is to use an electron backscatter diffraction (EBSD) detector within an SEM microscope **(Heidelbach et al., 1999)**.

In the 1700s Leonhard Euler developed a set of parameters, known as the Euler angles, to describe the orientation of a specimen with respect to a fixed point. These angles are heavily used in aerospace engineering, astronomy, and geology. The Euler angles, known as ϕ, ϕ_1 and ϕ_2, are the rotation(s) needed to bring the sample reference angles into correlation with the crystal reference frame. **Fig. 8** shows an example using an airplane. The most common explanation for Euler angles is the Yaw, Pitch, and Roll method, where yaw, ϕ, represents the rotation around the Z axis, Pitch, ϕ_1, is the rotation around the Y axis, and Roll, ϕ_2, is the rotation around the X axis. With these three angles, the orientation of a crystal can be determined.

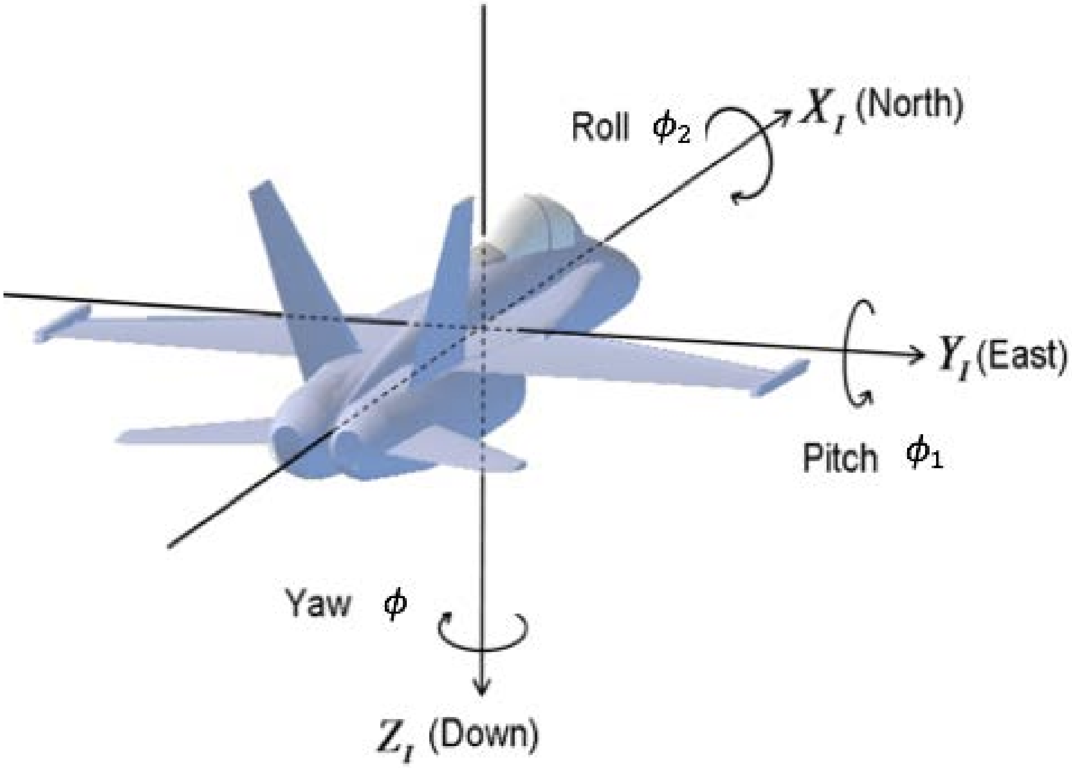

Figure 8: Yaw (ϕ), Pitch (ϕ_1), and Roll (ϕ_2). Showing how Euler angles are used to classify the orientation of a sample (Modified from Mechscience, 2017).

On a microscopic scale, Dauphiné twins do not change the alignment of the axes but reverse the positive and negative rhombs, {1011} and {0111}. This holds great significance because the direction along the negative rhomb is twice as stiff (elastically) as the direction normal to the positive rhomb, allowing twins to develop normal to the negative rhombs and giving new orientations parallel to the direction of compression **(Wenk et al., 2011)**. To identify twin boundaries, the identification of the inverse patterns of positive and negative rhombs is essential (**Tullis, 1970). Fig. 9** illustrates the effects of twinning along the c-axis.

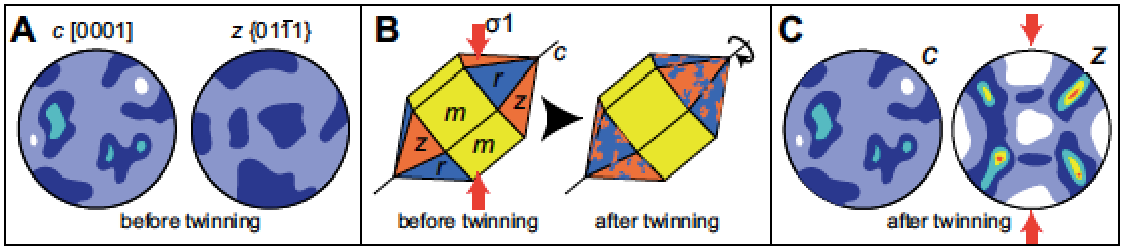

Figure 9: Cartoon of crystallographic quartz showing pole figures. A) shows a uniform c-axis and negative rhombs. B) 3D quartz structure displaying the prism (m), positive rhomb (r), and negative rhomb (z). The red arrows show the greatest principal stress where Dauphiné twinning will occur. C) Post-mechanical twinning illustrating crystallographic direction (normal to the negative rhomb) (Rahl et al., 2018).

Chapter 3: Experimental Methodology

Chapter 3 describes the equipment and methodologies used for the fracture and SEM experiments. A Tennessee sandstone sample was fractured using a triaxial loading system by **Damani (2013)**; his methods and materials will be discussed. The shale and pyrophyllite samples were fractured using a uniaxial loading system and were fractured by the author.

3.1 Equipment and Materials

3.1.1 Triaxial Loading System

The hydraulic fracture triaxial loading system used for this experiment was designed and built by New England Research Inc. (**Fig. 10** and **Fig. 11**). This system applies three independent stresses on a cylindrical sample. The vertical stress is activated using a piston, the confining stress is applied by the injection of hydraulic oil, and the transverse stress is attained using a pair of flat jacks with a conformal radius to the sample that is hydraulically activated. The injection pressure was monitored using an in-house monitoring software and continuous acoustic events are recorded with WaveExplorer™.

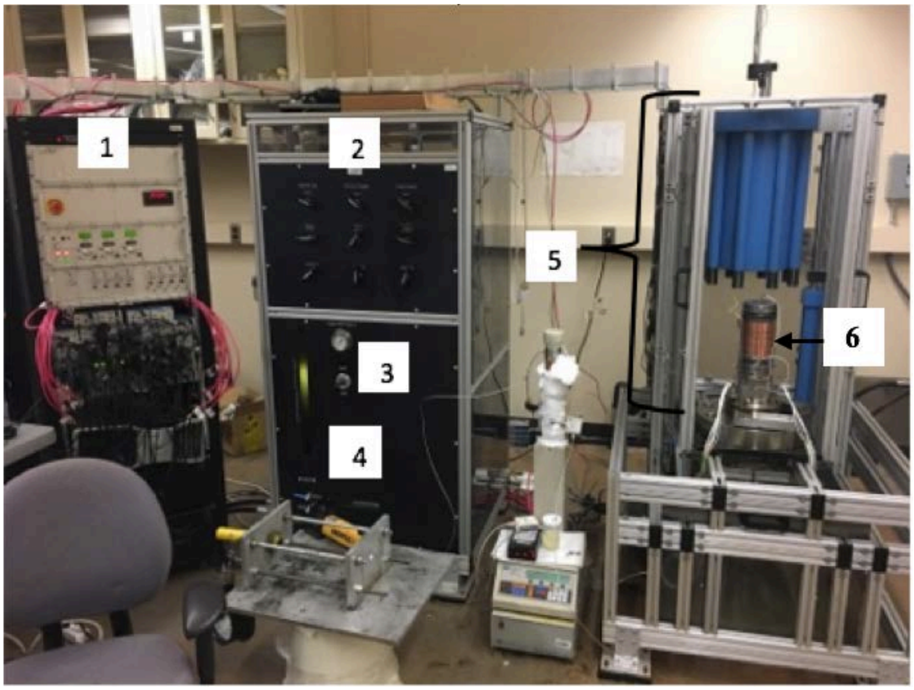

Figure 10: Triaxial fracture apparatus; 1) computer control station; 2) fluid valve locks; 3) confining fluid valve; 4) confining fluid storage; 5) triaxial loading compartment; 6) sample.

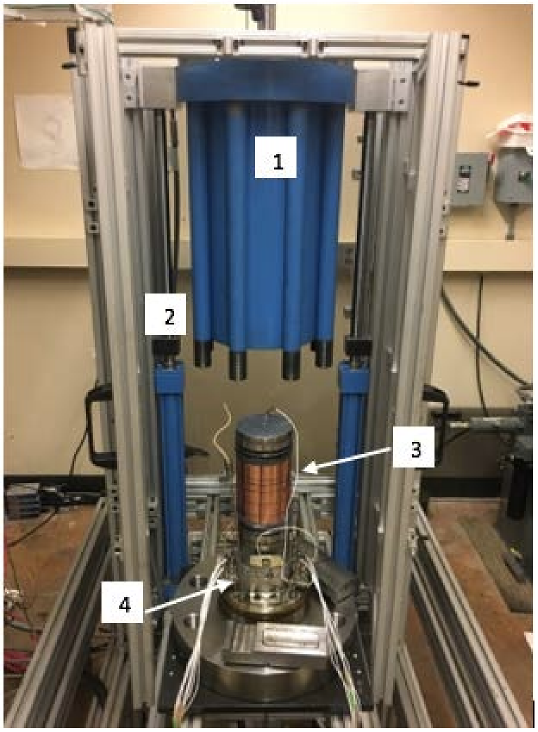

Figure 11: Close-up on the triaxial fracturing compartment; 1) loading piston, located on the inside of the confining vessel; 2) confining vessel; 3) copper jacket around sample; 4) acoustic transducers (not connected).

3.1.2 Uniaxial Loading System

The uniaxial loading system was designed in-lab and is comprised of a steel frame with a single hydraulic piston (see **Fig. 12)**. This apparatus applies a uniaxial load. The surface area in contact with the sample will govern the magnitude of applied stress. Injection pressure was measured with a transducer connected to the injection pipe and monitored continuously using software.

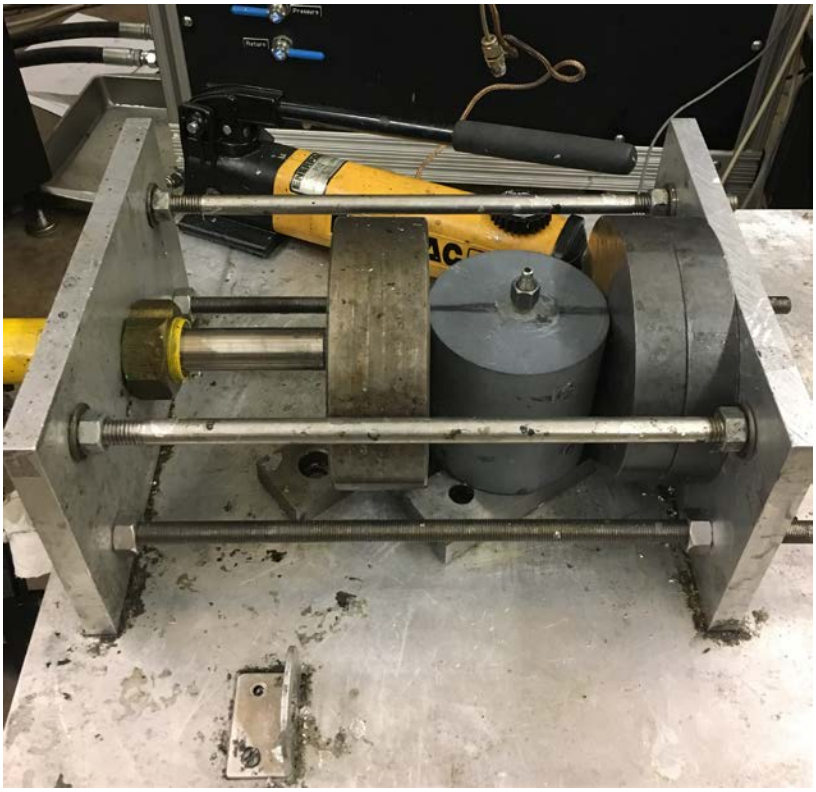

Figure 12: Uniaxial fracture test apparatus illustrating a single piston loading system on a cylindrical sample.

3.1.3 Pumping Unit

Two Teledyne Isco 100DX pumps were used to inject fracture fluid into the sandstone sample and a single Teledyne pump was used to inject fluid into the shale and pyrophyllite samples. This pump can generate 10,000 psi with flow rates up to 50 ml/minute and quick reloading capabilities. The cylinder is corrosion resistant and holds 102.93 ml with a temperature control jacket and displacement resolution of 9.65 nanoliters.

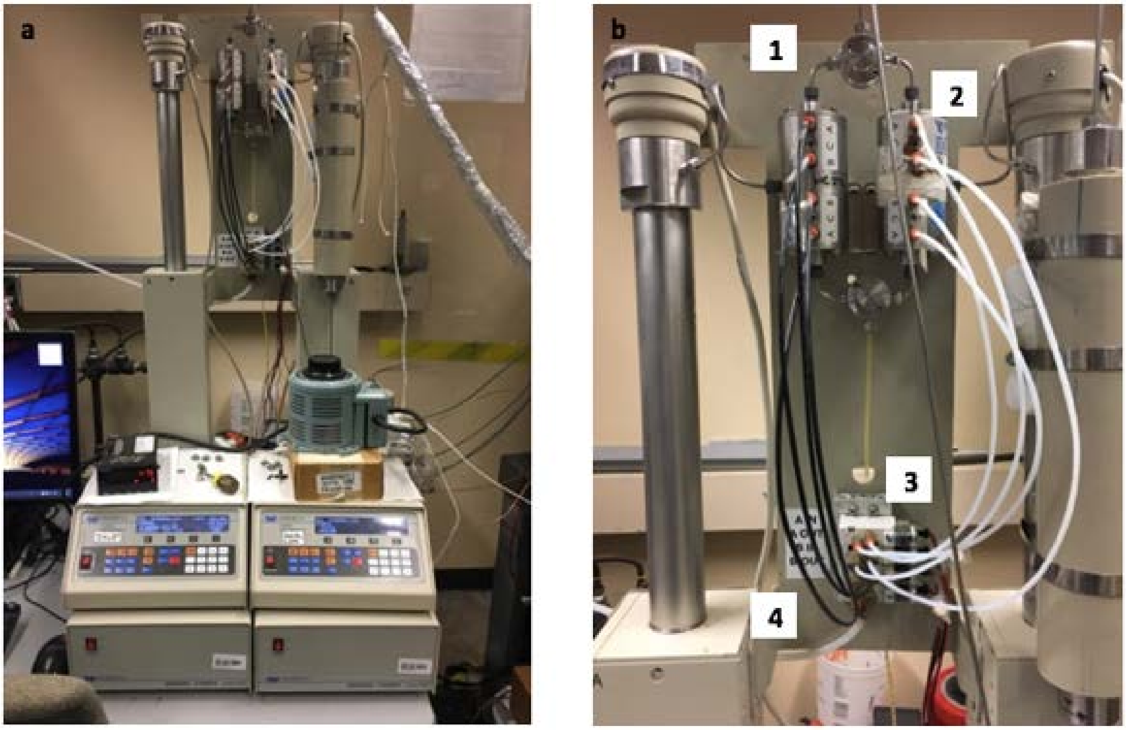

Figure 13: (a) Dual Teledyne Isco™ hydraulic pumps; (1) fluid outlet; (2) air-controlled valves; (3) fluid inlet; (4) solenoid regulators.

3.1.4 Fluid System

Two fracturing fluids are used in these experiments; a low viscosity epoxy (μ = 65 cP) created by Embed-It and is modified from the Spurr's formulation **(Spurr, 1969)** and Field's metal. The epoxy is used to capture the fracture network as close to native state as possible and to highlight the network for SEM analysis. Field's metal **(Fig. 14)**, melts at 70˚C and has a viscosity similar to mercury (μ = 1.6 cP). This metal was used to fracture two samples with the potential to infiltrate and delineate the fracture network for SEM and CT analysis.

Figure 14: Liquid Field's metal at a temperature greater than 70˚C. Field's metal is 32.5% Bismuth, 16.5% Tin, and 51% Indium (READE, 2018).

3.1.5 Coring and Cutting Systems

We cored 1" plugs from the 6" tall by 4" in diameter hydraulically fractured samples. The locations of the horizontal and vertical plugs with respect to the primary fracture are important and were documented. The 1" plugs were then cut into discs (1-2 centimeters thick) using a precision saw. The samples were cut using a diamond wafering blade. Samples were cut in vertical and horizontal slices. 6 plugs were drilled out of the Tennessee sandstone while 1 plug was drilled out of the shale and pyrophyllite samples. Each plug was then cut into several discs for SEM analysis, totaling 25 SEM samples.

3.1.6 Polishing Systems

The sandstone, shale, and pyrophyllite samples were polished sequentially to 800 and 1200 grit sandpaper to obtain a smooth, scratch free surface. Once no scratches could be seen on the surface, a Model 1060 Fischione™ ion mill was used to produce an ultra-smooth finish (**Fig. 16b).**

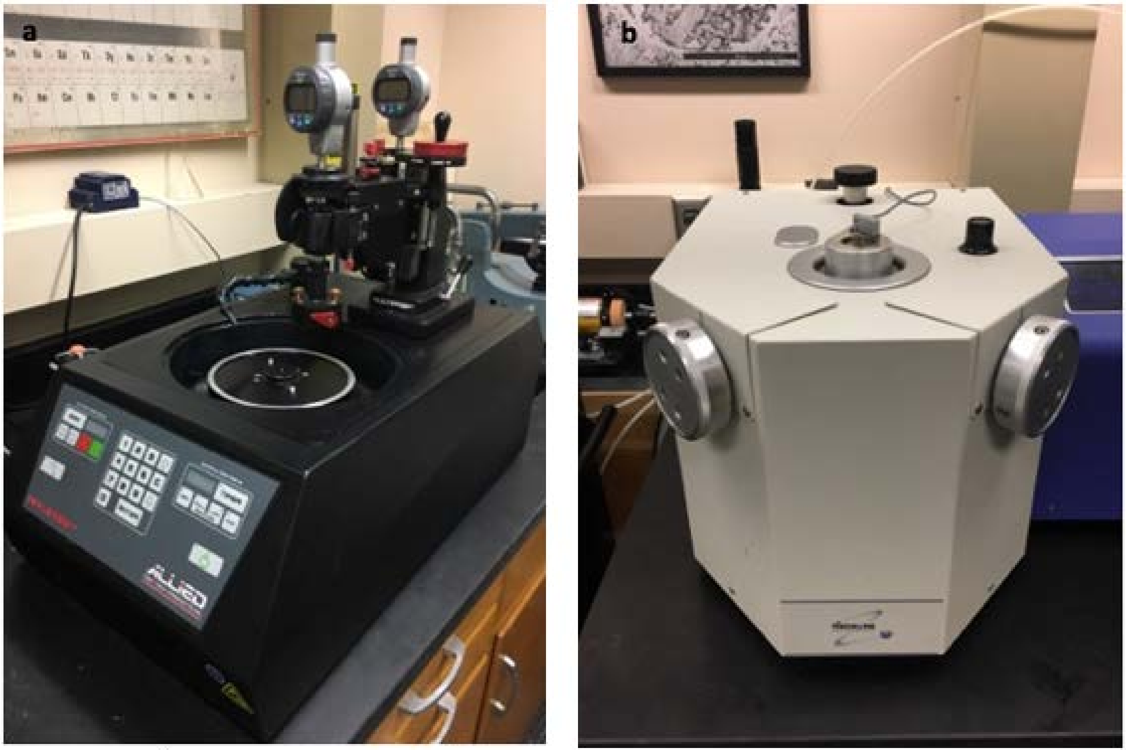

Figure 15: (a) Allied automatic polisher; (b) Model 1060™ Fischione ion mill. Allows molecular polishing on a 1-inch plug surface for superior SEM observation.

3.1.7 SEM

A FEI Helios Nanolab 650 DuelBeam FIB/SEM machine (**Fig. 17**) was used for fracture analysis. FEI "MAPS" software was used to acquire and stitch images into a large area mosaic. A Zeiss NEON FEG dual beam high resolution was used for the Oxford electron backscattered diffraction (EBSD) study.

Figure 16: FEI HELIOS NANOLAB 650™ Scanning Electron Microscope with multicomputer software and analysis. (1) pressurized vacuum chamber; (2) electron column used to focus and illuminate the specimen; (3) electron gun produces the electron beam; (4) control panel.

3.2 Sample Characterization

The petrophysical measurements presented here were conducted on Tennessee sandstone, Marcellus shale, and pyrophyllite. The measurements include helium porosity, acoustic velocity, total organic carbon (TOC), Fourier transform infrared spectroscopy (FTIR) mineralogy, nuclear magnetic resonance (NMR), mercury injection capillary pressure (MICP), nanoindentation, source rock analysis (SRA), and Brunauer-Emmett-Teller (BET) surface area analyzer.

3.2.1 Petrophysical Summary

A summary of the petrophysics is presented in **Tables 1, 2,** and **3**. The black bars illustrate data that was not collected.

Table 1: Petrophysical properties for Tennessee sandstone, Marcellus shale, and pyrophyllite. Thomsen's parameter ε, is a change in the P-wave velocity and γ, is a change in the S-wave velocity. The low changes suggest the sample is homogenous.

	LPP	**MICP**		**TOC**	**Velocity**		
	Total Porosity, %	Effective Porosity, %	Average Pore Throat Radius, µm	TOC (wt%)	Thomsen's Parameter Dry (γ)	Thomsen's Parameter Dry (ε)	Poisson's Ratio Dry
Sandstone	10	5.7	133	0.1	.025	.06	.12
Shale	9.1	6.5	3.4	9.8			.275
Pyrophyllite	5.27	3.25	7.3	0.97			.17

Table 2: Nanoindentation for Tennessee sandstone, Marcellus shale, and pyrophyllite, and SRA data for Marcellus shale.

	Nanoindentation		**SRA**					**BET**
	Young's Modulus, GPa	Hardness GPa	S1	S1/TOC	S2	S3	Max Temp, C$^\circ$	Surface Area, m^2/g
Sandstone	59							
Shale	24	.4 ± 5	.66	.17	12.14	1.39	418.9	10
Pyrophyllite	25							

Table 3: FTIR mineralogy of Tennessee sandstone, Marcellus shale, and pyrophyllite rounded to the nearest percentage.

Mineral	**FTIR Mineralogy (wgt. %)**		
	Sandstone	**Shale**	**Pyrophyllite**
Quartz	85	13	0
Calcite	0	0	2
Dolomite	1	0	3
Illite	0	26	0
Smectite	1	0	16
Kaolinite	3	0	0
Chlorite	0	0	2
Pyrite	1	0	0
Orthoclase Feldspar	1	2	0
Oglioclase Feldspar	0	0	1
Mixed Clay	6	37	61
Albite	3	13	4
Anhydrite	1	0	2
Siderite	1	6	5
Apatite	1	0	2
Aragonite	0	3	2

SRA data suggests that the Marcellus shale is immature with type III kerogen. Furthermore, the S2 peak illustrates a good source potential with sufficient TOC.

3.3 Experimental Procedure

3.3.1 Triaxial Fracture Procedure

The ends of a cylindrical core, 6” long by 4” in diameter, were polished to a maximum deviation of ± 0.01”. A borehole, 0.25” in diameter and 4” deep, was drilled in the center of the core. Because the wellbore is the same size as the borehole, a second borehole is drilled slightly off-center to the first to widen the hole and allow the wellbore to be inserted easily with a small amount of room for epoxy. The wellbore is made from a steel pipe with dimensions 0.25” OD and 0.187” ID (See **Table 4** for a summary on sample and completion dimensions). Injection ports in the pipe are made by cutting two holes into the pipe using a metal saw. In addition, the saw was used to abrade the outside walls of the pipe to create more surface area and allow the epoxy to adhere more effectively. The sides and bottom of the pipe were covered with epoxy and inserted into the borehole, making sure epoxy did not clog the ports. The core was set aside for 24 hours to allow epoxy solidification. An illustration of the prepared core sample can be seen in **Fig. 18**.

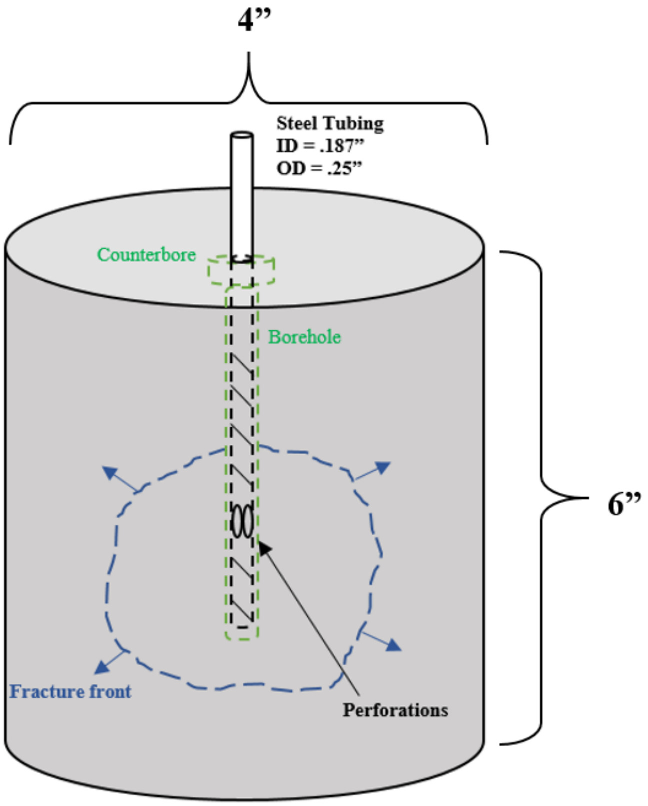

Figure 17: Schematic representing the hydraulic fracture sample. Steel, 1/4” tubing is placed in the middle of the sample and sealed with epoxy. Ports are drilled into the pipe to allow fluid injection.

A copper jacket is placed around the core and inserted into the triaxial test frame, where metal end caps are placed above and below the sample. Elastomeric (R47) tubes are placed around the sample and end caps and sealed with Viton tubing seal. The sample is inserted into the pressure vessel and confining pressure is set to 3000 psi. This procedure seals the copper jacket to the core.

When the sample is ready to undergo the fracture procedure, elastomeric tubes are inserted on the top and bottom of the sample, overlying the core and the metal spacers. To prevent confining oil penetration, stainless steel wire is wrapped around the tubes and tightened around the metal spacers. A Scotch-Weld™ epoxy was used as a seal between the Viton and copper jacket and allowed to set for 24 hours. Strain gauges and acoustic transducers were mounted to the rock sample to measure strain and acoustic emissions.

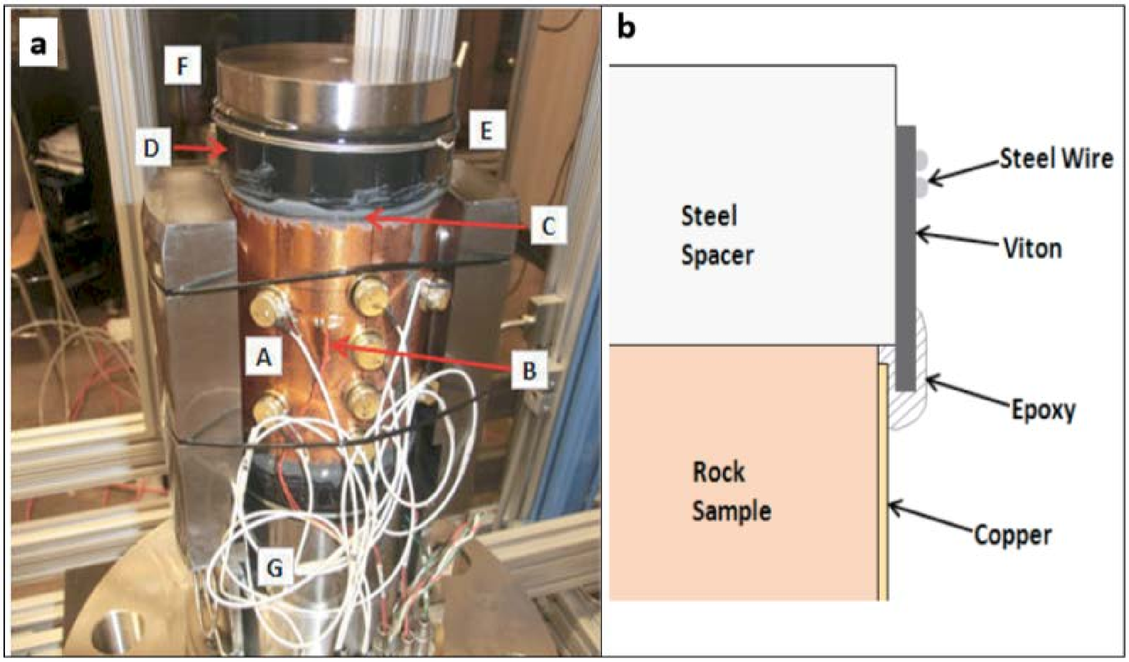

Figure 18: a) Rock sample with copper jacket A) transducers B) strain gauge C) epoxy seal D) Viton tube E) steel wire seal F) top spacer; b) schematic of top seal (Damani, 2013)

A low viscosity epoxy was used as the injection fluid. There are two primary reasons to fracture a sample using epoxy; one, the epoxy helps preserve the fracture network. This is important because SEM sample preparation produces vibrations from drilling, cutting, and polishing, thus creating new fractures, widening old fracture, and extending the length of pre-existing fractures. With the use of epoxy, these problems can be reduced for more accurate analysis. The second reason to use epoxy is to dye or mark the produced fractures. In sandstone, grain boundaries and secondary fractures can look very similar. By impregnating the rock with epoxy, we can determine where the hydraulic stimulation ends based on where the epoxy ends. For this experiment, any fracture that contained epoxy was considered produced by the fracture experiment, and any fracture that did not contain epoxy was considered to be produced by artificial means and was disregarded.

The triaxial stresses used in the Tennessee sandstone experiment were 3000 psi axial stress (σ_v), 2000 psi transverse stress (σ_H), 500 psi confining stress (σ_h), and 1500 psi horizontal differential stress. The injection rate was a constant 5 ml/min until fracture occurred.

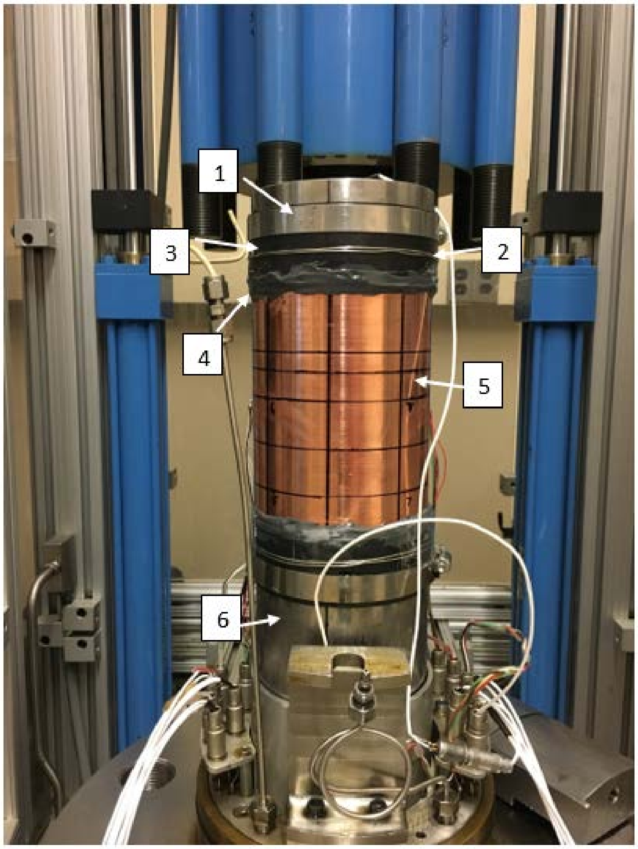

Figure 19: Core sample prepped for hydraulic fracture; (1) top metal spacer; (2) steel wire; (3) elastomeric tube; (4) epoxy between the rock sample, copper jacket, and elastomeric tube; (5) copper jacket; (6) bottom metal spacer.

3.3.2 Uniaxial Fracture Procedure

Two cylindrical cores, one shale and one pyrophyllite, were prepared for uniaxial fracture experiments the same way the sandstone was prepared for triaxial experiments. The differences are that no jacketing was performed, and the size of shale sample differed (See **Table 4**). Refer to section 3.3.1 for methods.

Table 4: Sample and completion dimensions. All dimensions in inches.

	Sample Height	Sample Diameter	Borehole OD	Borehole ID	Borehole Depth	Perforation Depth
Sandstone	6.0	4.0	0.25	0.187	4.0	3.0
Shale	2.5	1.8	0.125	0.07	1.5	1.25
Pyrophyllite	6.0	4.0	0.25	0.187	3.5	3.0

The fluid used for hydraulic injection in the uniaxial experiments was Field's metal, which consists of 32.5% Bismuth, 16.5% Tin, and 51% Indium. This metal has a low melting point of 70˚C and is used for its ability to illuminate fracture networks in SEM and CT imaging. A heated transfer vessel was used to hold the metal prior to fracturing. The vessel was made out of 1/4th inch piping and attached to the top of the wellbore. **Fig. 20** shows the experimental setup prior to fracturing. The long pipe stretching from the core to the tubing is the metal filled reservoir. Prior to fracturing, the Field's metal was heated to 100˚C and poured into the vessel to act as a storage device. The cores were placed into an oven at 90˚C to ensure the metal would not rapidly solidify when the metal came in contact with the core during injection.

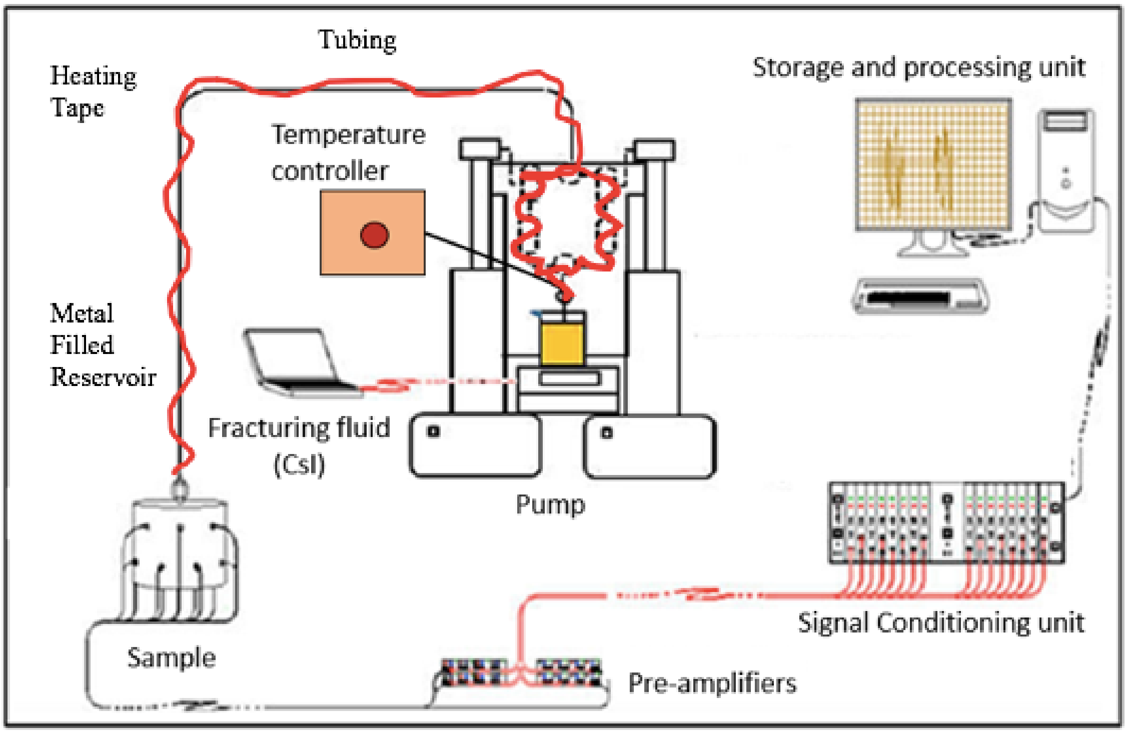

Figure 20: Diagram of the experimental setup excluding the uniaxial loading system (Modified from Damani, 2013).

At the time of fracture, the Isco Pumps were filled with vegetable oil and connected to the metal reservoir. One of the cores were removed from the oven and placed within the uniaxial fracture apparatus. 2000 psi uniaxial horizontal stress was applied to the pyrophyllite sample and 500 psi uniaxial horizontal stress was applied to the shale sample. Significantly less pressure was applied to the shale because of its tendency to fail under low uniaxial pressures. The metal reservoir vessel was then connected to the borehole and heating tape was wrapped around all tubing and heated to 90˚C. While the reservoir was heating, heat guns were placed around the core to keep it warm. Once the reservoir reached 90˚C and the metal returned to liquid state, the Isco pump forced the liquid metal into the formation at a rate of 5 ml/min. Both core samples did not fail during initial pressurization but finally failed after repeated pressure pulsing.

3.3.3 SEM Preparation

To examine the interior of the hydraulic fracture, the core was cut in half, as seen in **Fig. 21a**. The fractures protruding from the perforations were visually documented and 6 plugs were drilled out of the core making certain that the fracture, or fracture tip, resided within the 1” diameter plugs. The plugs were then cut into several discs approximately 1 cm in thickness for SEM analysis. To analyze different angles of the fracture, vertical and horizontal samples were prepared. **Fig 21b** illustrates a 1-inch plug before cutting it into SEM samples. Black marks roughly define cutting locations.

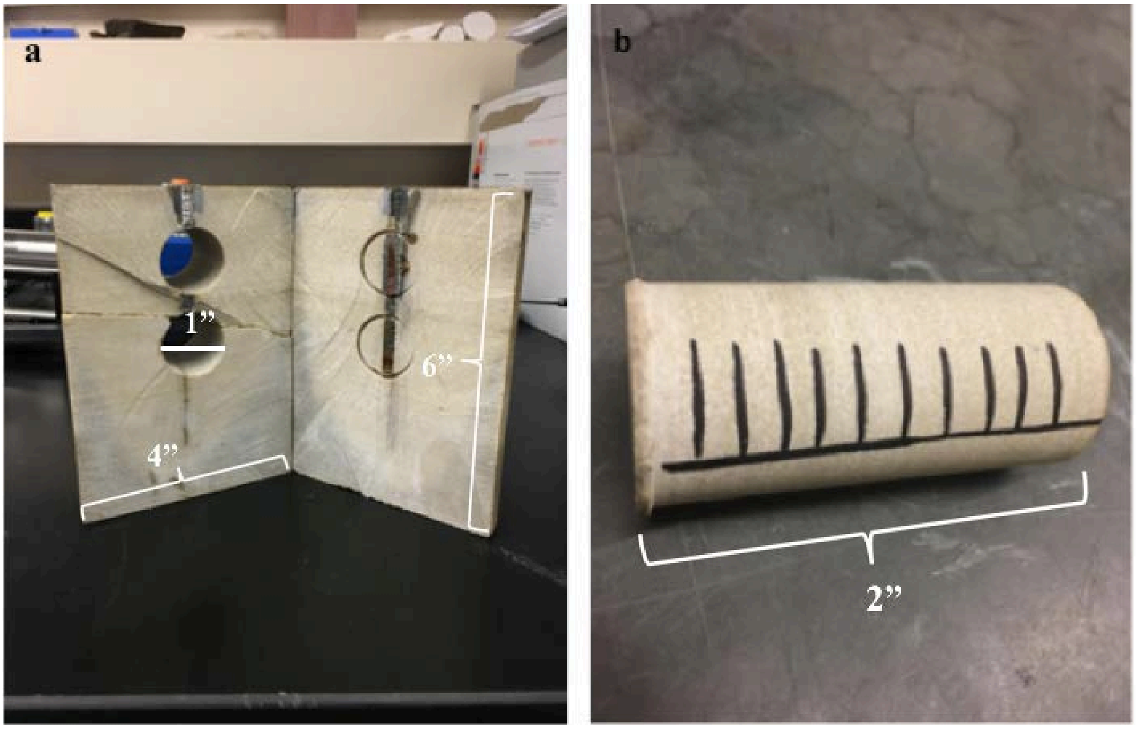

Figure 21: A visual representation of the sandstone core and plug. (a) the fracture can be seen running vertically through the core from the darkness of the imbedded epoxy. (b) Each plug is cut into several SEM samples with a distinct distance from the injection point.

The sandstone samples were polished using a mechanical polisher with 120, 400, 600, and 800 grit emery paper. Shale and pyrophyllite samples were polished by hand, starting at 120 grit to smooth the surface, then applying one sheet of 400, 600, 800, and 1200 grit paper. A model 1060 Fischione™ broad beam argon ion mill was used after paper polishing. For a large surface area, a nine-hour argon milling process at 6 kV and low beam angles were used. In addition, a three-hour milling process at 5 kV is used at high beam angles focused at the center of the sample. Combining both procedures, the surface is evenly polished for analysis. The drawback to using an ion mill is the removal of topography. Depending on what the analysis entails, ion milling is not always desired.

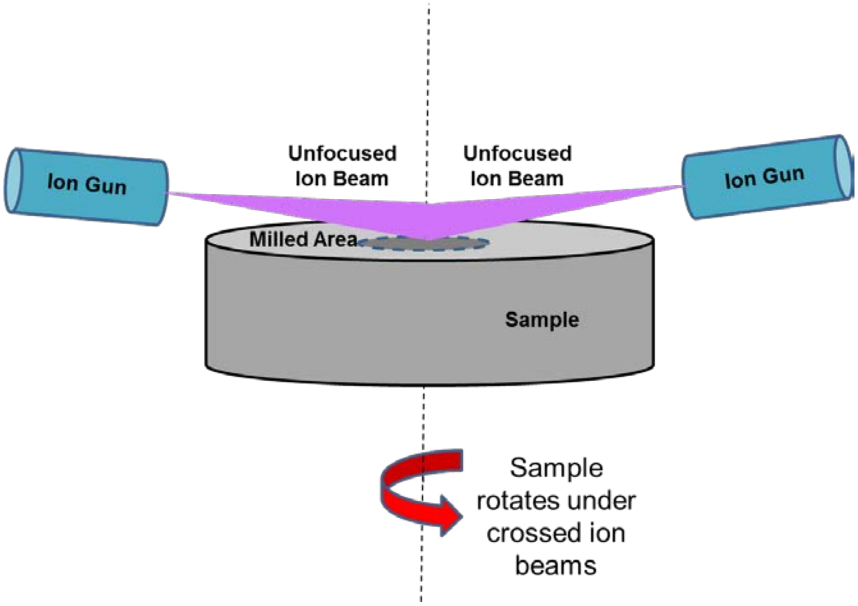

Figure 22: Two Ar ion guns blast the sample surface while the stage rotates, creating a molecularly smooth finish (Curtis, 2017).

For samples that suffer from charging, copper tape is applied with liquid silver around the edges. Once the silver is dry (5 hours), the sample is sputter coated with Au/Pd by a Desk V DENTON Vacuum instrument for four, three-second increments. The benefits to sputter coating include a reduction of charging, increased secondary electron generation, and a reduction of beam penetration (**Quorum Technologies, n.d.)**. Depending on the intensity of charging, not all samples need to be wrapped with copper and silver. Typically, the Au/Pd sputter coat is sufficient. **Fig. 23** shows 12 samples that were analyzed for fracture statistics. **Fig. 23a** shows 8 samples that were used to diagnose the secondary fracture network in the elastic region and **Fig. 23b** shows 4 samples that were used for fracture tip analysis.

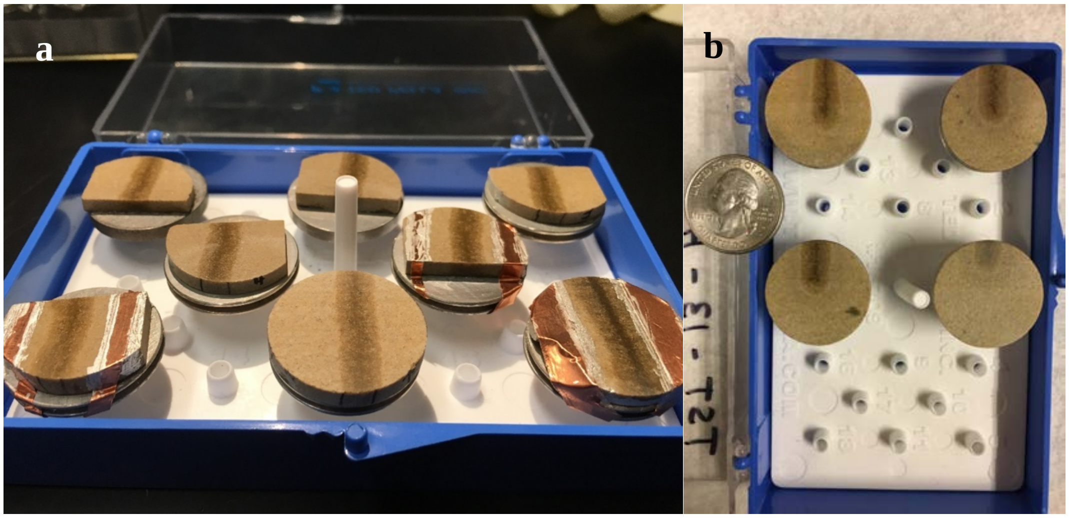

Figure 23: a) Prepared samples ready for SEM analysis. Three out of eight samples were wrapped with copper and liquid silver to reduce charging. b) 4 fracture tip SEM samples. Each sample shows the fracture tip as it gets further away from the injection point. The fracture is recognized by the dark epoxy running down the center of each sample.

3.3.4 SEM Procedure

Imaging was performed on a Helios Nanolab™ 650 DualBeam™ FIB/SEM instrument. Before imaging, the voltage was set to 2.0 kV with a 0.40 nA beam current. The accelerating voltage controls the depth of penetration, however, if set too high can cause a loss of surface material. Finding the optimal voltage is critical for best results. The dwell time was set to 1 μs, frame time 4.8 seconds, and the resolution was set to

1536x1024 pixels. The Everhart-Thornley detector is first used to acquire a quick focus on the sample surface and set working distance to 3 mm. The concentric backscatter (CBS) detector is inserted for its sensitivity to atomic number. Minerals that have a high atomic number (pyrite) appear very bright under the detector, and features that have a low atomic number (epoxy) appear dark. Thus, the CBS detector will expose the epoxy and metal that was injected into the fracture network. Once the detector is in place, the lenses, beam, and detector parameters are adjusted to achieve optimal clarity.

The FEI MAPS software was used for automatic image acquisition and stitching. This software allows a multitude of images to be taken and then stitched together to produce one high-resolution mosaic image. To begin this process, an electron acquisition type is selected. It was determined that the appropriate image size for secondary fracture analysis in sandstone was 5 mm by 4.5 mm. This size was chosen by discovering the maximum distance the epoxy impregnated perpendicular to the primary fracture. The number of images taken varied from sample to sample but averaged about 2,500 per sample. Other image properties included a frame width of 133 μm, dwell time of 3 μs, a 4-frame integration, and a 1536x1024 pixel resolution. The acquisition time for each individual image was 19 seconds and took approximately 21 hours to complete depending on the number of images being stitched together. The focus setting was set to interpolated, which is derived from manual focus points at three different locations around the tileset. This provides optimal clarity given such a large surface area being imaged.

3.3.5 Fracture Counting Procedure

To begin fracture analysis, scan lines parallel and/or perpendicular to the primary fracture were imposed on the image using the measurement tool in the FEI MAPS software. Scan lines are used to give the naked eye something to follow while recording fracture statistics. This guarantees that the data gathering process is uniform for all analyses. Starting at the scan line nearest to the primary fracture: fracture quantity (number), length, width, and azimuth were recorded with respect to distance from primary fracture, fracture tip, and/or injection point. For these experiments the scanlines ranged from 4.5 to 5.5 mm long and the fracture quantity was counted for the entire scanline length. Fracture density is calculated by dividing the number of fractures by a given distance. Fracture length is determined by following the fracture until it branches into separate fractures or terminates. Width is calculated using the software measurement tool and azimuth is taken with respect to the primary fracture. The azimuth will be 0° if the secondary fracture is parallel to the primary fracture and 90° degrees if the secondary fracture is perpendicular to the primary fracture.

The edge of the process zone is reached when injection fluid can no longer be found in the secondary fracture network. Parallel and perpendicular scanlines were spaced 200 µm apart. **Fig. 24** is an example of how parallel scan lines are imposed onto the SEM image.

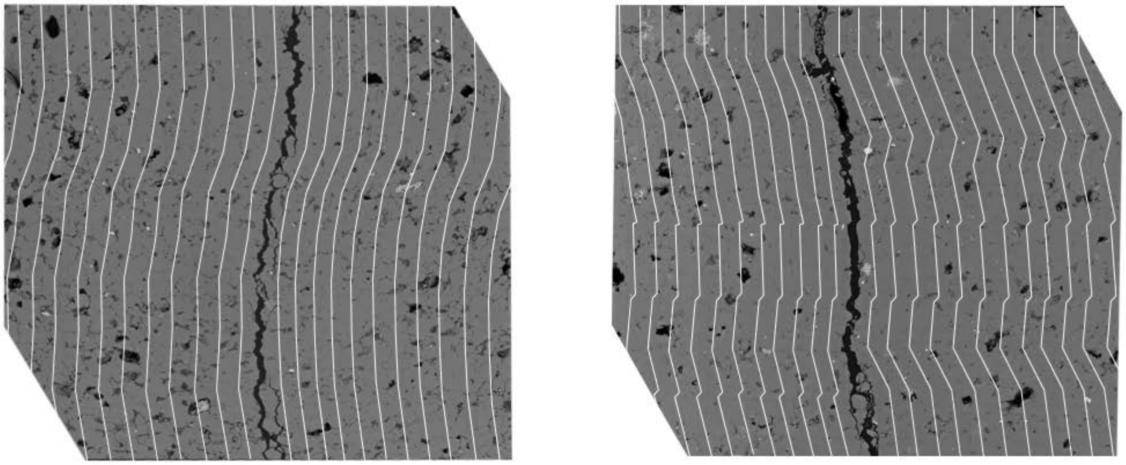

Figure 24: Illustration of parallel scanlines imposed onto two SEM images. The scanlines are bent in accordance to the primary fracture. This is to maintain constant distance from the primary fracture. A 200 μm spacing was implemented between scanlines.

For fracture tip experiments, parallel, perpendicular, and radial scanlines were used. **Fig. 25** shows the grid system for fracture tip analysis. Behind the fracture's termination point, a square grid system is imposed onto the image with parallel and perpendicular scanlines, creating 200 by 200 μm squares. In front of the termination point parallel scanlines continue and radial scanlines move outwards at 10-degree increments. **Figure 7** illustrates the Von Mises and Tresca diagrams for normalized fracture tip geometries.

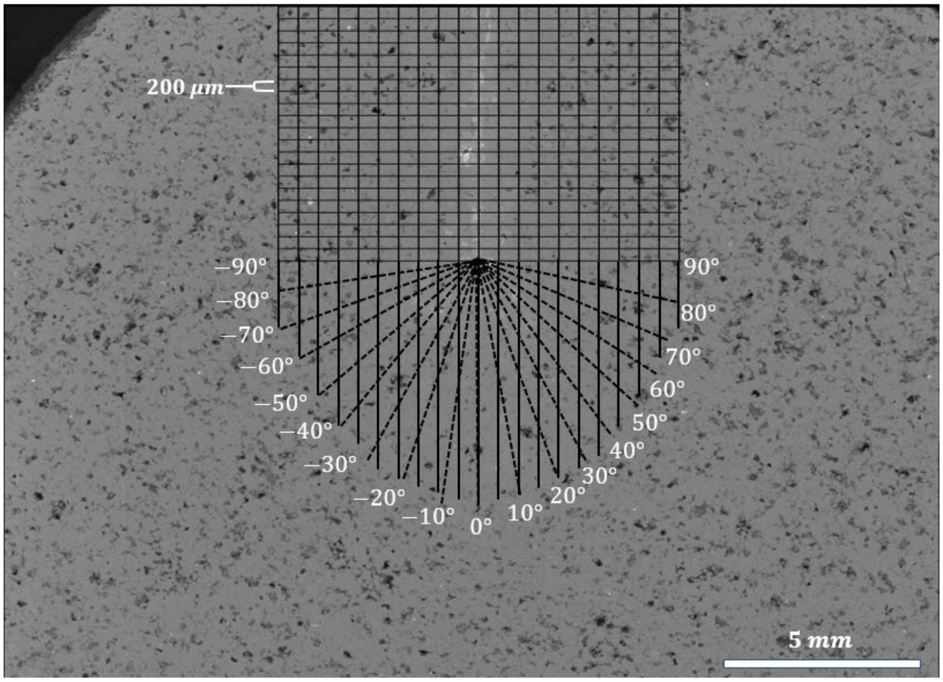

Figure 25: Fracture tip grid system used for fracture counting on an SEM image.

Tennessee sandstone has an average grain size of 80 µm and the secondary fractures typically range in width from 0.5 µm – 3 µm. **Fig. 26** displays an SEM image of a primary fracture running vertically with a series of secondary fractures extending into the formation. At first glance, the secondary fractures appear to be following the grain boundaries without much deviation. However, the displayed SEM mosaic is 1220 µm wide by 770 µm tall with a resolution of 1536x1024 pixels, which does not allow small secondary fracture to be seen. To solve this problem, a decrease in surface size or increase in resolution is necessary. **Fig. 27** shows a magnified image (22 µm by 13 µm) of a secondary fracture (resolution 1536x1024) that could not be seen in **Fig. 26**. This fracture is approximately 2 µm wide and contains the injected epoxy from the fracturing procedure. Because this fracture contains epoxy, it is stimulated by the hydraulic fracture and is considered for statistics. Notice that the epoxy does not uniformly fill the fracture.

This is hypothesized to be due to one of two reasons; 1) there was air within the sample when injection took place, or 2) the epoxy is non-wetting to the rock surface and is beading up before the epoxy could cure. The black arrows on the SEM images represent the stresses applied during the triaxial fracture. Notice the primary fracture is propagating in the direction of maximum horizontal stress (2000 psi) and upwards in the direction of vertical stress (3000 psi).

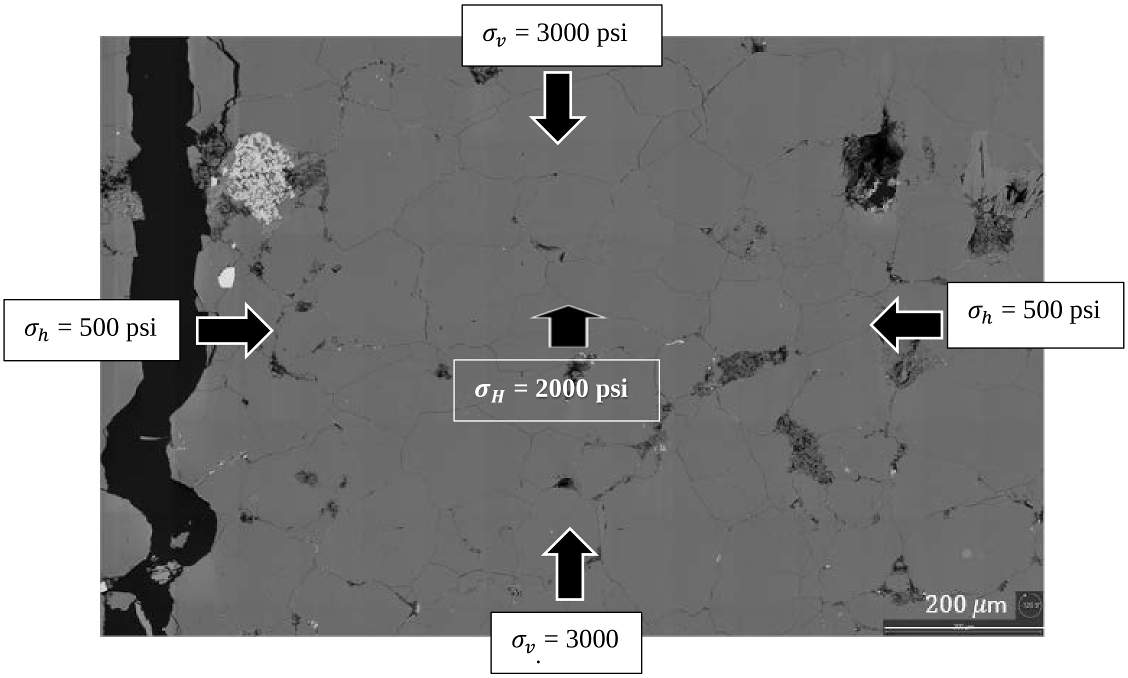

Figure 26: Secondary fracture network extending into the formation. 1220 µm wide by 770 µm tall mosaic with a 1536x1024 pixel resolution, the secondary fractures appear to be following the grain boundaries successfully. Black arrows represent the stress orientation and magnitude of the triaxial experiment.

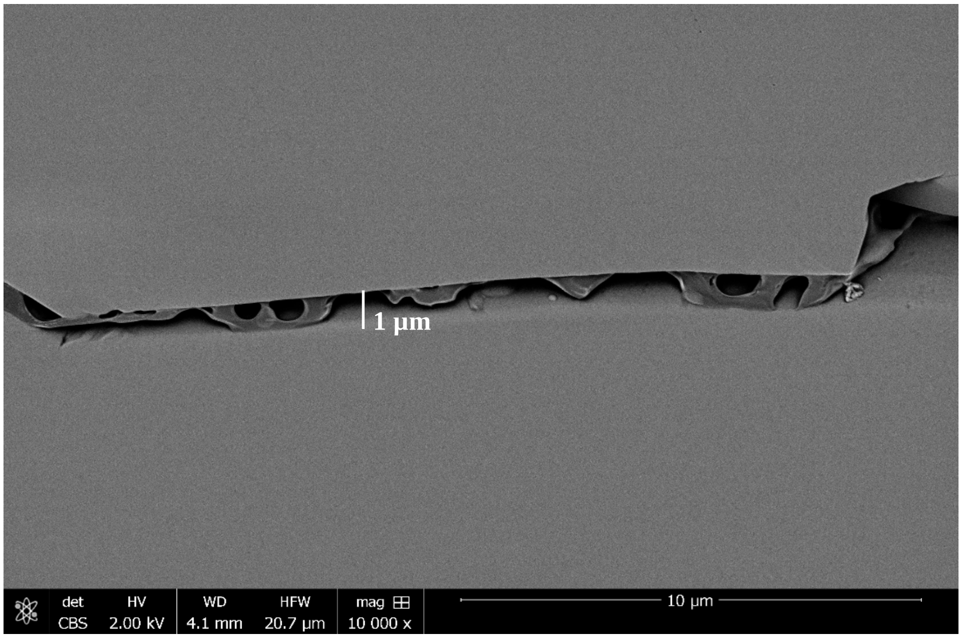

Figure 27: Close-up of a secondary fracture, revealing the injected epoxy. Presence of injected epoxy verifies hydraulic stimulation and is therefore counted towards SRV statistics.

Fracture counting was conducted on 25 prepared SEM samples that were extracted from 9 plugs within the Tennessee sandstone, Marcellus shale, and pyrophyllite. Vertical and horizontal plugs were taken to view the fracture from different orientations. Vertical samples provide a constant distance from the injection point and allow analysis along the vertical plane, while horizontal samples show the continuous change with distance from injection point.

3.3.6 Twinning Procedure

Sample preparation for the twinning experiments is the same as SEM preparation with the exception that the samples were not sputter coated. This is because the Au/Pd that covers the samples interferes with the EBSD’s ability to read the crystal’s diffraction patterns. However, if necessary, carbon coating can be performed.

Twinning analysis was first conducted on an unstressed, native Tennessee sandstone sample. The selected region was studied in a Zeiss NEON FEG-SEM dual beam high resolution SEM at 25kV, 100µA beam current, 5nA probe current, with a working distance of 15-25mm. The stage was brought to a 70° inclination and the diffraction patterns were analyzed. The area of study was 200 µm by 250 µm scanned in 1 µm steps. The second test was conducted on a hydraulically fractured Tennessee sandstone using the same instrument. The area of study was 130 µm by 200 µm and located 10 µm from the primary fracture, which was chosen due to the high damage and excessive intragranular fractures, confirming a high energy zone.

Apart from using Oxford Software instead of BEARTEX, the methods for this experiment are outlined by **(Wenk et al., 2011)**. Without BEARTEX, over laying the twin boundaries onto SEM images could not be done; however, the presence of Dauphiné twins can still be proven.

Chapter 4: Results and Discussion

4.1 Tennessee Sandstone Secondary Fracture Network

4.1.1 Symmetry

Statistical analysis was performed on both sides of the primary fracture to capture secondary fracture symmetry. This process was performed to save time in future experiments by running fracture analysis on one side of the fracture instead of two. The result of the symmetry test was also applied to the pyrophyllite and shale experiments.

Statistical analysis was performed on 6 vertical samples. **Fig. 28** shows a strong correlation between the number of fractures and distance from primary fracture for both wings. Welch's t-test was used for analysis since the data had unequal variances and/or unequal sizes. The two-tailed P-value gave a 0.625 average, which is much higher than the statistically significant difference of 0.1. It was determined that there is a strong correlation in secondary fractures between both sides of the primary fracture.

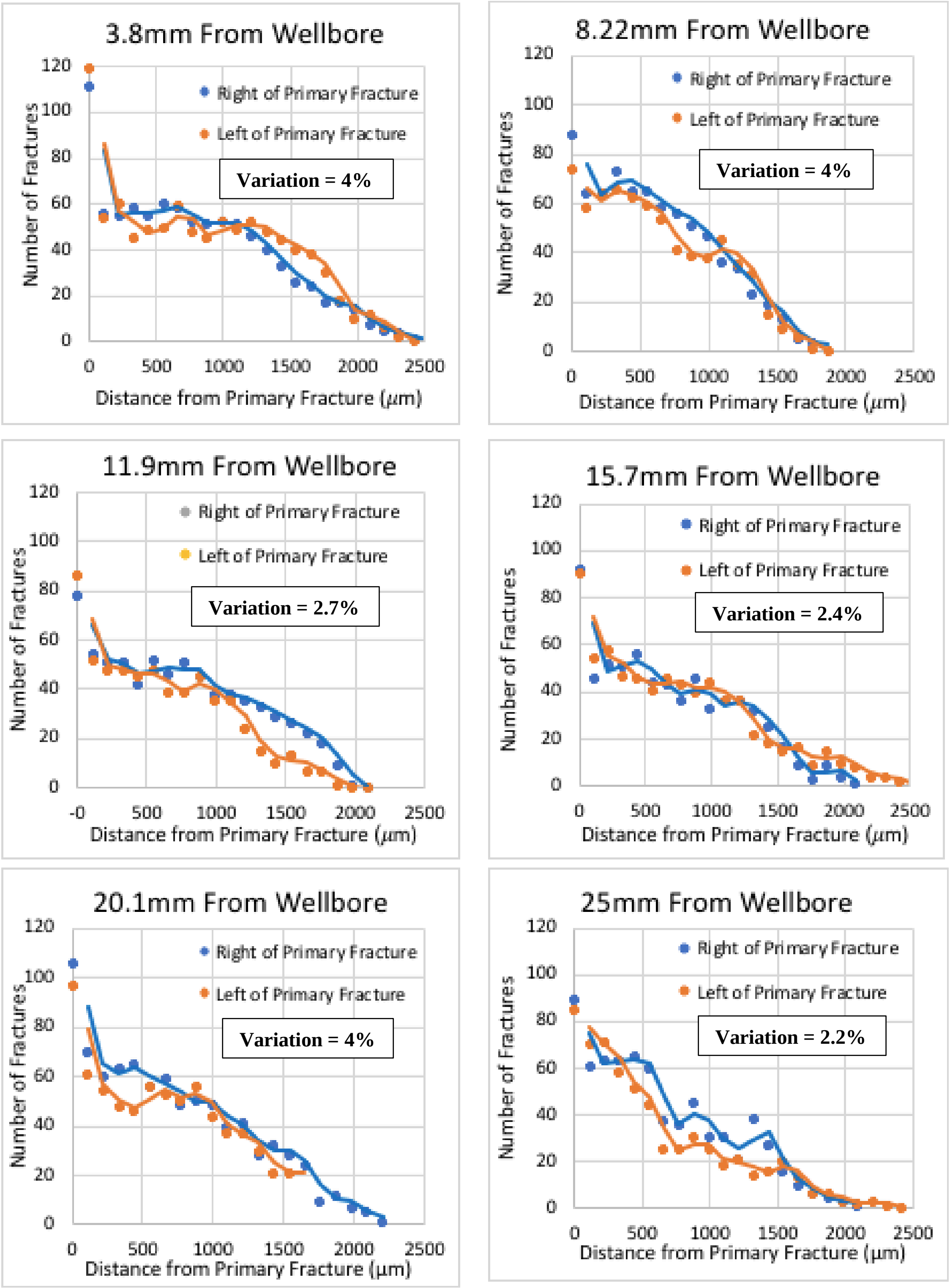

Figure 28: Statistical analysis regarding fracture symmetry on either side of a primary fracture. All samples show high secondary fracture density near the primary fracture and decrease at a fairly constant rate. Welch's t-test confirmed symmetry.

4.1.2 Secondary Fracture Orientation (Azimuth)

Fracture propagation is highly dependent on the velocity of the fracture. The primary fracture, which travels the fastest, propagates through grains in the direction of maximum stress. In contrast, the secondary fractures act orthogonal to the maximum stress load and propagate perpendicular to the primary fracture. **Atkinson (1987)** showed that the lower the velocity, the lower the stress intensity factor (K), and fractures would more likely follow grains boundaries instead of propagating through grains (**Fig. 29**). However, **Fig. 30** shows that despite low velocity, majority of secondary fractures propagate 90° from the primary fracture and do not change with distance from injection point for the triaxial experiment. The 90° orientation of the secondary fractures is most likely due to the triaxial load on the rock. A 2000 psi transverse stress controlled the propagation of the primary fracture while the 500 psi confining stress dictated the secondary fracture orientation. This observation was also seen on a macroscale by **Brace and Bombolakis (1963)**, who determined microfractures propagate normal to the direction of least principal stress. The findings that secondary fracture orientation did not change with distance from injection point suggests that the energy levels associated with the secondary fractures remain constant as the energy levels within the primary fracture decreases, maintaining a strong secondary fracture network (for a finite fracture geometry of a 2” bi-wing). This observation was seen in all samples of the Tennessee sandstone.

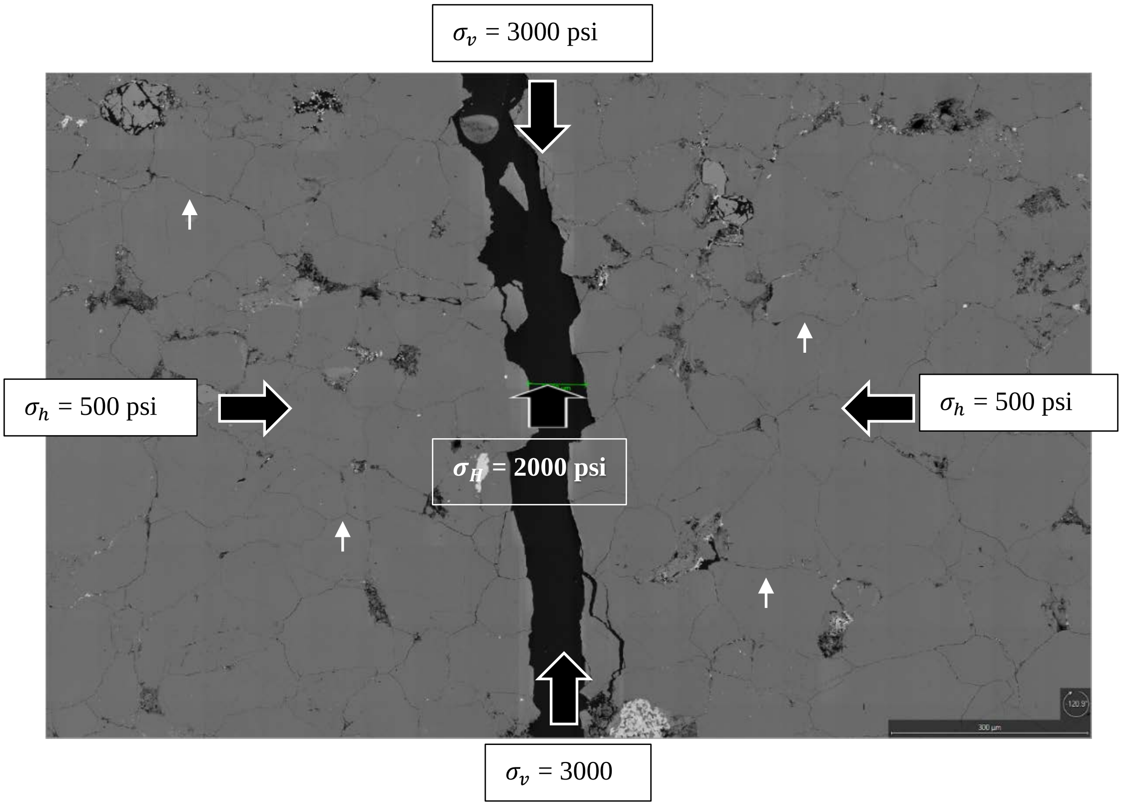

Figure 29: Back scattered electron (BSE) image showing the intragranular nature of the primary fracture and the intergranular nature of the secondary fractures. This process is due to the energy distribution between primary and secondary fractures. Four secondary fractures are illustrated by white arrows. Black arrows represent the stress orientation and magnitude of the triaxial experiment.

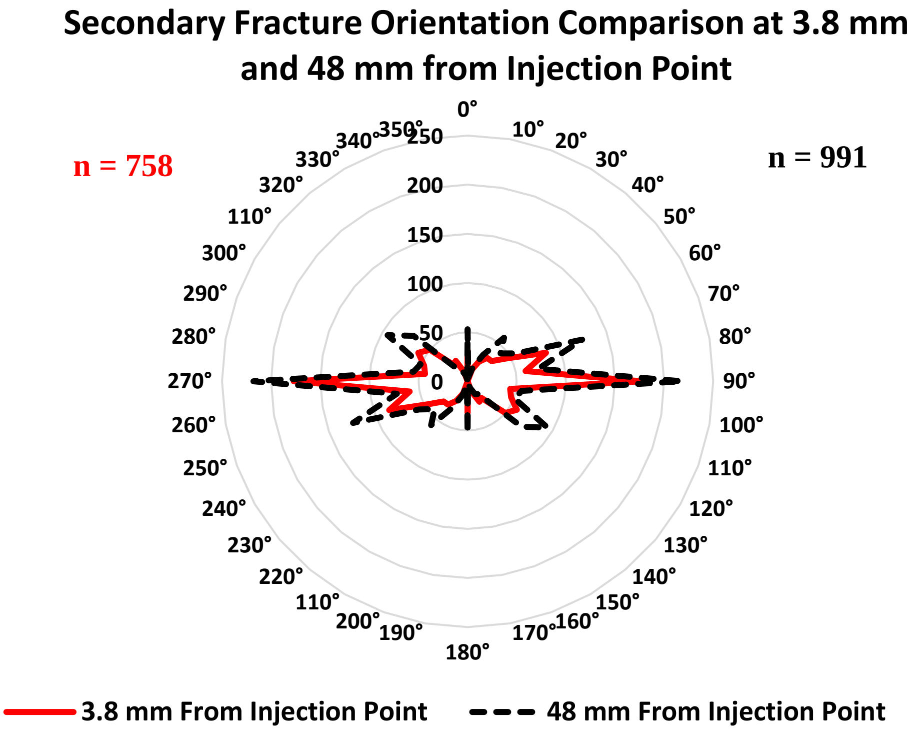

Figure 30: Secondary fractures observed 3.8 and 48 mm from the injection wellbore. A dominate trend of 90° can be seen for both secondary fracture locations. 758 fractures were counted 3.8 mm from wellbore and 991 fractures were counted 48 mm from wellbore. Secondary fracture azimuth is in relation to the primary fracture where 0° and 180° is parallel to primary fracture and 90° is perpendicular to primary fracture. This figure shows 0°- 360° and thus, 180°- 360° is a mirror of 0°- 180°.

4.1.3 Process Zone

The process zone length is defined by the distance that the secondary fractures extend into the formation. This distance is found by determining the maximum distance of epoxy injection. **Fig. 31** shows the process zone length variation along the distance from the injection point. It can clearly be seen that there is a cyclical pulsation effect in the process zone. As the fracture propagates away from the injection point, the process zone dimensions increase and decrease. This effect correlates with the increasing and decreasing width of the primary fracture. Looking at **Fig. 32**, the fracture width is approximately 40 µm, which is slightly smaller than the value reported by **(Damani et al., 2013)** but still consistent, and the process zone is between 2090 and 2310 µm. In **Fig. 33**, the fracture width increases to 70 µm and the process zone increases to 2420 µm.

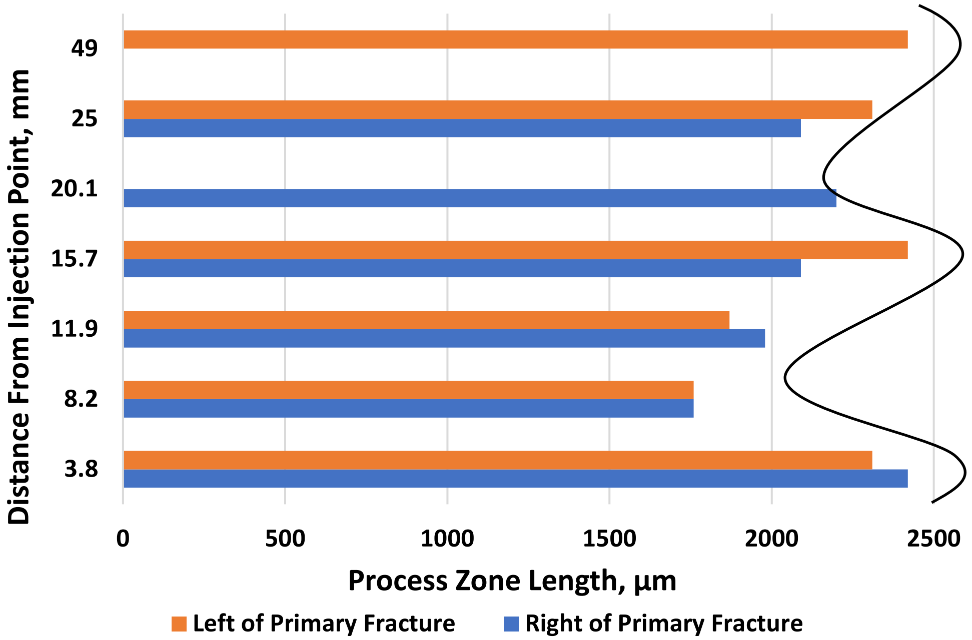

Figure 31: A cyclic process zone size with distance from injection point. The process zone length fluctuates in pulsating patterns as it propagates away from the injection point. these pulsations correlate with the primary fracture width.

It is hypothesized that the pulsation effect in the fracture width and process zone are due to the velocity of the primary fracture. The primary fracture does not propagate with constant velocity, but rather in incremental periods of acceleration and deceleration associated with the build-up and release of energy. During the pressure build-up period, the fracture width and process zone decline until the energy is released, which widens the fracture, extends the fracture and increases the process zone. The velocity, along with the stress intensity factor and fracture morphology, provide information about fracture propagation **(Bahat, 1991)**. The pulsations seen here indicate low velocity due to the incremental movements during fracture propagation. A high velocity fracture would result in a more uniform propagation pattern.

The cause of velocity fluctuations within a primary fracture is due to one of three reasons: 1) an infiltration of pore fluid into the primary fracture suddenly raises fracture pressure and increases fracture propagation velocity, 2) the compressibility of the fluid inside the fracture expands, increasing propagation velocity, or 3) the fracture fluid is slower than the fracture tip, causing the tip to outrun the fluid inside the fracture until the tip no longer feels the stress generated by the fluid; it will then wait until the fluid catches up to repeat the process **(Engelder, 1987; Lacazette and Engelder, 1992).** Because the saturation and pore pressure of the core was low in comparison to the injection pressure, the first hypothesis for intermittent fracture growth can be ruled out. In addition, because the injection fluid was epoxy, the expansion rate during fracture propagation would be minimal, and the second hypothesis does not satisfy our conditions. However, the third condition could be true due to the high viscosity of the injected epoxy (65 cP) slowing the fracturing fluid and allowing the fracture tip to propagate faster than the fluid. This hypothesis would explain the energy pulsations within the process zone and primary fracture widths.

Intermittent fracture growths can be seen on a macroscale as well as in microscale. **Lacazette and Engelder (1992)** observe cyclic propagations in the Devonian Ithaca Siltstone, where they found plumose morphologies with multiple arrest lines. In their study, it was determined that the expansion of natural gas in the propagating fracture caused fluctuations of fracture velocity. Their fracture pulsations were 0.6-1.0-meter-long over a 28-meter exposed finite outcrop, whereas this study showed fracture pulsations of 5-10 mm long over a 51 mm finite sample.

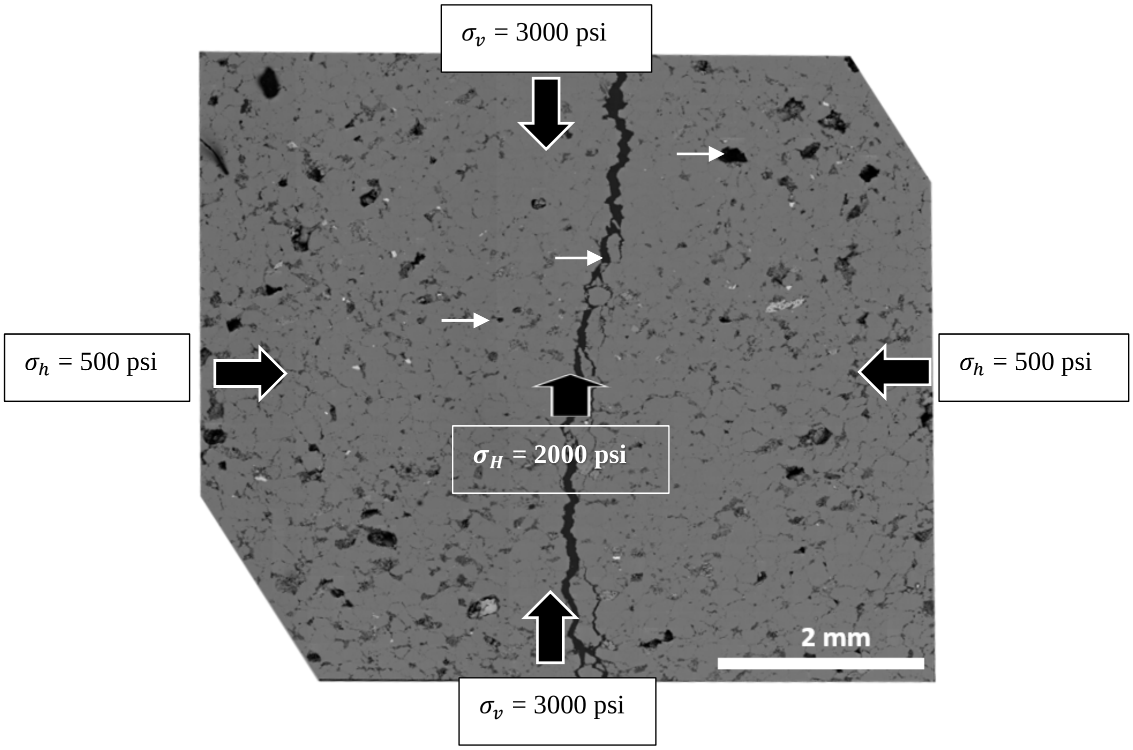

Figure 32: Vertical sample taken 25mm away from the wellbore. Notice that the width of the primary fracture is small, indicating a relaxation of energy before another pulse. The injected epoxy can be seen as the dark color contrast filling the primary fracture and pore space, represented by white arrows. Black arrows represent the stress orientation and magnitude of the triaxial experiment.

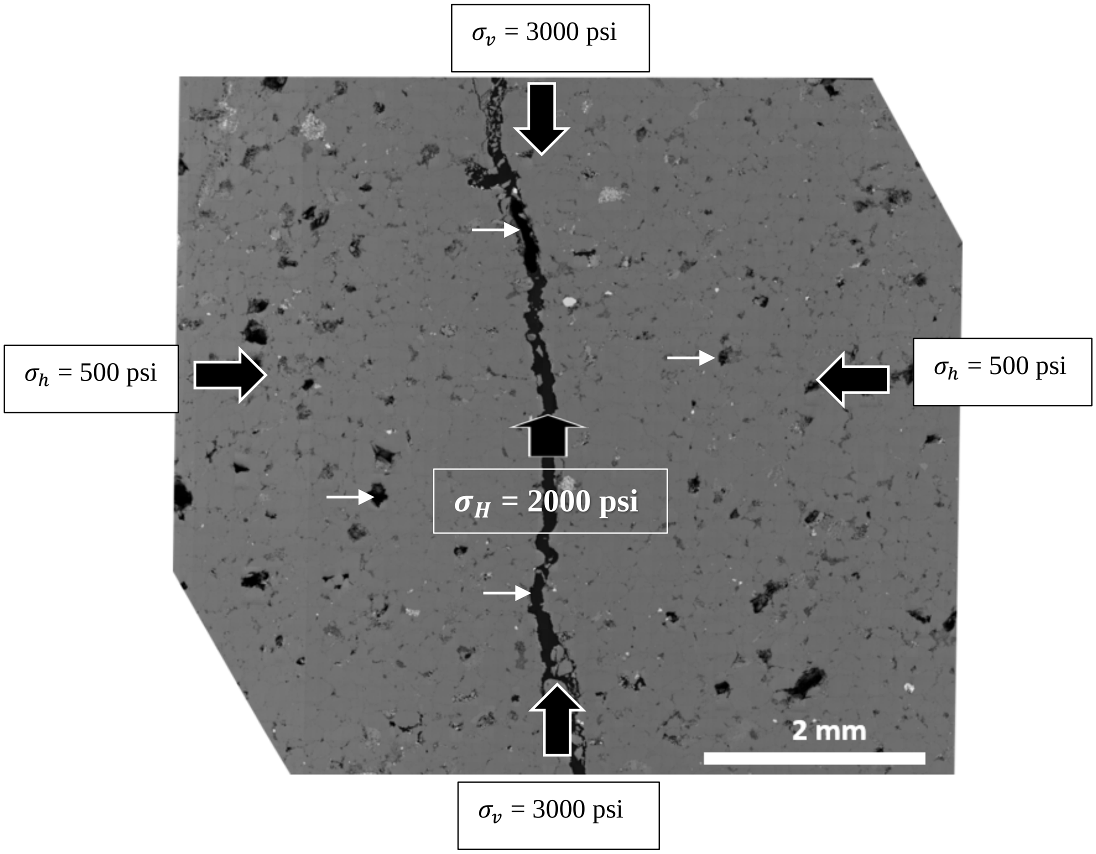

Figure 33: Vertical sample taken 49mm from wellbore. Notice the width of the primary fracture is large, indicating the beginning of a pulse, where energy is high. The epoxy can be seen as the dark contrast within the primary fracture and pores, represented by white arrows. Black arrows represent the stress orientation and magnitude of the triaxial experiment.

The energy distribution during fracture propagation was also reflected in intragranular fracture densities. Intragranular fractures are produced in high energy zones where the fractures can overcome the grain boundaries and break through the grain. Therefore, it would be expected that there would be more intragranular fractures when the primary fracture width widens, and the process zone is large. Indeed, it is seen in **Fig. 34** that there is a correlation between process zone length and intragranular fracture density. This correlation is consistent with the energy distribution pattern during fracture propagation.

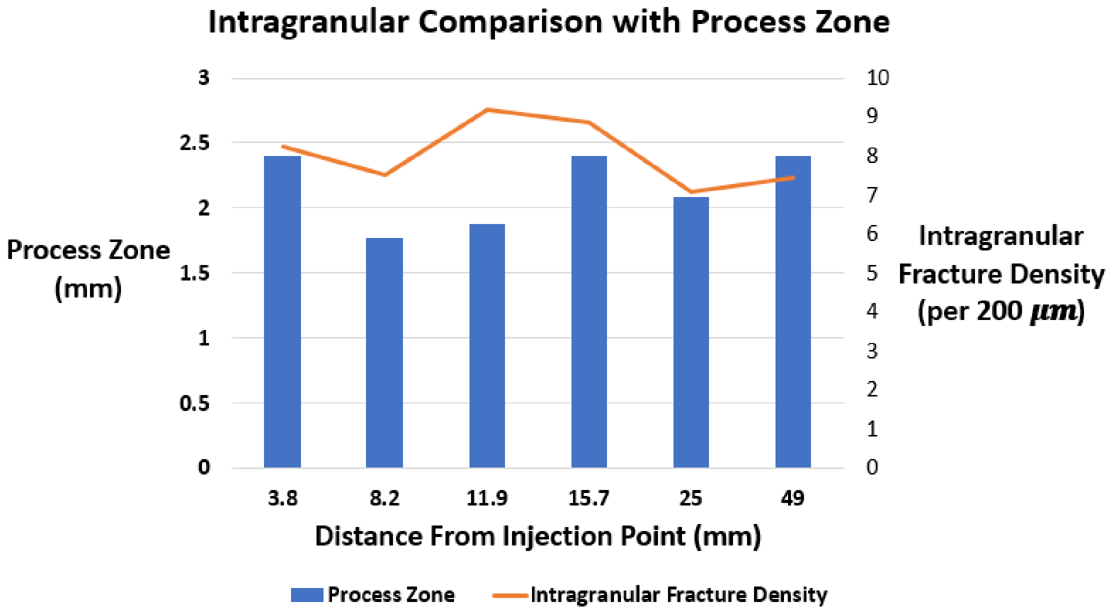

Figure 34: The process zone and intragranular fracture density on the Y1 and Y2 axes show a correlation with distance from injection point. The intragranular fracture density was measured with perpendicular scanlines every 200 µm as was the process zone. The simultaneous increase and decrease of process zone and intragranular fractures define high energy zones during fracture propagation.

Aside from the cyclic nature of the process zone, it was observed that the general size of the process zone did not decrease with an increase in distance from the injection point in our finite dimension sample of 2” biwings. The process zone at 3.8 mm from injection point is the same as the process zone at 48 mm from injection point. This suggests that the decrease in stored energy in the primary fracture during propagation does not significantly affect the distributed energy to the secondary fracture network. Whether there is high energy (near injection point) or low energy (near termination point), the secondary network remains constant, despite the fluctuations from primary fracture propagation. This behavior is odd and may be an artificial consequence of the finite sample dimensions.

4.1.4 Quantity

The fracture density is an important aspect to reservoir stimulation along with the fracture orientation and location. The higher the density of fractures, the higher the chance that pores will be interconnected and production rates will rise. In this experiment, the scanlines were imposed parallel to the primary fracture, 5 mm long with 120 µm spacing (e.g. **Fig. 24**), to determine the extent of reservoir stimulation with respect to distance from primary fracture and distance from injection point. **Fig. 35** demonstrates the reduction of secondary fractures with increasing distance from the primary fracture. The secondary fracture network decreases at an approximate rate of 33 fractures per millimeter from the primary fracture. This rate disregards the initial high density of fractures at zero distance from the primary fracture due to the abundance of secondary fractures that reconnect with the primary fracture and never penetrate further than 20 or 30 µm into the formation.

The initial hypothesis was that the secondary fracture network would decrease with distance from the primary fracture and with distance from the injection point, but results show that secondary stimulation did not decrease with distance from injection point. In fact, the number of secondary fractures was found to be highest 49 mm from injection point (sample boundary). It is possible however, that the fracture was affected by the sample boundary, even though fairly consistent results are found throughout all distances from injection point. The quantity of secondary fractures with distance from injection point can be correlated to the pulsation patterns of fracture propagation. **Fig. 31** shows that the largest process zones were 3.8 mm and 49 mm away from injection point, and **Fig. 35** shows that 3.8 mm and 49 mm also have the greatest number of fractures. It is logical that the largest process zones would also contain the greatest number of fractures.

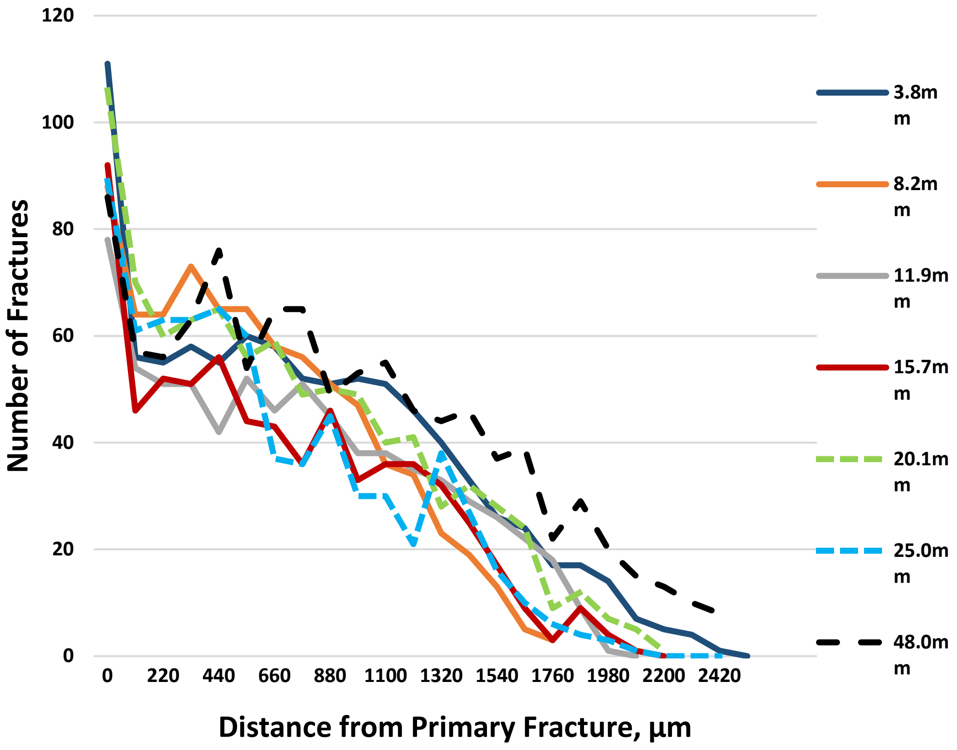

Figure 35: Number of fracture with respect to distance from primary fracture and distance from wellbore. Data was collected using parallel scanlines (with respect to primary fracture) 5 mm long and 110 µm spacing between scanlines (which explains the x-axis). This graph illustrates a constant decrease in the number of fractures with distance from primary fracture. However, it does not show a decline in the number of fractures with respect to distance from injection point.

4.1.5 Density and Spacing

The fracture density (ρ_F) is calculated by simply dividing the number of fractures along a scanline by the scanline length. This gives the number of fractures per 1 mm. **Fig. 36** displays fracture density against distance from primary fracture. These measurements are taken by parallel scanlines, determining the declining rate of fracture density as they propagate perpendicular to the primary fracture. A polynomial function best captures the decrease in fracture density with distance from primary fracture. The average spacing is calculated by $\frac{1}{\rho_F}$ and illustrates the average distance between each fracture. An exponential function best fits these data. Although the secondary fracture density decreases with distance from the primary fracture, the density of secondary fractures remain constant with distance from injection point.

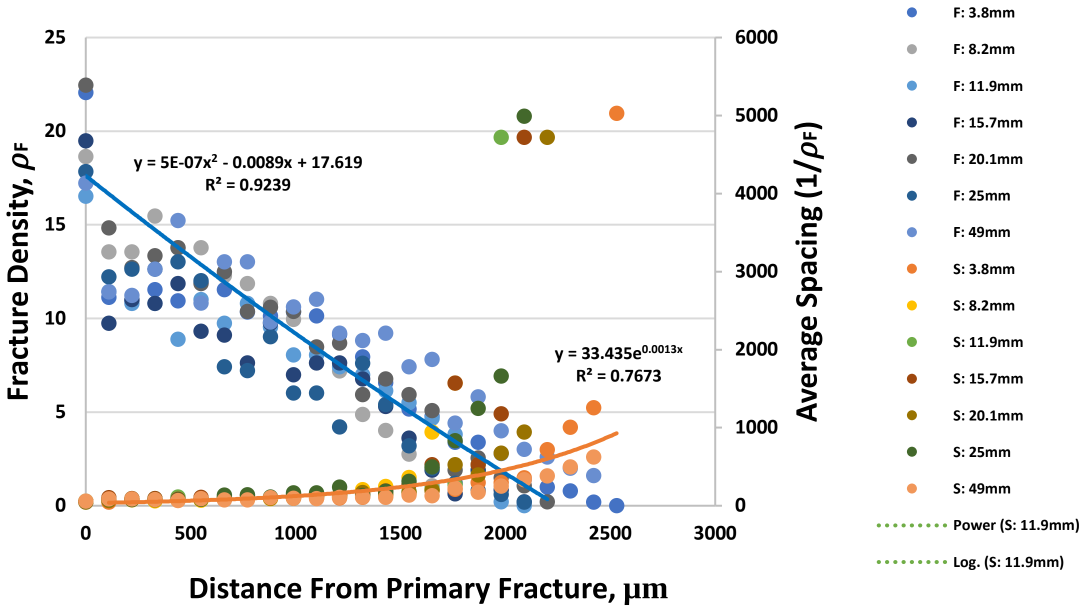

Figure 36: Fracture density shows a constant decrease with increasing distance from primary fracture. In contrast, the average spacing between fractures shows an exponential increase with distance from primary fracture.

4.1.6 Stimulated Reservoir Area (SRA)

Unlike the process zone, which is the total secondary fracture geometry that extends into the formation, SRV is the connected volume of all the individual fractures and pores. Stimulated reservoir area (SRA) is being used to replace SRV because we are limited to 2D images. See **Fig. 37** for an illustration of the process zone and SRA.

SRA is easily calculated once the length, width and number of fractures are known. **Table 5** illustrates the SRA calculated from a vertical plug 1" in diameter and 3.8 mm from the injection point. Comparing rows 1 and 3, one can see the importance of the secondary fracture network. A 4.5 mm long section of the primary fracture, with a primary fracture width of 60 μm, stimulated an area of 0.27 mm^2. However, the secondary fracture network, which branches from the primary fracture and connects a series of pores, was found to add an additional 0.710 mm^2 to the SRA over the same 4.5 mm section. This changes the initial SRA of 0.27 mm^2, if only the primary fracture is counted, to 0.982 mm^2 when adding the secondary fracture network. Thus, tripling the calculated SRA. See **Fig. 37** for an illustration of this data.

Table 5: SRA statistics for primary and secondary fractures, pore space, and pore connectivity. SRA and induced porosity have little variation but the variation among the average secondary fracture width and length are significant. Total secondary fracture length does not have variation because the sum of all secondary fracture lengths was only performed once. Ratios were considered without variation. Because statistics were drawn from one SEM mosaic (approximately 3,000 SEM images and 4.5 mm in length) the variation within the primary fracture will be small.

SRA Statistics from One SEM Mosaic Image		
1	**Primary Fracture SRA (mm^2)**	**0.27 ± .01**
2	**Secondary Fracture SRA (mm^2)**	**0.171 ± .001**
3	**Total Secondary SRA (fractures + porosity) (mm^2)**	**0.710 ± .003**
4	**Primary/Secondary SRA Ratio**	**0.376**
5	**Secondary Induced Porosity (mm^2)**	**0.539 ± .002**
6	**Fracture/Porosity SRA ratio**	**0.316**
7	**Total Secondary Fracture Length (mm^2)**	**110**

8	**Average Secondary Fracture Width (µm)**	**1.9 ± 2.4**
9	**Average Secondary Fracture Length (µm)**	**64 ± 38**

Comparing rows 2 and 3, one can see that the majority of SRA is not coming from the secondary fractures but from the pore space that is being connected to the fractures. A comparison between rows 2 and 5 shows that only 32% of the secondary SRA is coming from the secondary fractures and 68% of secondary SRA is coming from the pore network. This finding reveals that the role of stimulation is not in the fracture volume but the fracture length. Thus, instead of analyzing the stimulated area, it may be more accurate to measure the fracture’s ability to connect pores. As shown in row 7, the combined secondary fracture length is 110 mm compared to the 4.5 mm from the primary fracture. This is 24 times the primary fracture length. The average secondary fracture width is 1.9 ± 2.4 µm compared to the primary fracture width of 48 ± 21 µm, and the average secondary fracture length is 64 ± 38.7 µm.

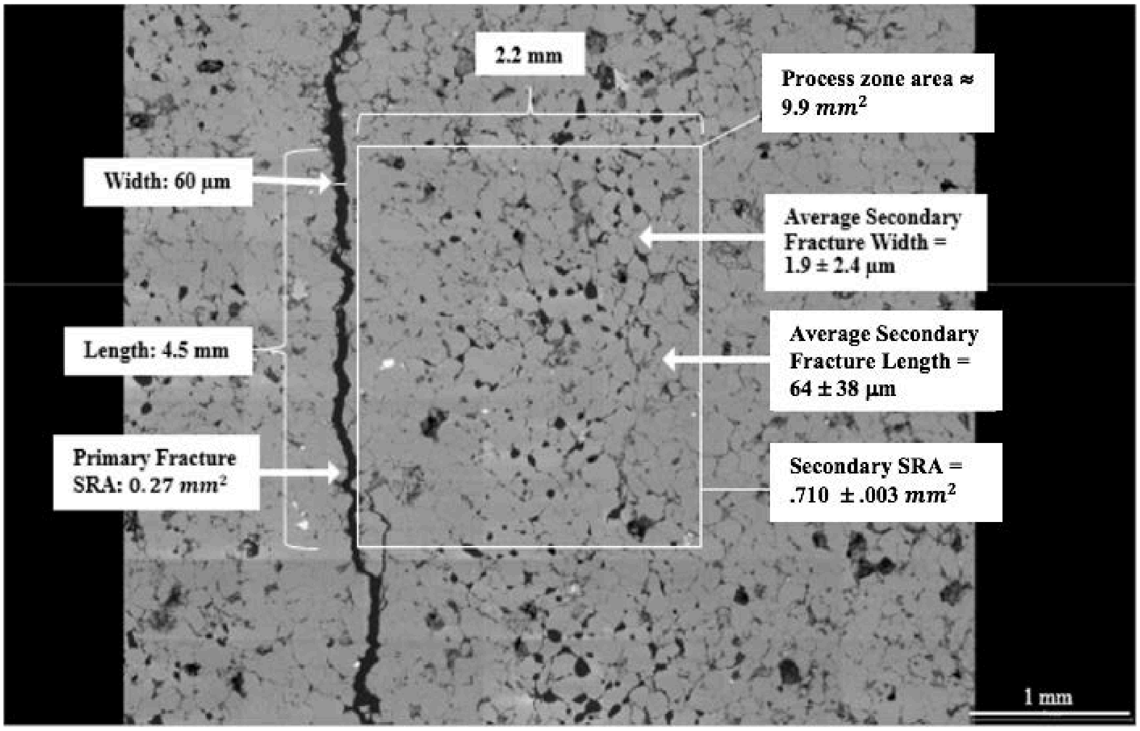

Figure 37: An SEM mosaic of 63 images showing the dimensions and SRA of the primary fracture and the dimensions and SRA of the secondary fracture network and process zone. The process zone length (2.2 mm) is an average of the cyclical pattern, which fluctuates between 1.8 mm and 2.4 mm.

The sample in **Fig. 37** shows a strong decrease in porosity immediately adjacent to the primary fracture, suggesting compaction. This compaction was found in only one SEM mosaic and is not continuous along the fracture.

4.1.7 Upscaling

Zang and Stephansson (2010) plotted process zone width against fault length for natural fractures. They include thrust, normal, and reverse faults, which admittedly differ from hydraulic fractures. Bhagat (2012), used this graph to evaluate laboratory observations and scale them to the field. Plotting the current work on the graph shows a potential upscaling correlation. These results suggest that the current laboratory work can be upscaled to field level.

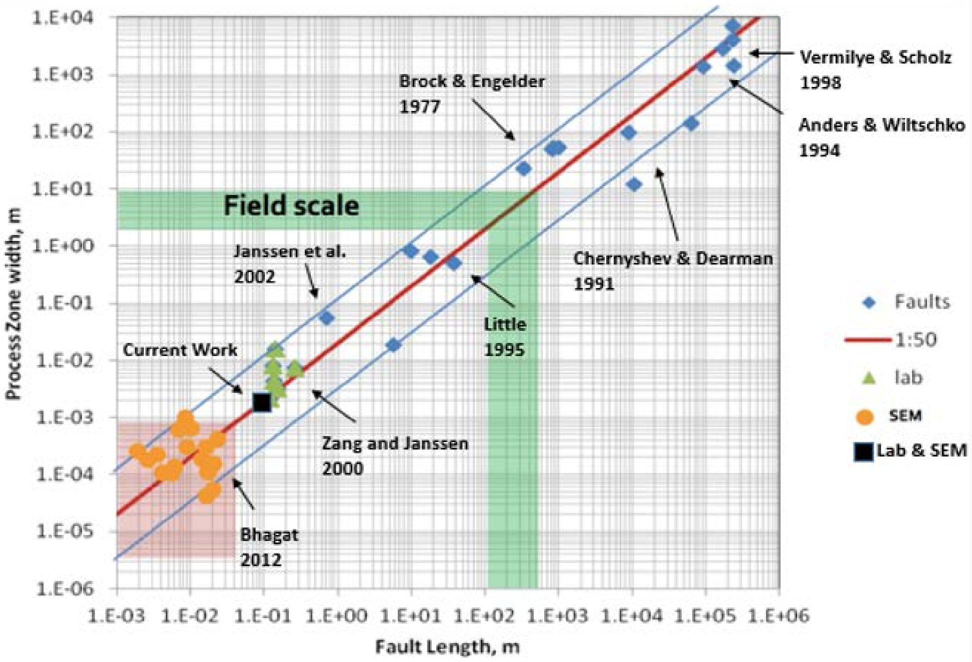

Figure 38: Upscaling procedure for the elastic zone of a triaxial fractured sandstone conducted under a laboratory setting (Zang and Stephansson, 2010; Bhagat et al., 2012).

4.2 Tennessee Sandstone Fracture Tip

The area of study for the fracture tip experiment is shown in **Fig. 39.** Image ‘a’ shows the primary fracture propagating down the core. The ability to stop a hydraulic fracture before reaching the edge of the sample is difficult, and thus being able to analyze the entire fracture is unique. In this experiment, an accurate depiction of the difference between the elastic and plastic zones is seen with the help of the epoxy filled networks.

In **Fig. 39**, the cured epoxy highlights the primary fracture with a darker shadow zone. Observing **Fig. 39b**, a darker silhouette around the primary fracture can be seen. This silhouette represents the epoxy that has intruded into the secondary fracture network. The area of study is the point of elastic/plastic transition and the surrounding regions. In this section we will discuss the effects of plastic fracture mechanics and how they relate to the linear elastic fracture mechanics (LEFM) with the help of SEM.

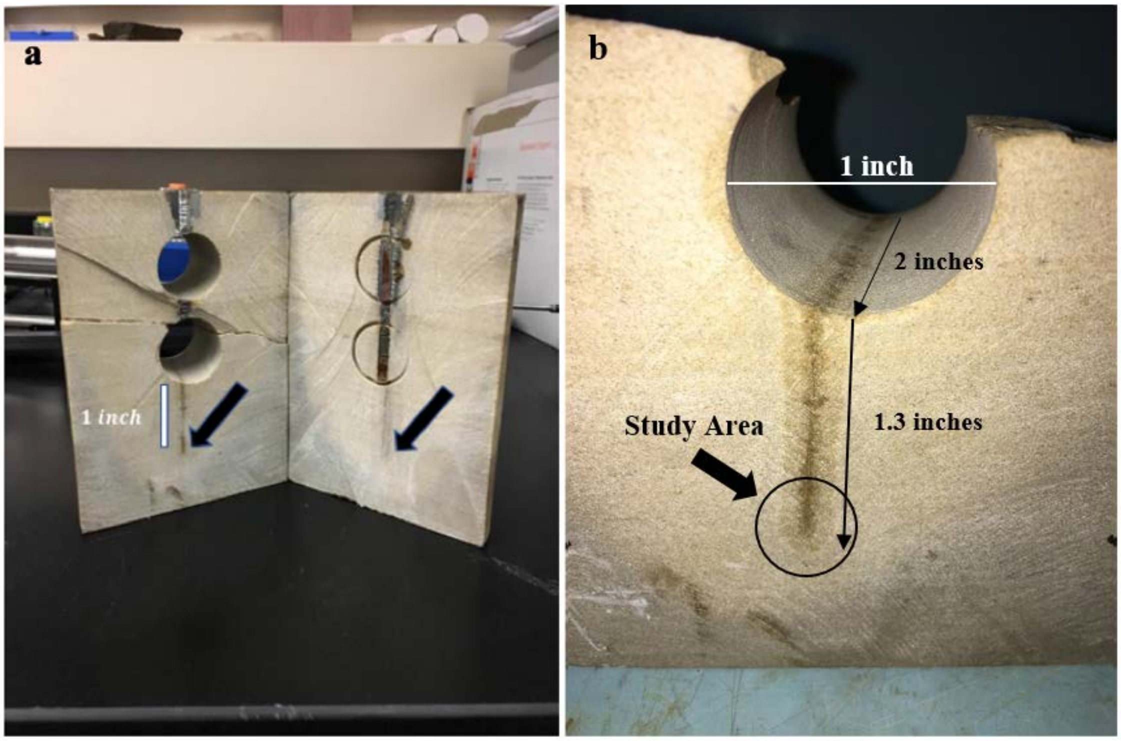

Figure 39: Two images revealing the primary fracture impregnated with epoxy. Image A displays the bi-wing fracture on both sides of the borehole. Image B shows a dark silhouette around the primary fracture, illustrating the secondary fracture network.

4.2.1 Process Zone

The process zone, which is the area that the secondary fractures protrude into the formation, was determined by counting fractures along perpendicular scanlines from the primary fracture and radial scanlines from the fracture tip **(see Fig. 41)**. **Fig. 40** defines the changes in process zone around the fracture tip. In this figure the fracture termination point is located at 90 on the Y-axis (asterisk). This is where the perpendicular scanlines stop, and radial scanlines start **(see Fig. 41).** The y-axis represents the angle around the fracture tip (0-90˚) and above 90 becomes the distance behind the fracture tip (200-5000 µm), while the x-axis shows distance perpendicular from primary fracture. **Fig. 41** illustrates the process zone with real data to help interpret **Fig. 40**. The blue and green annotations represent the process zone in two different fracture stages. The blue color defines the elastic process zone and the green color defines the plastic process zone. The black arrows protruding from the center of the primary fracture in **Fig. 41** represent the perpendicular scanlines and the photograph in the bottom right corner is a picture of the sample analyzed. The process zone length when measured in the optical image is equal to the process zone length when measured in the SEM image, although fluctuations cannot be seen in optical view. These figures explain the energy patterns associated with fracture propagation by showing fluctuation in the process zone lengths.

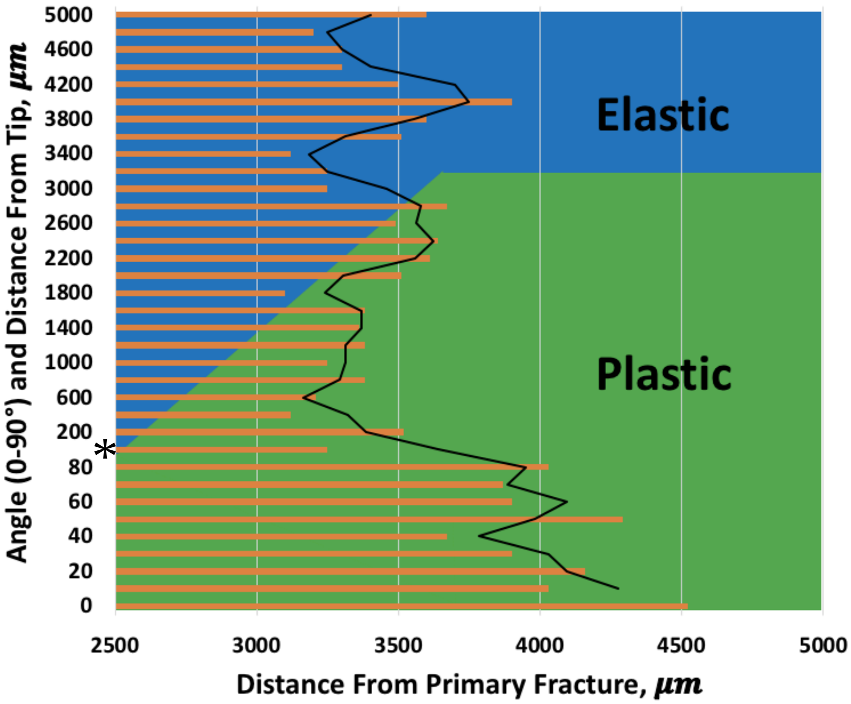

Figure 40: The distance secondary fractures extend into the formation (orange bars) with respect to the distance and angle from the fracture termination point (90º on y-axis). At the primary fracture's end, a radial scanline method was implemented every 10º until parallel with the primary fracture (See Fig. 41). The blue and green colors represent the elastic and plastic zones. 0-90 on the y-axis represents the scanline angles and 200-5000 µm represents the distance behind the fracture tip (perpendicular scanlines every 200 µm). Please see Fig. 41 for visual representation. The black trendline outlines the energy pulsation pattern during fracture propagation.

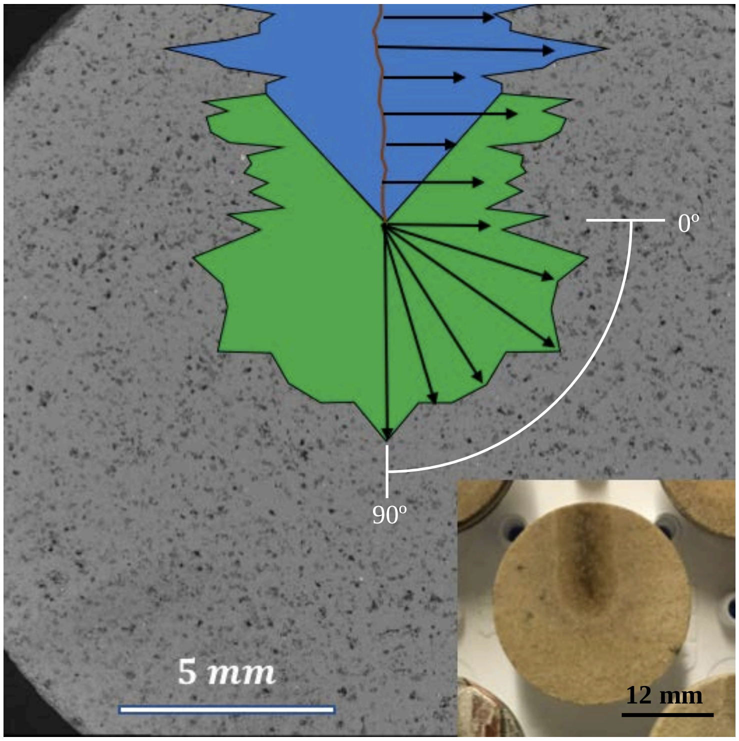

Figure 41: Sketch of the process zone over laid onto an SEM image. The photograph in the bottom right corner is the sample being observed. The blue color represents the elastic zone and the green color represents the plastic zone. The black arrows represent perpendicular scanlines to determine the process zone length. The process zone length in the optical image is equivalent to the process zone lengths in the SEM image.

It can clearly be seen that the process zone appears to be modulated in both the elastic and plastic regions. As suggested previously, this is most likely due to the energy pulsation during fracture propagation. It should be noted that the transition into the plastic zone does not seem to affect this pattern. A second aspect to notice is the increase in process zone within the plastic region, especially from 0-90˚; this suggests a change in physics when the fracture terminates. This can be seen through the change in fracture geometry. Because the fracture tip is always present during propagation, one would expect the process zone to be fairly uniform throughout the length of the fracture and even at the end of the fracture. This is apparently not the case. The point of termination brings an expansion of the secondary fracture network. This is particularly interesting because the stored energy is depleted and yet the secondary fractures extend into the formation further than ever. The change in fracture network at the point of fracture termination suggests that the mechanisms of deformation may be speed dependent. In addition, the secondary fracture width is observed to decrease by approximately 60% in the plastic zone, creating thinner fractures instead of wider fractures.

One hypothesis for why the process zone is increasing at the fracture's termination point is because the secondary fractures are changing from intragranular fractures to intergranular fractures. When the primary fracture is close to the injection point, energy is high, permitting secondary intragranular fractures. The result of intragranular fractures is a significant loss of energy and a reduction of secondary fracture penetration length. However, when the primary fracture terminates, and fracture energy is low, secondary fractures no longer have the required energy to propagate through grains but rather navigate around grains. This process allows the secondary fractures to conserve energy and extend further into the formation.

4.2.2 Secondary Fracture Orientation (azimuth)

Fig. 42 illustrates the frequency of the secondary fracture orientation in the elastic and plastic zones. It is clearly seen that the secondary fracture orientation is not different in the plastic zone and maintains a dominant orientation of 90° from the primary fracture.

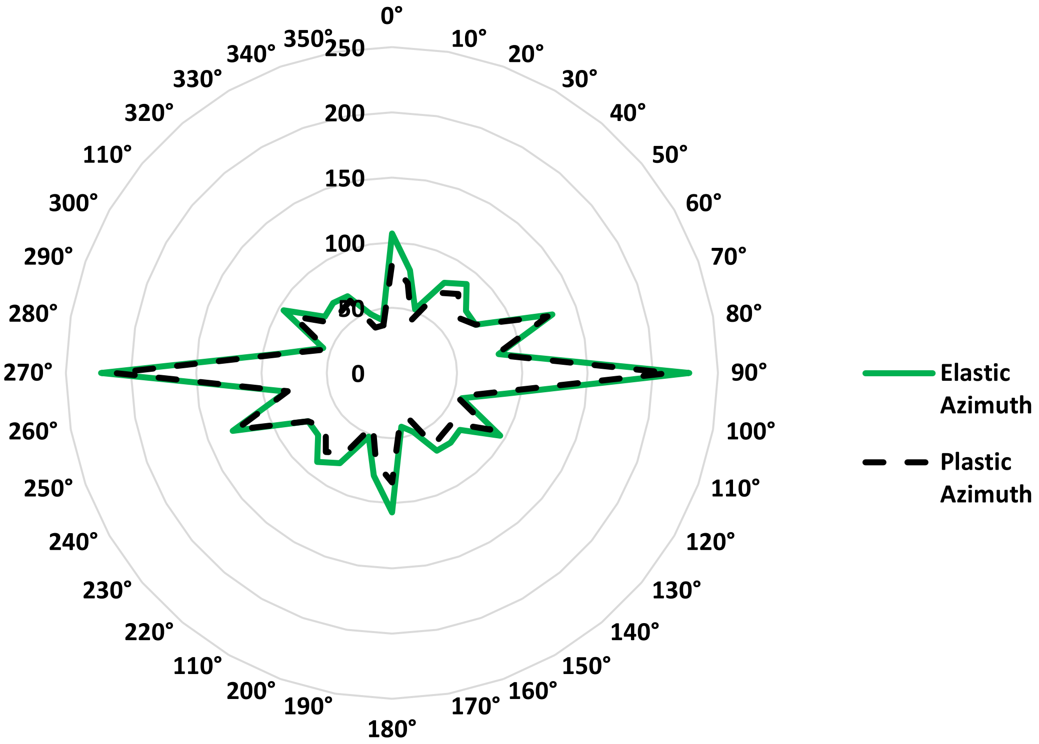

Figure 42: Secondary fracture orientations for the elastic and plastic zones. Both zones correlate with a trend of 90˚. 180°- 360° is a mirror of 0°- 180°.

4.2.3 Density

Fracture density is expressed as the total number of fractures over a given scanline length. **Fig. 43** illustrates a 3D model built in Petrel™ revealing the fracture density counted along 5 mm scanlines with respect to the primary fracture. **Fig. 43** illustrates only the data collected from the parallel scanlines. The center of the 3D model is the primary fracture and always has the greatest density of secondary fractures. The front of the model is labeled “termination point” and is the point at which the fracture ends. Therefore **Fig. 43** and **Fig. 44** represent the tip of the fracture and behind it.

Fig. 43 shows that fracture density decreases with distance perpendicular to the primary fracture and reveals a symmetry on both sides of the fracture. This data correlates with **Damani (2013)** acoustic emission locations. The model also shows a pulsation effect during secondary fracture propagation. Starting at the primary fracture and moving away, it is clearly seen that there is a symmetrical ripple effect in the fracture density model. This illustrates that the secondary fractures propagate episodically like the primary fracture, responding to pressure build-up and release.

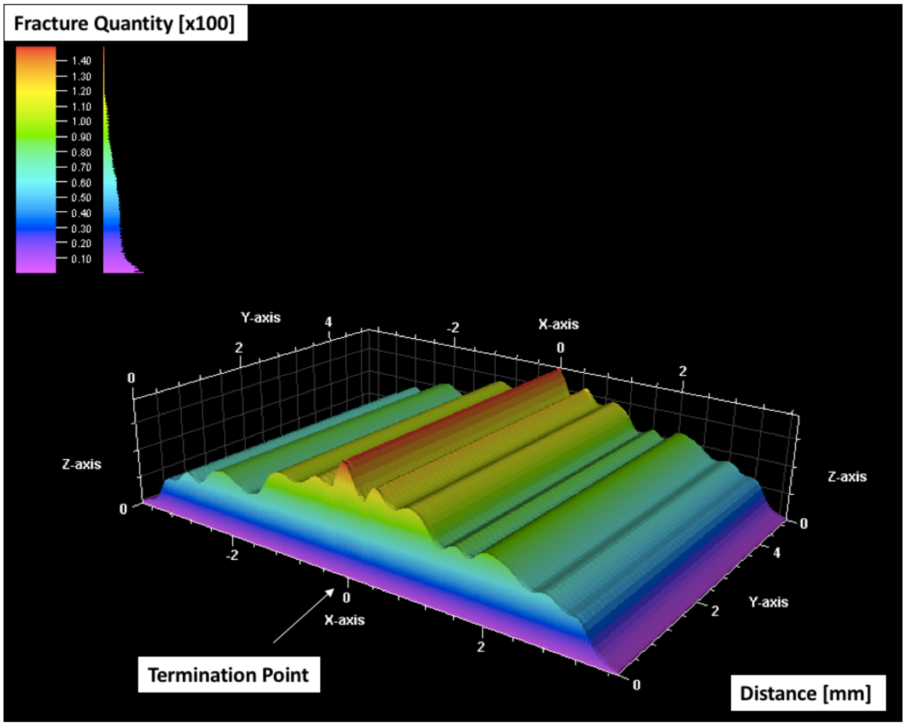

Figure 43: A 3D model illustrating the fracture density with respect to distance from primary fracture. Data shown were collected using parallel scanlines only. Each scanline is 5 mm and represents uniform distribution. The figure shows a repetitive increase and decrease in fracture density as it continuously decreases with distance from the primary fracture.

Fig. 44 is similar to **Fig. 43** only now we show the perpendicular scanline data instead of the parallel scanline data. In doing so, one can see different features of the zones. Notice that the model has been rotated 90˚ so that the termination point is now facing west. This allows the edge of the model to be seen, which illustrates the increase in fracture density as it nears the termination point. In addition, this model shows where the plastic zone originates. Around 3.2 mm from the termination point there is a noticeable increase in the number of counted fractures. We observed that the plastic zone has a greater number of fractures than the elastic zone; thus, the abrupt increase in fractures confirms where the elastic zone stops and transitions into the plastic zone.

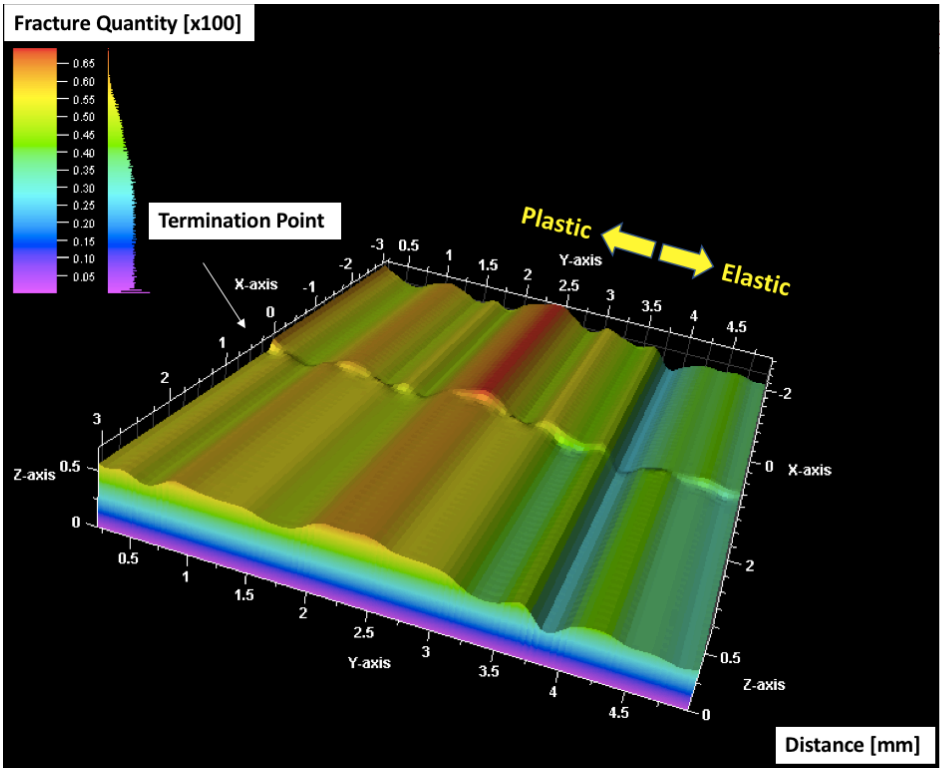

Figure 44: A 3D model illustrating fracture density with respect to distance from the termination zone. Data shown was collected using perpendicular scanlines only. Each scanline is the length of the process zone and represents all intercepted secondary fractures from the primary fracture to the end of stimulation.

The 3D model does not illustrate the decrease in fracture density very well. A graph of the same data is provided in **Fig. 45**. This shows the point at which the secondary fracture network begins to feel the effects of the plastic zone based on the increase in counted fractures.

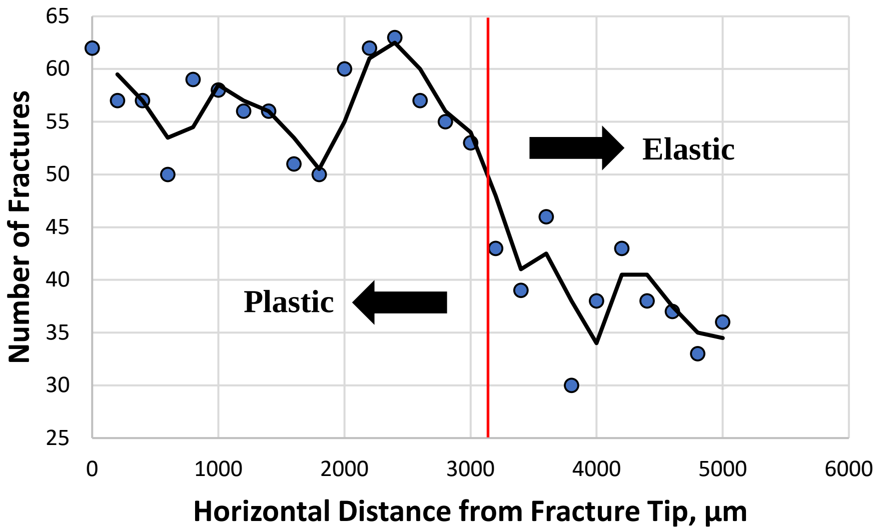

Figure 45: Data from the perpendicular scanlines starting at the fracture's termination point, 0, and moving back 5000 µm. A substantial decrease in the fractures can be seen around 3200 µm, illustrating the point at which the plastic zone influences decreased.

4.2.4 Primary Fracture Width

Capturing an accurate representation of the fracture network was one of the primary goals for using a low viscosity epoxy as our hydraulic fluid. **Fig. 46** illustrates the rate of decline for the primary fracture width with distance from the injection point; the fracture width does not decrease in a monotonic linear manner but instead appears to have 3 different zones. Zones 1 and 3 behave similarly, with comparable negative slopes and lengths. Zone 2 however, includes over half of the length of the fracture and shows relatively no decline. This may suggest that the greatest loss of energy occurs at the initiation and termination of the fracture, where the process transitions from intragranular to intergranular failure.

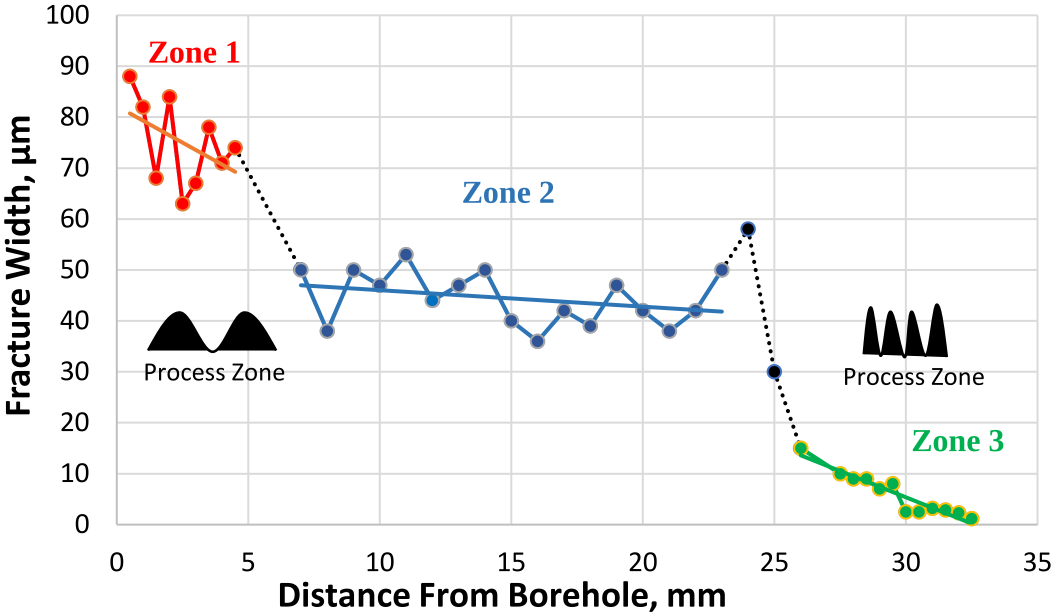

Figure 46: A documentation of the primary fracture width starting at the injection point and ending at the fracture's termination zone. Three distinct zones are observed. Also notice the process zone frequency is lower near fracture origin and higher at termination point.

It is also worth noting that cyclical nature of the process zone is highly dependent on where it is observed along the fracture. For example, if the process zone is analyzed near the injection point, each pulsation is longer in duration, but few occur; i.e., lower frequency. On the other hand, if the process zone is observed near the termination point, the pulsations are much more frequent; i.e., higher frequency. This suggests that the fracture initially propagates with a small number of strong pulsations and finishes with a larger number of weak pulsations.

4.2.5 An Elastic/Plastic Comparison of Fracture Geometries

Table 6 illustrates a statistical comparison of fracture geometries between the elastic and plastic zones. Rows 2 and 4 display a significant decrease in primary and secondary fracture widths within the plastic zone but large variations occur. Rows 3 and 5, however, show that the average and total secondary fracture length do not change despite the loss of energy. This suggests that it requires more energy to widen a fracture than to extend a fracture. Row 7 illustrates that the number of fractures per scanline increases once the plastic zone is reached but row 8 reveals that the fracture density stays constant. This implies that the increase in the number of fractures is due to the increase in process zone, defined by the length that the secondary fractures extend into the formation (row 9), which increases by nearly 60%.

Table 6: Comparison between the elastic and plastic zone. The elastic zone contains perpendicular scanlines to primary fracture and the plastic zone contains perpendicular and radial scanlines depending whether in front or behind the fracture termination point (see Fig. 41). In the plastic zone, there is a significant decrease in fracture width but increase in process zone length.

Row	Subject	Elastic	Plastic
1	Length Analyzed, µm	4500	4000
2	Average Primary Fracture Width, µm	48 ± 21	7 ± 3
3	Average Secondary Fracture Length, µm	64 ± 39	63 ± 41
4	Average Secondary Fracture Width, µm	1.9 ± 2.4	0.7 ± .5
5	Total Secondary Fracture Length, mm	110	100
6	Most Common Azimuth, degrees	90˚	90˚
7	Density (Number of fractures per scanline)	38 ± 4.5	52 ± 5.2
8	Density (Number of fractures per mm)	15.8 ± 2.2	15.5 + 2.3
9	Process Zone for 1 wing, µm	2152 ± 260	3620 ± 381

4.2.6 Upscaling

The plastic zone was plotted in **Fig. 47** to see how the data compare with previous observations. Looking at the black box on the graph, one can see that the plastic zone lies on the upper limit of the error margin of the upscaling plot. This is reasonable because we previously determined that the process zone increases as it enters the "plastic region", therefore the data will increase on the y-axis; nonetheless, the data still appears to be consistent with the graph for upscaling purposes.

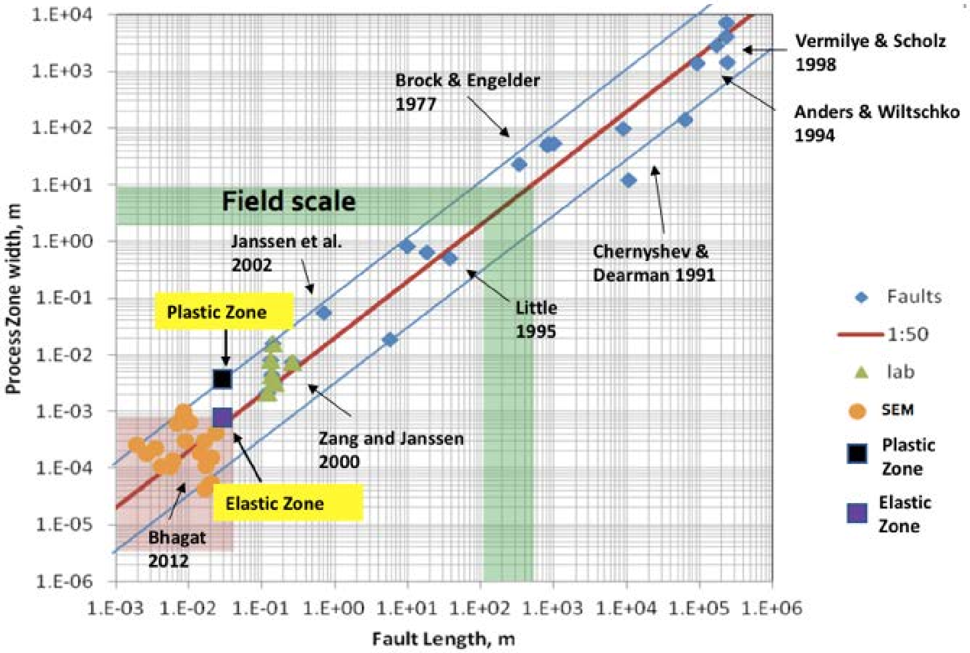

Figure 47: Upscaling procedure for the plastic zone of a triaxial fractured sandstone conducted under a laboratory setting (Zang and Stephansson, 2010).

4.3 Tennessee Sandstone and Quartz Twinning

To determine whether Dauphiné twins are present in the quartz grains, two conditions must be satisfied. Condition 1 states that the z-axes across the boundary of the host and twin are the same, thus ϕ and ϕ_1 are equal $(\pm 3^\circ\ variation)$, and condition 2 states the rotation of the x-axis, defined by ϕ_2, is $60°$ ($\pm\ 3°\ variation$) **(Wenk et al., 2011)**. These experiments were conducted to determine if the above conditions could be identified in quartz grains deformed during hydraulic fracturing. An electron backscatter diffraction (EBSD) detector was used to determine Euler angles. The EBSD detector recognizes pattern formations within a crystal structure. This is made possible by rotating the sample stage within the SEM chamber 70˚ to the electron beam; allowing the EBSD detector to be 90˚ from the sample surface. The electron beam collides with the sample surface to form electron diffraction patterns that are unique to specific crystal orientations. These orientations can be broken down into three Euler angles to determine the presence of mechanical twinning. **Fig. 49** shows the diffraction patterns of a quartz crystal within the area of study. For further explanation on Euler angles, visit section 3.3.6 for twinning procedures.

4.3.1 Native Sample

Three experiments were conducted on a native, undeformed Tennessee sandstone to ensure that the sample did not contain Dauphiné twins prior to hydraulic fracturing. The area of study for one of the three samples is shown in **Fig. 48**, which includes the analysis of approximately 7 quartz grains. Several attempts were made to get a fine surface for optimal analysis but was never perfectly successful. Unwanted topography can be seen that made data collection difficult.

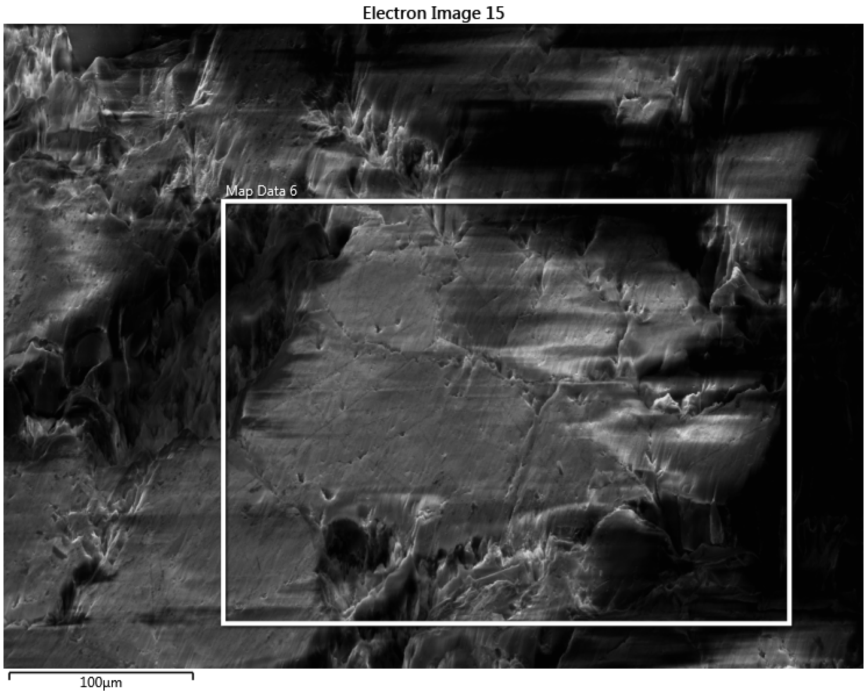

Figure 48: Area of study for a native, undeformed Tennessee sandstone. Approximately 7 grains are being analyzed for this sample.

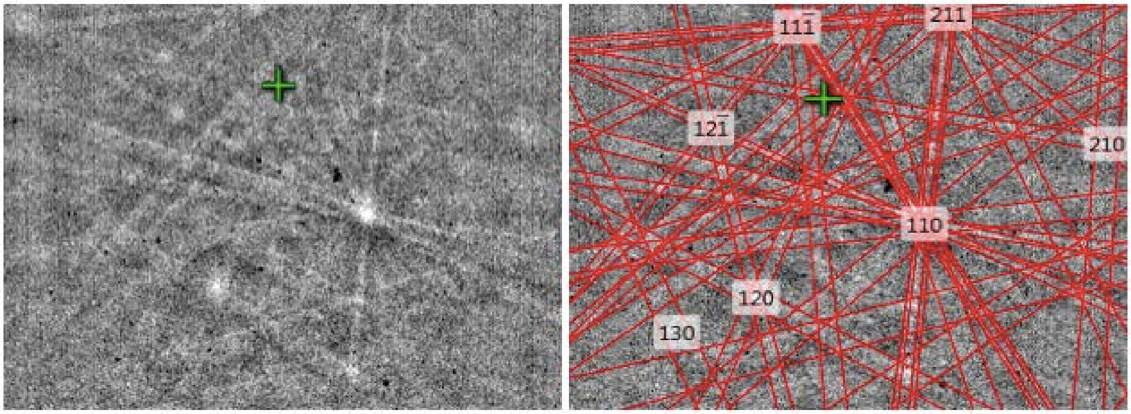

Figure 49: EBSD diffraction pattern of quartz. The individual bands represent spacing of specific lattice planes. The indexing procedure on the right side illustrates the crystal's Miller indices. Diffraction patterns appear weak due to carbon coating the sample to reduce charging.

Fig. 50 shows the correlation between $\emptyset$ and $\emptyset_1$. To satisfy condition 1 for Dauphiné twins, $\emptyset$ and $\emptyset_1$ must be equal. Significant overlap can be seen between the two Euler angles, most dramatically around 90˚. **Fig. 51** illustrates an $\emptyset$ and $\emptyset_1$ map that is over lain onto the SEM area of study. Each colored pixel represents a data point where a diffraction pattern is recognized, and the grey background represents data that could not be analyzed. The EBSD detector only analyzed diffraction patterns for quartz grains. Thus, unrecognizable data could be due to other minerals such as feldspars or clay. The different colors in **Fig. 51** represent different crystal orientations and therefore illustrate the different quartz grains. Despite ion milling, the unwanted topography of the sample added difficulty when recording diffraction patterns and only 32% of Euler data could be collected. The primary color for the correlation between $\emptyset$ and $\emptyset_1$ in **Fig. 50** is light green, indicated by the black arrow. Noticing the same color on the Euler map in **Fig. 51**, the location of the Euler correlations can be found. **Fig. 51** shows that $\emptyset$ and $\emptyset_1$ correlations dominate most of data points, thus proving condition 1 is satisfied.

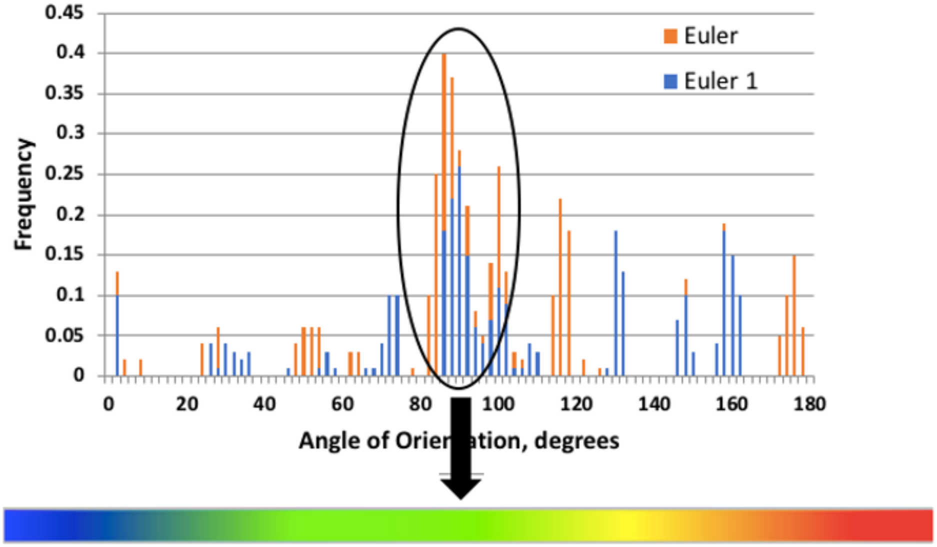

Figure 50: A comparison between $\emptyset$ and $\emptyset_1$. There is a dominate correlation between 80° and 100°. There are also minor correlations around 30° and 150°. The majority of correlations fall within the light green color on the color bar.

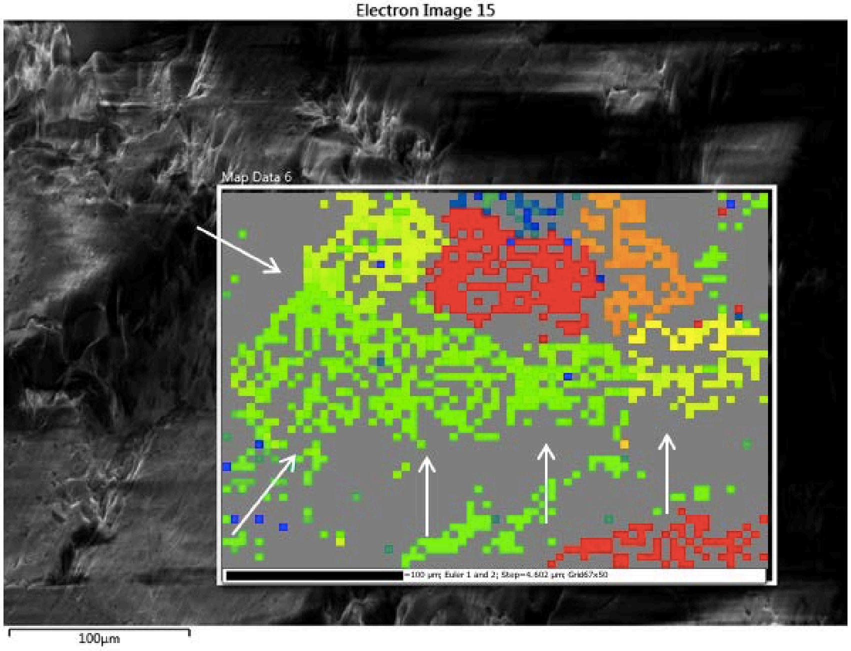

Figure 51: Map of Euler angles displaying $\emptyset$ and $\emptyset_1$. The map is overlain onto the area of study to show the location of Euler correlations. The Euler correlation is indicated by a light green color derived from the color bar in Figure 50. Illustrated by white arrows, most of the data collected are equal

The second condition states $\emptyset_2$ must have a 60° rotation around the x-axis. To determine whether this condition is satisfied, $\emptyset_2$ histograms are analyzed. **Fig. 52** shows 3 separate histograms depicting the $\emptyset_2$ angles of quartz. As seen in the top right corner of each graph, a percentage and type of quartz is labeled by the software. Quartz, quartz low, and quartz high are distinguished by the symmetry of the crystal bonds. The higher the forming temperature, the better the symmetry will be. Quartz high represents high symmetry while quartz low represents low symmetry. Quartz is the symmetry for a normal quartz crystal. If all the percentages are added together, they equal 32.56%, which is nearly all the data that could be collected. For this experiment, the specific type of quartz does not matter. **Fig. 52** clearly shows that there are no 60-degree rotations around the x-axis. Furthermore, **Fig. 53** does not show a light green color on the Euler map. Thus, condition 2 is not satisfied and it is concluded that the native, undeformed Tennessee sandstone sample does not have Dauphiné twins prior to hydraulic fracturing. See **Appendix C** for the data of two additional native Tennessee sandstone samples.

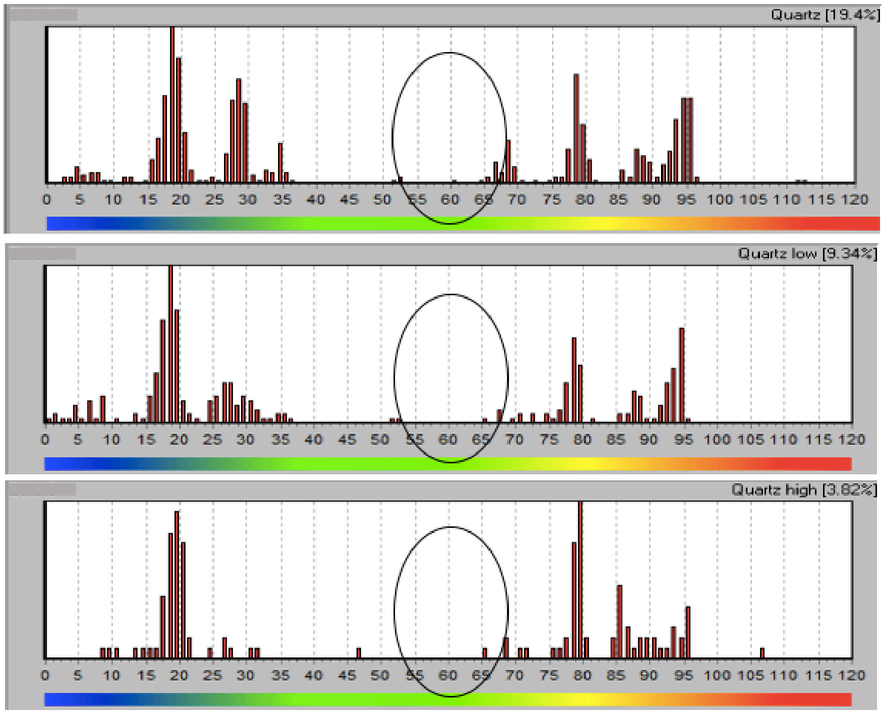

Figure 52: Three histograms showing the $\emptyset_2$ angles for the area of study on the native, undeformed sample. It is clearly seen that there are no, or very few, 60-degree rotations about the x-axis.

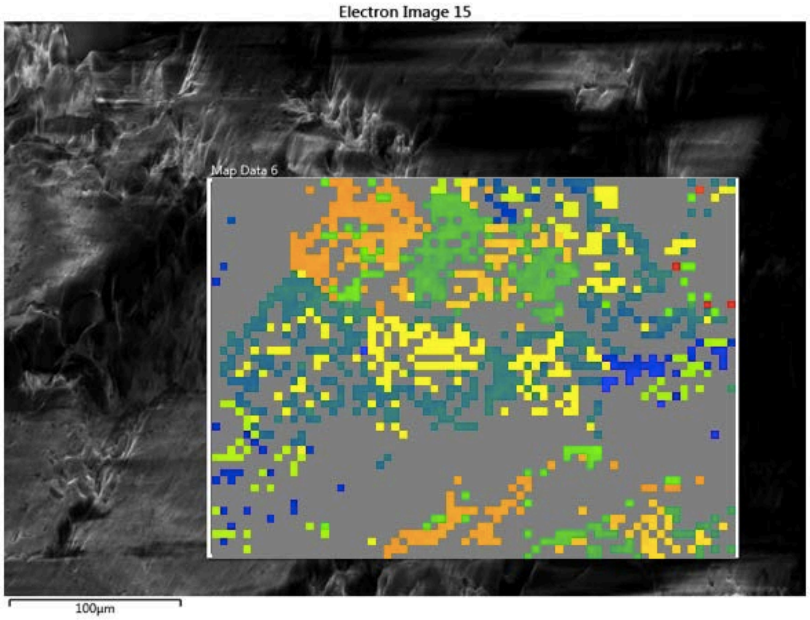

Figure 53: Euler angle ($\emptyset_2$) map over lain onto the SEM area of study. The light green color that represents a 60-degree rotation around the x-axis cannot be seen.

4.3.2 Hydraulically Fractured Sample

The same procedure was applied on a hydraulically fractured Tennessee sandstone to determine whether Dauphiné twins were induced. **Fig. 54** shows the area of study, which is located approximately 10 µm from the primary fracture and is 130 µm wide by 200 µm long. This location was chosen due to the abundance of intragranular fractures and damage among grain boundaries, illustrating a high energy zone and most likely to contain Dauphiné twins. Approximately 8 quartz grains were analyzed in this area of study.

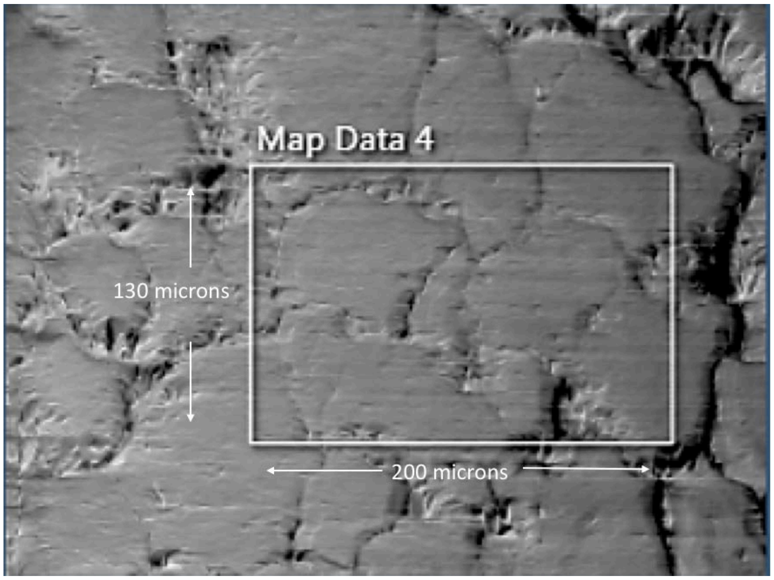

Figure 54: Area of study for the hydraulically fractured Tennessee sandstone. Approximately 8 quartz grains were analyzed in this area of study.

Fig. 55 illustrates the comparison between $\emptyset$ and $\emptyset_1$, which correlate around 10˚, 90˚, and 110˚ with their associated color of blue, light green, and yellow, respectively. Observing **Fig. 56**, $\emptyset$ and $\emptyset_1$ are equal in most of the area of study. Therefore, condition 1 can be satisfied in the designated areas of the Euler map, as marked with white arrows. Notice that over 90% of the diffraction patterns were found during EBSD analysis, which provides a near complete Euler map. The increased quality of the sample surface is due acquiring the image directly over the ion milled surface area. The different grains can be seen by their associated color.

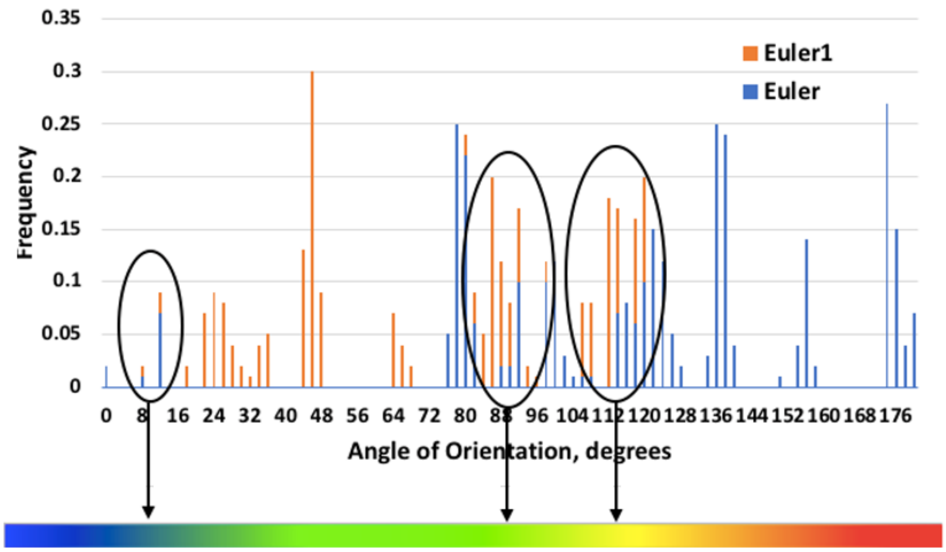

Figure 55: A comparison between $\emptyset$ and $\emptyset_1$ for a hydraulically fractured sample. There is a significant correlation around 10˚, 90˚, and 100˚.

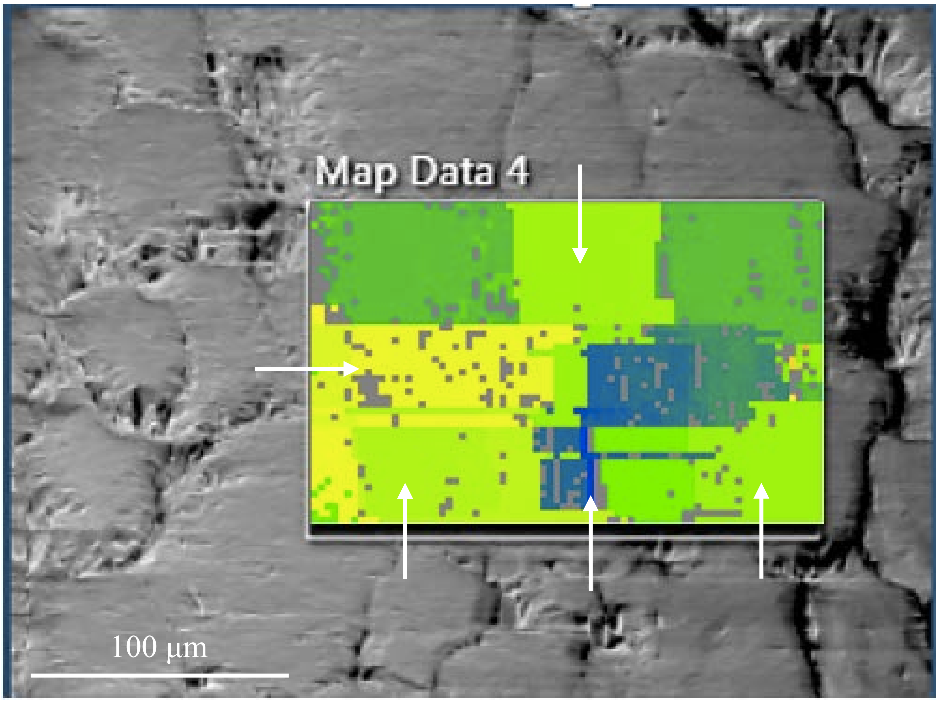

Figure 56: A Euler map displaying $\emptyset$ and $\emptyset_1$. The map is overlain onto the area of study to show the location of Euler correlations. The Euler correlations are shown in blue, light green, and yellow. Illustrated by the white arrows, most of the data collected have equal $\emptyset$ and $\emptyset_1$ angles. Approximately 8 quartz grains were analyzed in this area of study indicated by different colors.

Fig. 57 shows three $\emptyset_2$ histograms illustrating the relative frequency of specific rotations around the x-axis. Prior to fracturing, condition 2 could not be satisfied. However, after fracturing, the frequency of 60˚ rotations around the x-axis increased dramatically. All three types of quartz contain 60˚ rotations and the added percentages equal 84.3%, which is the majority of data. **Fig. 58** displays the $\emptyset_2$ map overlain onto the area of study. This map shows the areas which condition 2 is satisfied by a light green color.

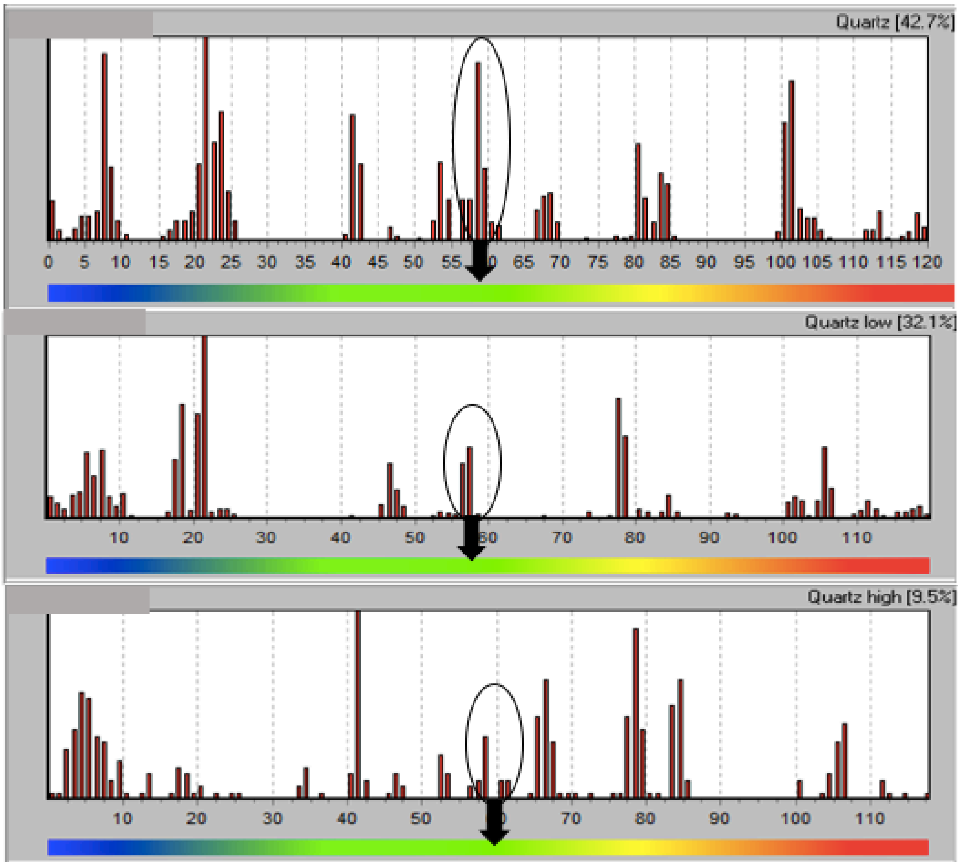

Figure 57: Three histograms showing $\emptyset_2$ angles for the area of study on the fractured sample. 60˚ rotations around the x-axis can be seen in all quartz.

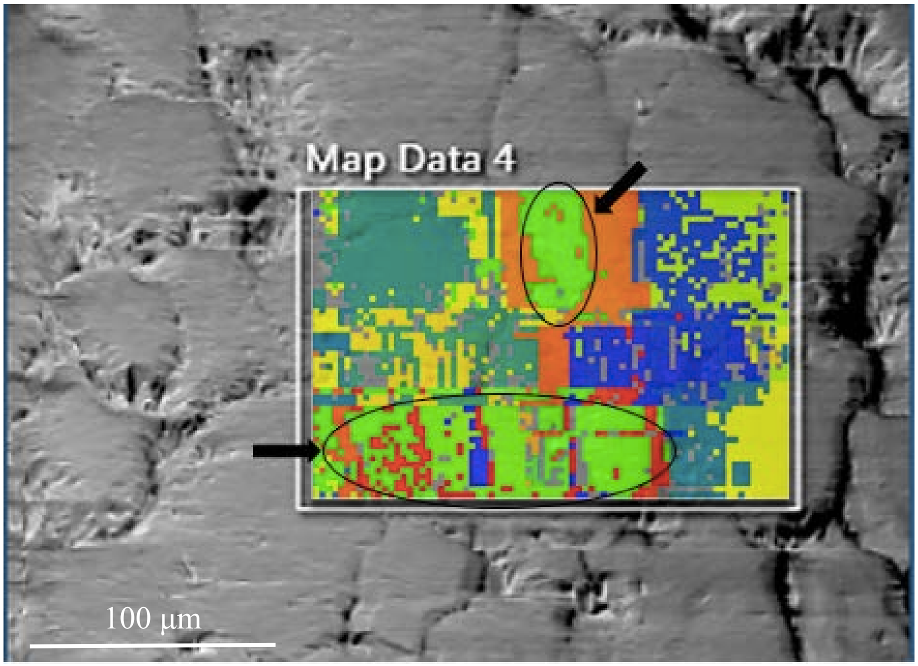

Figure 58: $\emptyset_2$ map overlain onto the SEM area of study. The light green color, which represents a 60˚ rotation around the x-axis, can be seen in two major areas of the map as illustrated by black arrows.

By overlaying the areas where condition 1 and 2 are satisfied, we can determine where Dauphiné twins have formed. **Fig. 59** illustrates these zones with black arrows on the original SEM image. Notice the areas where Dauphiné twins were determined are around grain boundaries, this is the most common area for mechanical twins to form. Because Dauphiné twins cannot be seen directly with an EBSD detector, it is only known that twins have formed in these regions due to satisfying the Dauphiné conditions. To view mechanical twinning in quartz, crystallography software such as BEARTEX is needed.

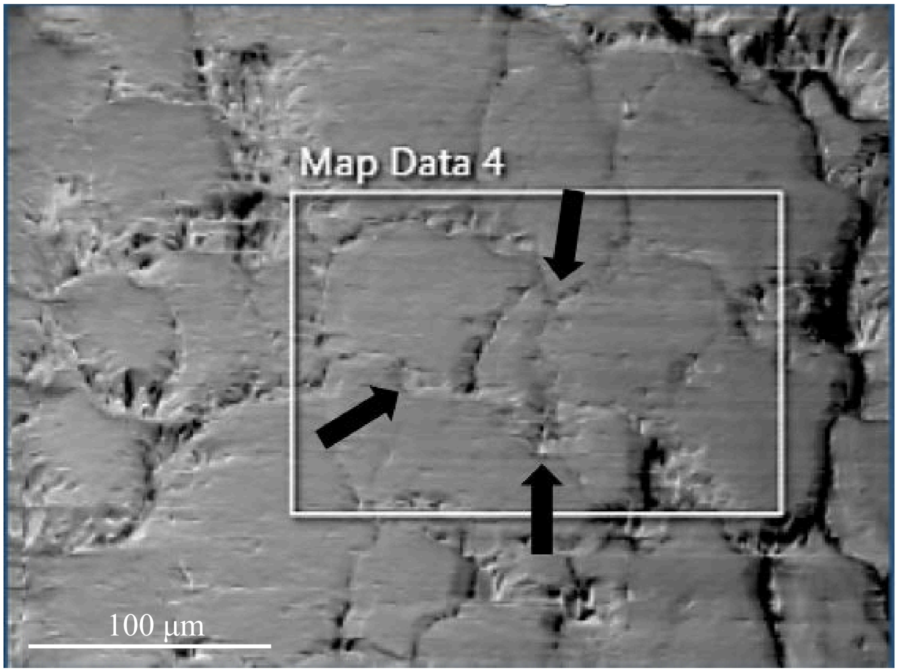

Figure 59: Location of Dauphiné twins illustrated by black arrows. Dauphiné twins cannot be seen with an EBSD detector but the twinning conditions were satisfied in these locations.

The two samples analyzed suggest a distinct change in crystal orientation after the hydraulic fracturing. Before the sample was fractured, few 60˚ rotations about the x-axis could be found. After the hydraulic fracture however, an abundance of 60˚ rotations originated to satisfy the second twinning condition. Additional data must be gathered to draw stronger conclusions, but preliminary observations show a misorientation of grains, which could allow further slip of the propagating fracture to occur, and the creation of mechanical twins that could alter fracture propagation paths and increase SRV. Two additional native samples were analyzed, and a small number of mechanical twins were found, but it is apparent that there is an increase in twinning after hydraulic fracturing. Please see **Appendix C** to view additional crystallography data. Extended studies should be performed to satisfy these observations.

A second fractured sample was analyzed 1.8 mm from the fracture tip to determine if the effects of the plastic zone would alter the creation of Dauphiné twins. The results were very similar to the fractured sample in the elastic zone shown above. Despite the reduction of velocity in the primary fracture, Dauphiné twins were still produced at the fracture's termination point. The data can be found in **Appendix C**.

4.4 Marcellus Shale Fracture Network

The Marcellus shale sample was fractured under uniaxial stress. The stress orientation and magnitude are illustrated by black arrows on the SEM images.

4.4.1 MicroXCT

CT scan was performed at the Integrated Core Characterization Center (IC^3) by **Dr. Mark Curtis** on the 2.5" tall by 1.5" wide uniaxially fractured Marcellus shale sample. **Fig. 61** shows four 2D slices, from top to bottom, in 0.5" increments. See **Fig. 60** for an illustration of where CT scans are located on the sample. **Fig. 61a** shows a fracture breaching the sample's edge with Field's metal inside (seen by high contrast). **Fig. 61b** shows two additional fractures (one parallel to maximum stress and one perpendicular to maximum stress) and illustrate the nonuniform displacement of Field's metal. The propagation of the fracture in direction not parallel to maximum stress is due to an insufficient magnitude of applied load (500 psi). However, prior attempts by the author have shown that a greater amount of applied load causes the shale to fail before injection. **Fig. 61c** shows the initiation of fracture propagation in the direction of maximum stress and **Fig. 61d** illustrates the Field's metal filling the area around the wellbore before fracture initiation.

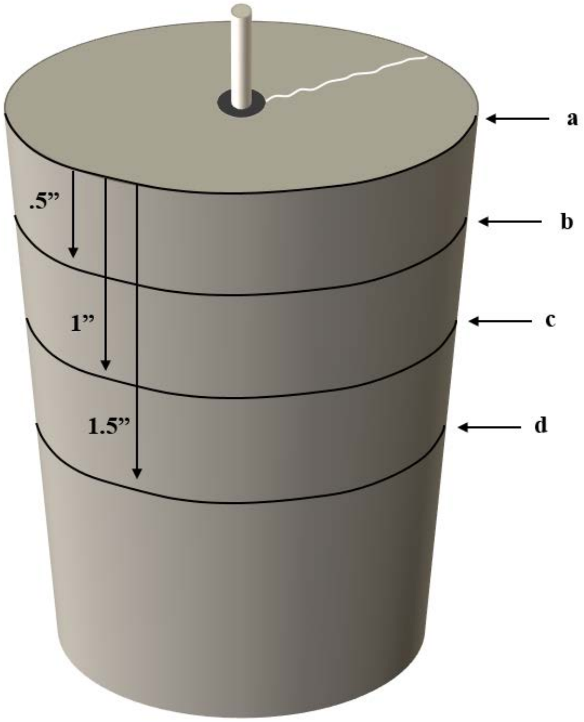

Figure 60: A schematic showing the locations of the 4 CT scans displayed in Figure 61.

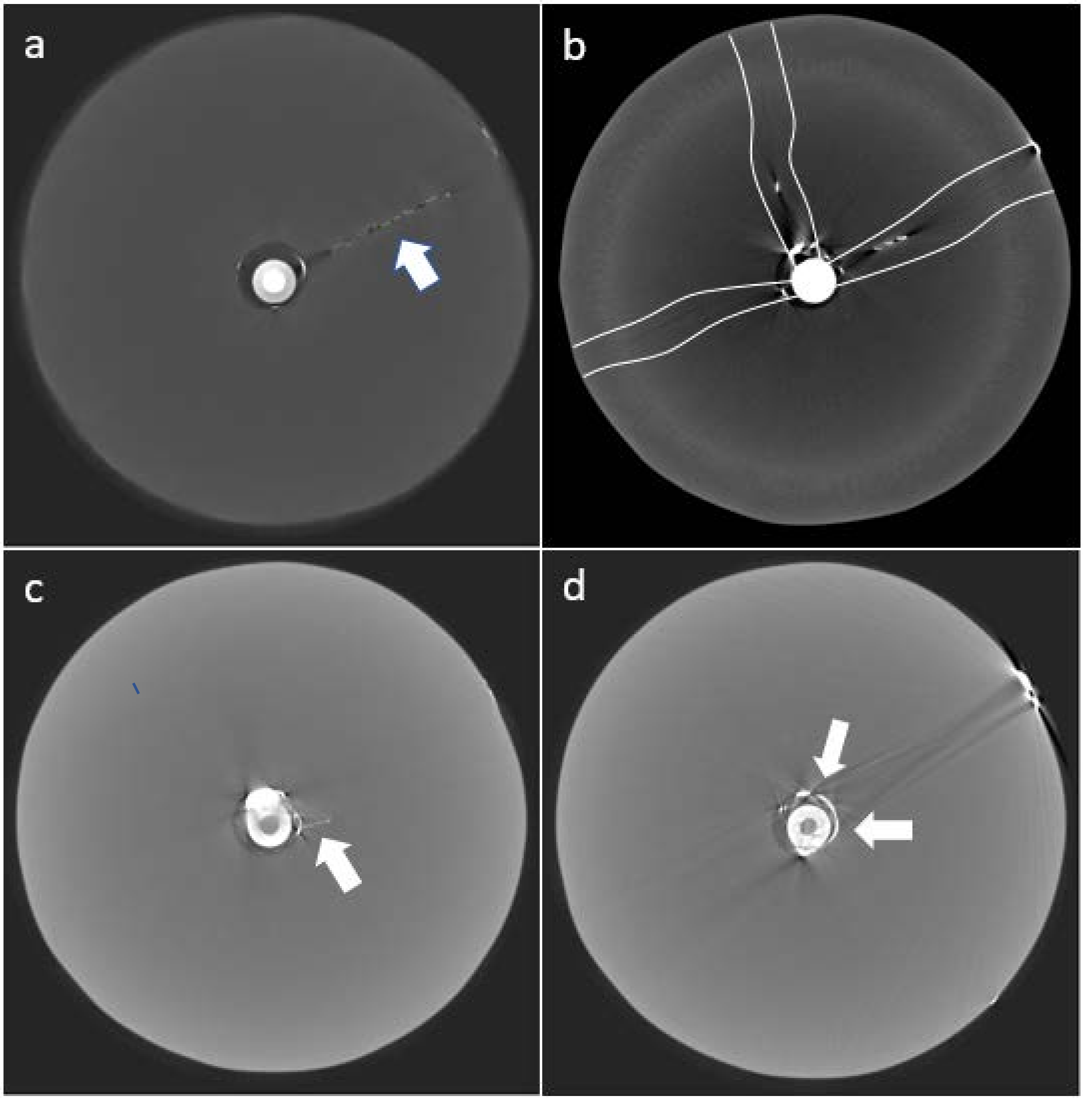

Figure 61: Four 2-Dimensional CT scans illustrating the top (a) to bottom (d) of the 1.5” diameter core in 0.5” increments. Field’s metal can be seen by the bright contrast and is signified by white arrows. The three fractures in image “b” are outlined by white lines for clarity.

Fig. 62 and **63** display the scans stacked together to form a 3-D model. **Fig. 62** shows that a minimal amount of Field’s metal penetrated the sample. A fracture can be seen along the outside of **Fig. 62a** and Field’s metal is clearly seen down the outside surface of the sample. **Fig. 63** shows the Field’s metal within one of the primary fractures.

Once again, the Field’s metal injection is incomplete and does not uniformly fill the fracture networks.

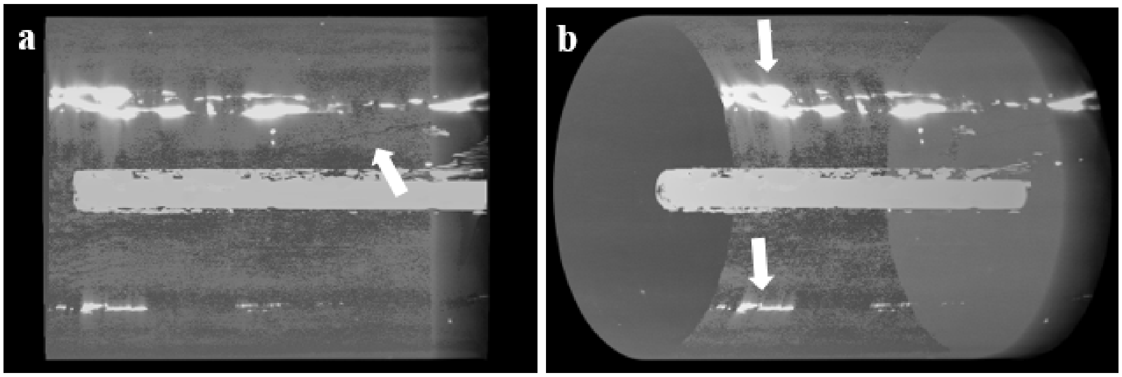

Figure 62: 3-D models of 1,014 CT scans. A) Primary fracture breaking the samples surface. B) Field’s metal on the outside of the sample from fluid filled fractures penetrating the sample walls.

The inconsistency of Field’s metal throughout the primary fracture reveals the irregularity of the primary fracture. Notice the Field’s metal within the primary fracture in **Fig. 63** (illustrated by white arrows). The metal is unevenly distributed and only resides in a small portion of the fracture. The reason for this irregularity is consistent with why the rock does not split into two separate pieces after the fracturing; because the rock is still intact in many places. This could be due the creation of several microfractures during propagation (instead of one primary fracture), initiating and terminating several times in different parts of the rock. As the fracture propagates, stress is building nonuniformly throughout the anisotropic formation causing the fracture direction to deviate. This process may occur several times creating an irregular fracture pattern and making it difficult for the Field’s metal to uniformly fill the fracture. During this process, the individual microfractures will follow the least resistance and connect back together, giving a result of one macrofracture that we observe in SEM. This observation is also documented by **Engelder (1987)** who states supplementary stress will add microfractures until they start to link together. This process occurs because the largest stress risers are at the tip of the longest fractures, causing an increase in stress intensity (K) for every additional linked fracture. Microfracture linking is further explained in **Scholz (1968b)** and **Byerlee (1978).** This hypothesis also defines a great problem for proppant distribution; similar to how the metal cannot flow throughout the "primary fracture", the proppant will not be distributed uniformly either.

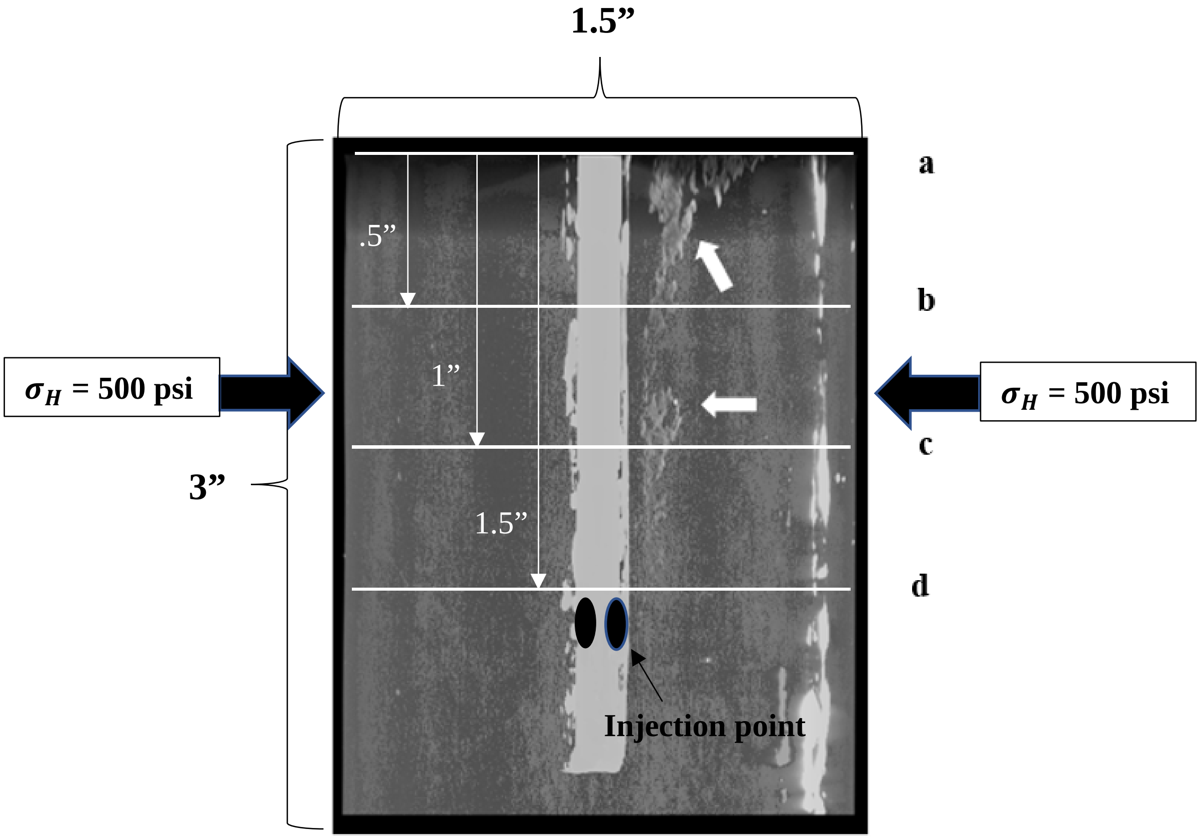

Figure 63: A stack of CT scans showing the Field's metal within one of the primary fractures. Notice the metal is irregular and does not uniformly fill the fracture.

4.4.2 SEM Fracture Analysis

CT analysis helps identify the location of microfractures prior to drilling plugs for SEM. **Fig. 65** is an SEM mosaic of 3,000 images that shows the primary fracture 5 mm away from the injection point. In correlation with CT scans, the distribution of Field's metal is not uniform, indicating a lack of pressure communication. It is possible that the parts of the fracture that do not contain Field’s metal in **Fig. 65** are linking fractures that were created after the Field’s metal had already found its way through the sample, possibly from a continuation of the original fracture above or below the 2-D image. It is also possible that the Fields metal fell out of the sample during sample preparation.

Fig. 64 illustrates the orientation of the SEM mosaic images. All SEM samples were cut across the primary fracture (shown by black lines on the plug). This indicates that all SEM images are being analyzed along the vertical plane of the fracture and have a top (the point closest to the top of the core) and bottom (the point closest to the bottom of the core). A black box is overlain in **Fig. 64** onto the outside of the plug; this shows the orientation the images were taken in accordance to fracture orientation. This sample orientation will now be called vertical sample. The Marcellus shale core was drilled horizontally, making the bedding planes run vertical to the core. It is possible that the primary fracture is propagating along a bedding plane.

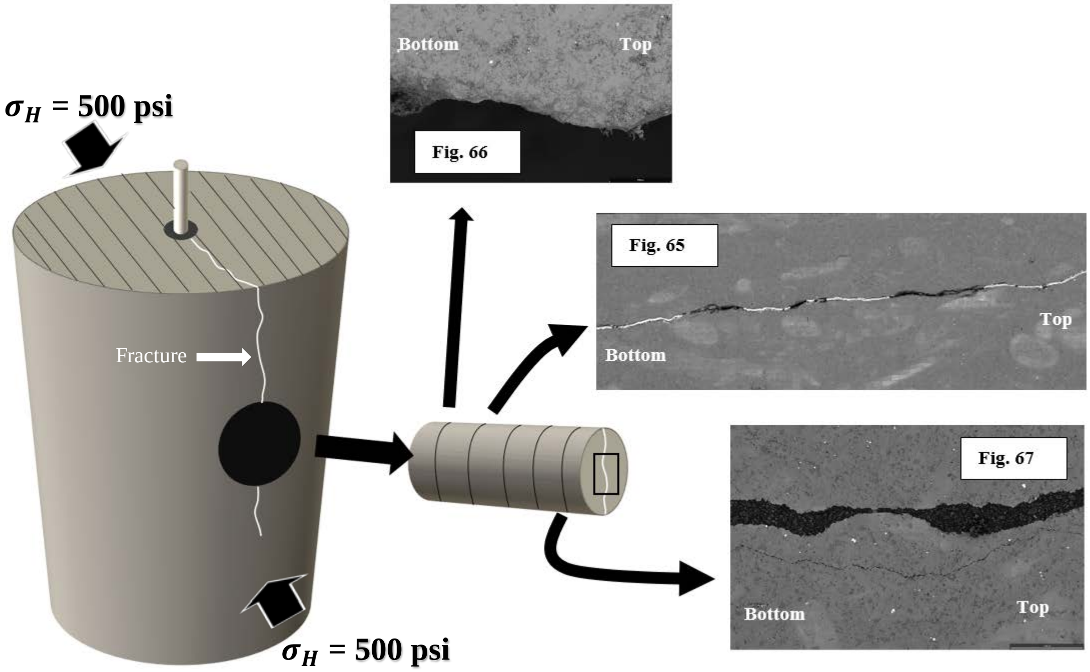

Figure 64: A schematic of the orientation of SEM mosaic images for Marcellus shale. All SEM samples were cut perpendicular the primary fracture as indicated by the black lines on the plug. Each mosaic was taken in the orientation signified by the black box on the front of the plug. The black parallel lines on top of the core indicate the bedding orientation. This core was drilled horizontally and therefore the bedding planes are running vertically through the core. The uniaxial stress was applied parallel to bedding planes (500 psi), causing the fracture to propagate in the direction of planes.

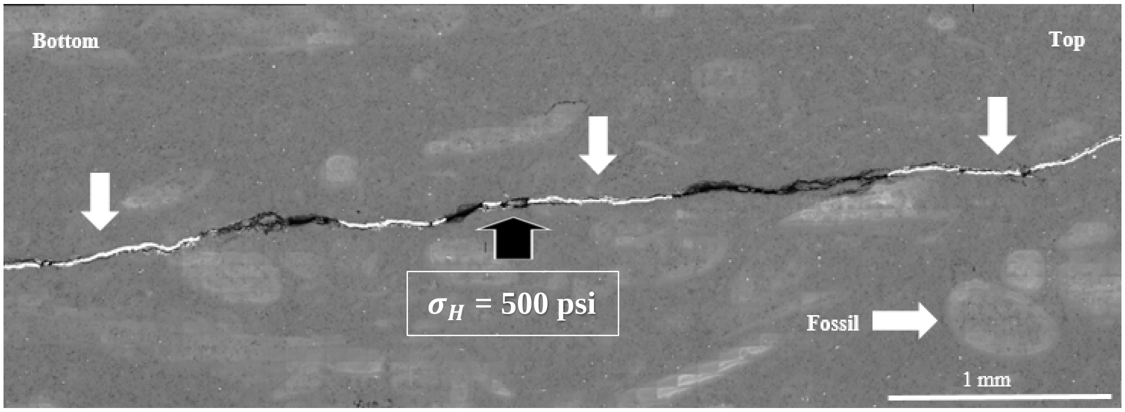

Figure 65: SEM mosaic of 3,000 images. The high amounts of charging within the formation (seen by high contrast areas) are due to fossils within the Marcellus shale. The Field’s metal, illustrated by white arrows, can be seen by the very high contrast within the fracture. Black arrow represents the stress orientation and magnitude of the uniaxial experiment.

Fig. 66, 67, and **68** show the three different extremes of fracture density along the primary fracture. **Fig. 66** is one side of the primary fracture and it is clearly seen that there are no secondary fractures; this is regarded as a “simple” fracture. We will define simple as the density of secondary or tertiary fractures branching off another fracture; the lower the fracture density, the simpler the fracture and vice versa, the higher the fracture density around another fracture, the more “complex” the fracture. Nearly 70% of the primary fracture analyzed in shale revealed no secondary fractures.

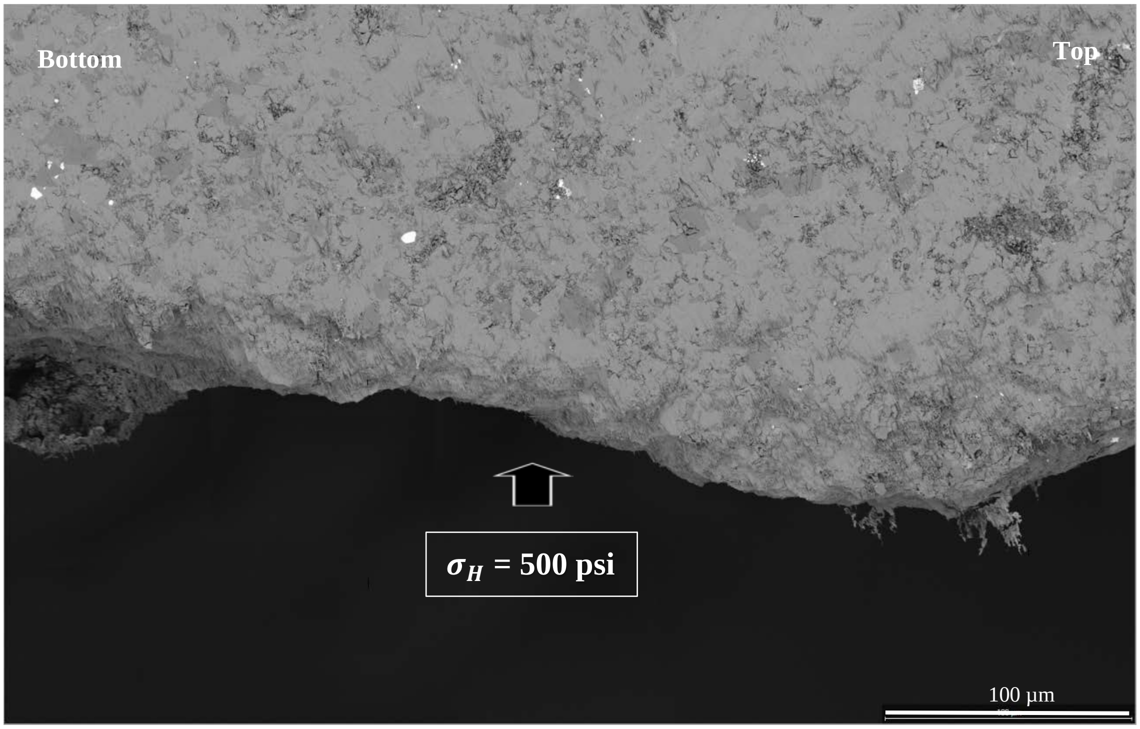

Figure 66: One side of the primary fracture in Marcellus shale, illustrating no secondary fractures entering the formation. This is regarded as a simple fracture. Black arrow represents the stress orientation and magnitude of the uniaxial experiment.

Fig. 67 and **68** shows two sides of the primary fracture that were epoxied together after hydraulic fracturing. This was done to analyze both sides of the fracture simultaneously. A single secondary fracture can be seen in **Fig. 67** propagating parallel to the primary fracture. This fracture is 1.9 mm long and 2.4 µm wide. This is wider and significantly longer than the fractures observed in Tennessee sandstone. **Fig. 68** shows several secondary fractures propagating from the primary fracture in orientations within 30º of the primary fracture and having an average length of 0.3 ± .1 mm and average width of 1.4 ± .5 µm. The reasons that the secondary fractures in Marcellus shale are propagating parallel to the primary fracture instead of perpendicular, as seen in the Tennessee sandstone, are: 1) fractures are following vertical bedding planes, and 2) the rock was fractured under uniaxial load, applying one maximum stress in a horizontal direction.

The secondary fractures in **Fig. 68** appear as hackle marks. In this figure, the fracture is approaching the edge of the sample, which potentially causes changes in stress orientations. These stress variations can create twist hackles that propagate perpendicular to the subsequent tensions. **Engelder (1987)** sees this process on a macro scale when fractures approach the edge of sedimentary beds. At this location, he documents twist hackles forming en echelon fractures within the plane of the primary fracture. **Kulander et al. (1979)** also suggests that twist hackles are most likely to occur in the location of least tensile stress, which also corresponds to the micro scale data shown here.

The observation that secondary fractures in the Marcellus shale are longer than secondary fractures in the Tennessee sandstone is largely due to the grain size of each formation. Secondary fractures in sandstone follow grain boundaries and terminate when a grain causes the fracture to make a strong change in orientation (> 55º) **(Nohava et al., 2002)**. Shale grains, which are primarily silt-clay in size and often form platelet shapes, are not large enough to make an abrupt, terminating impact on secondary fractures, allowing the fracture to propagate further without interruption. **Engelder (1987)** observed longer secondary fractures are associated with straight plume axes. The secondary fractures seen here possess straight and long plume axes rather than curved and short axes, agreeing with **Engelder's** findings.

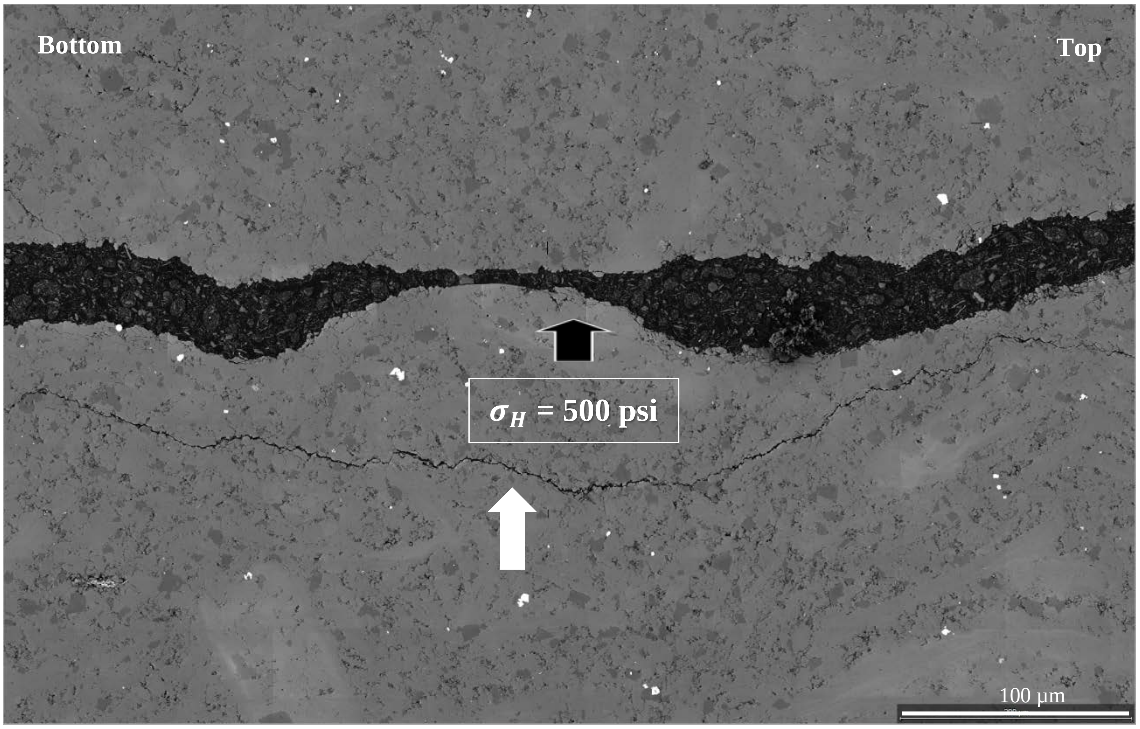

Figure 67: Marcellus shale sample showing a primary fracture with epoxy inside to hold both sides of the fracture together. Because the rock was fractured into two pieces and then epoxied back together, the primary fracture width is not realistic. One secondary fracture parallel to the primary fracture can be seen (white arrow). Black arrow represents the stress orientation and magnitude of the uniaxial experiment.

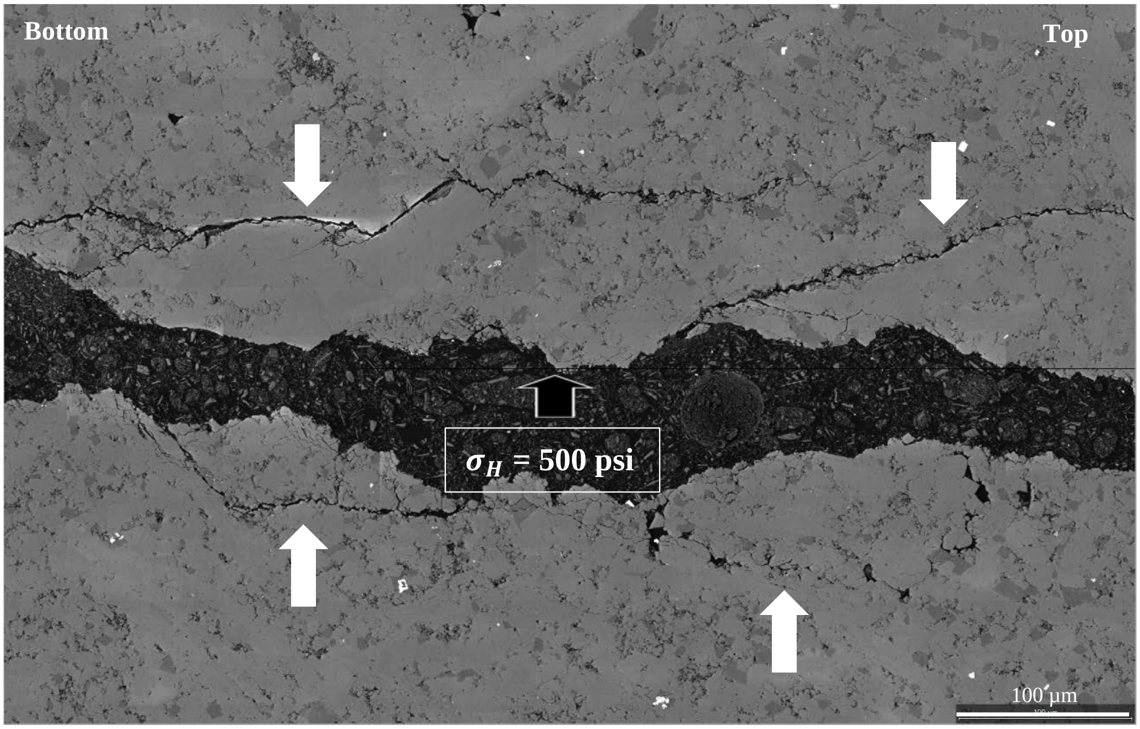

Figure 68: Primary fracture held together with epoxy in the Marcellus shale. Several secondary fractures can be seen (white arrows). Black arrow represents the stress orientation and magnitude of the uniaxial experiment.

The tertiary fractures that branch off the secondary fractures can be seen in **Fig. 69**. In Tennessee sandstone, the tertiary to secondary fracture ratio was 0.26, revealing that secondary fractures were fairly simple. In shale however, the amount of tertiary fracturing exceeds the amount of secondary fracturing by a factor of 100. The average tertiary fracture density around a secondary fracture is 136 ± 20 fractures per mm, whereas the amount of secondary fractures found per mm was less than 1 (30 mm analyzed). The tertiary fractures have an average length of 9 µm, average width of 300 nm and a process zone length of 10 ± 5 µm. More statistics need to be obtained to corroborate these initial results. These numbers are the initial findings and only take into consideration less than 1000 nanofractures.

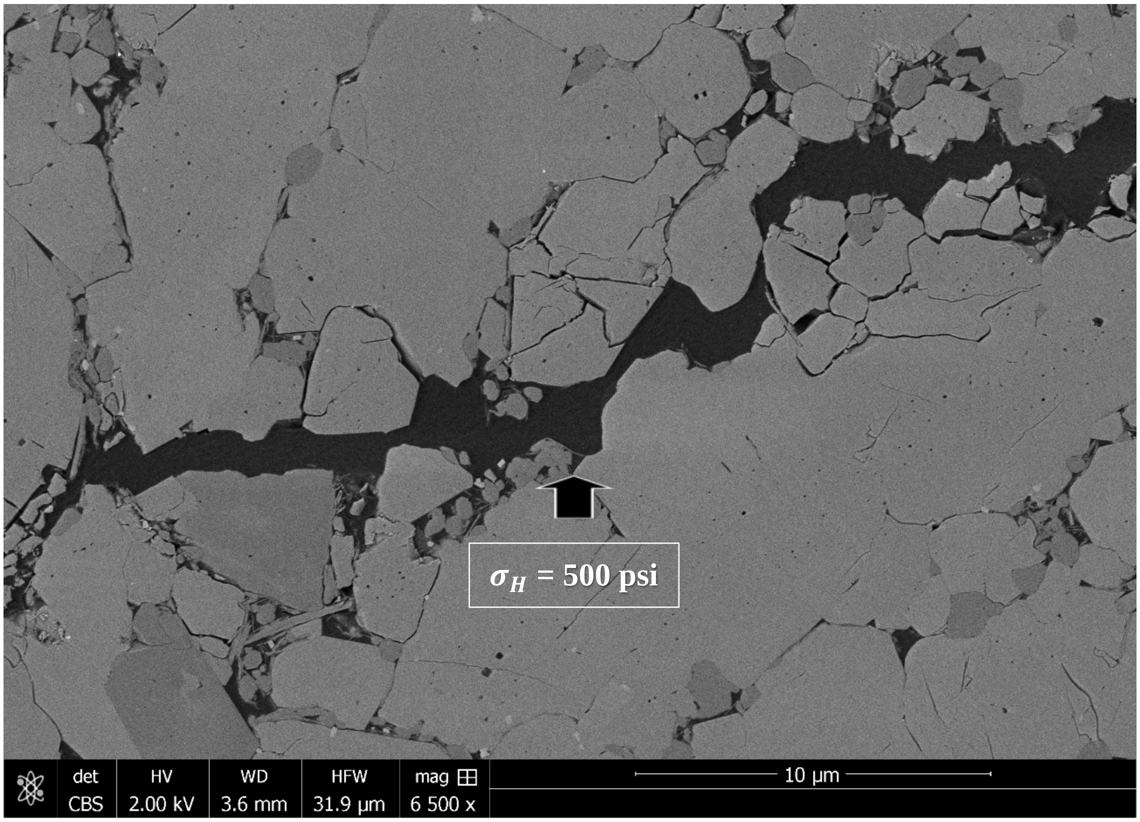

Figure 69: A magnified image of a secondary fracture illustrating the high tertiary fracture density in the Marcellus shale. Black arrow represents the stress orientation and magnitude of the uniaxial experiment.

Fig 70. Illustrates a high nanofracture density around the primary fracture. Technically, these fractures would also be considered secondary fractures since they are initially branching off the primary fracture. However, these fractures are significantly different than the bigger, more obvious, secondary fractures and could be classified as something different, such as the immediate damage zone. For this paper, we will define the damage zone as the immediate area around a fracture that contains nanofractures. This zone is seen to have an average nanofracture density of 169 fractures per 1 mm with a similar process zone length of 10 ± 5 µm. The nanofractures around the primary fracture are very similar to the nanofractures around the secondary fractures, sharing similar lengths, widths, and process zones.

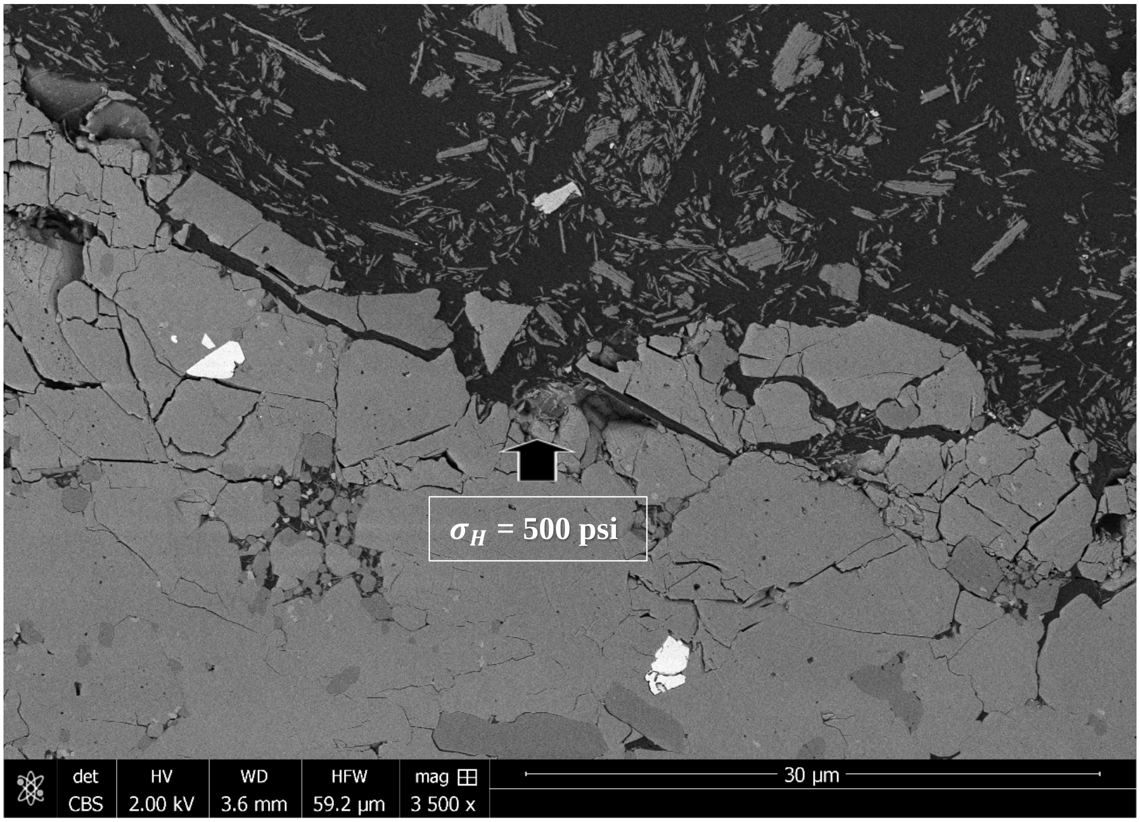

Figure 70: A magnified image of the primary fracture showing a large concentration of nanofractures within 15 µm from the primary fracture. The dark contrast within the primary fracture is epoxy while the lighter contrast within the epoxy are bits of shale. The bright spots within the Marcellus shale formation is pyrite. Black arrow represents the stress orientation and magnitude of the uniaxial experiment.

It should be noted that the production of secondary fractures, tertiary fractures, and nanofractures around the primary fracture only occur in the sample furthest away from the wellbore. This either suggests that the fracture is reacting with the core boundary to create secondary fractures, or that a greater amount of SRV is created when fracture velocity is low. Near the injection point, no secondary or tertiary fractures can be found, forming a simple fracture face. Near the end of the fracture, where velocity is slowing, secondary and tertiary fractures develop.

Energy-dispersive x-ray spectroscopy (EDS) was used to determine the elements within the Marcellus shale. This task was performed to show the amount of Field's metal that intruded into the secondary fracture network after injection. **Fig. 71** shows the abundance of specific elements inside the formation. No indium, bismuth, or tin (which comprises Field's metal) was found in the secondary fracture network and it was concluded that very little Field's metal penetrated into the secondary fractures.

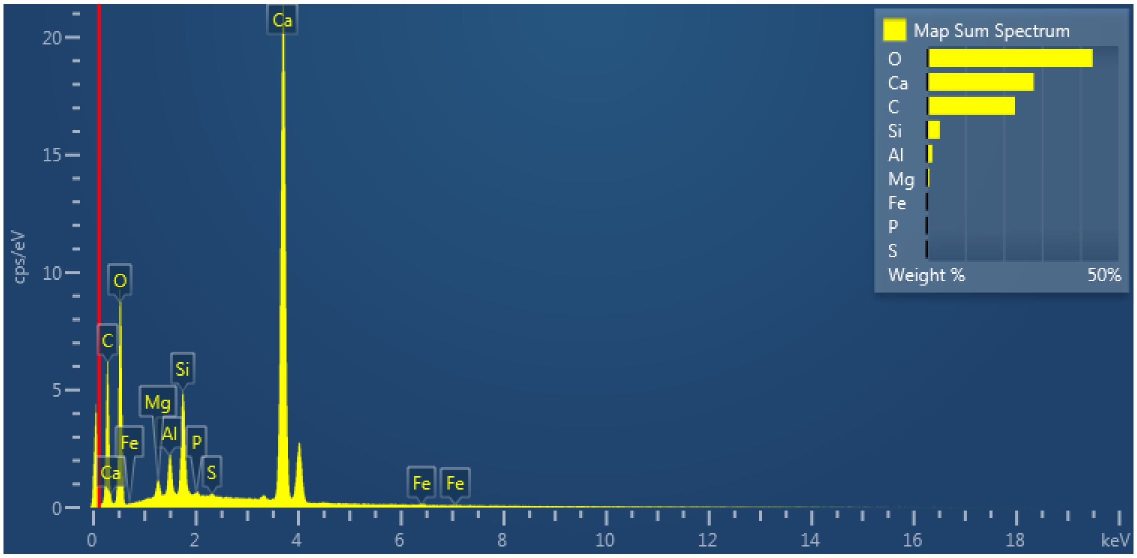

Figure 71: Elemental spectrum of the Marcellus shale. No traces of Field's metal can be found within the secondary fractures.

4.5 Pyrophyllite Fracture Network

The pyrophyllite sample was fractured under uniaxial stress. The stress orientation and magnitude are illustrated by black arrows on the SEM images.

4.5.1 MicroXCT

MicroXCT scans for the pyrophyllite sample were performed by **Dr. Nick Drenzek** of **General Electric Co. (GE) Baker Hughes. Fig. 72** displays the primary fracture and distribution of Field's metal. It is apparent that the primary fracture within the pyrophyllite is larger and more uniform than the fracture within the Marcellus shale.

One reason for this finding is because the core was fractured twice. The initial hydraulic fracture was thought to have not succeeded because no pressure drop was observed during fluid injection. A second fracture attempt produced a large uniform fracture that nearly fractured the core into two separate pieces. It is thought that the rock was already fractured and significantly weakened when the second hydraulic fracture took place, creating a large primary fracture. CT scans show a significant amount of Field's metal was injected into the sample.

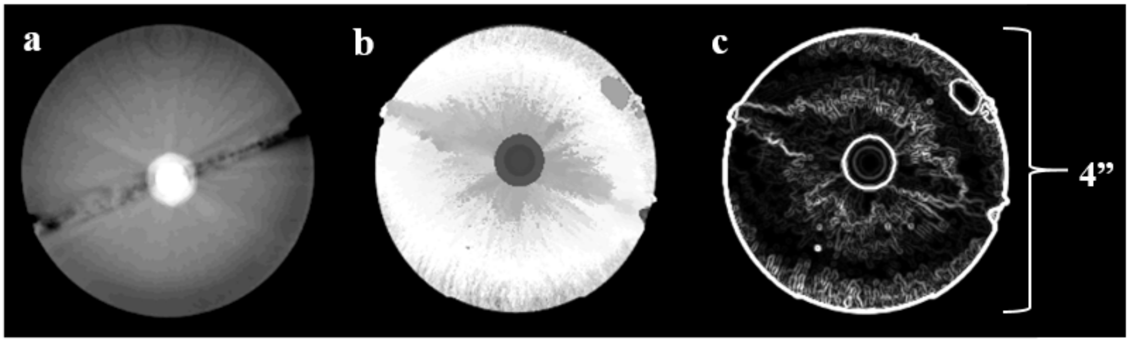

Figure 72: A single CT scan showing the top of the pyrophyllite sample, displaying three different ways to look at the induced, vertical fracture. A) shows a large bi-wing fracture propagating in the direction of maximum stress. B) shows the metal within the primary fracture and how it is distributed. C) shows the edges of the Field's metal, to get a clearer image of the depth of fracture penetration. The bedding planes are oriented parallel to the primary fracture.

Fig. 73 illustrates that the majority of Field's metal is at the bottom of the core. This is due to gravity acting on the metal before it solidified. When the core failed, a wide fracture opened and allowed the metal to flow to the bottom. This is not unlike proppant setting. However, **Fig. 73** shows a large amount of metal being distributed into the sample as well.

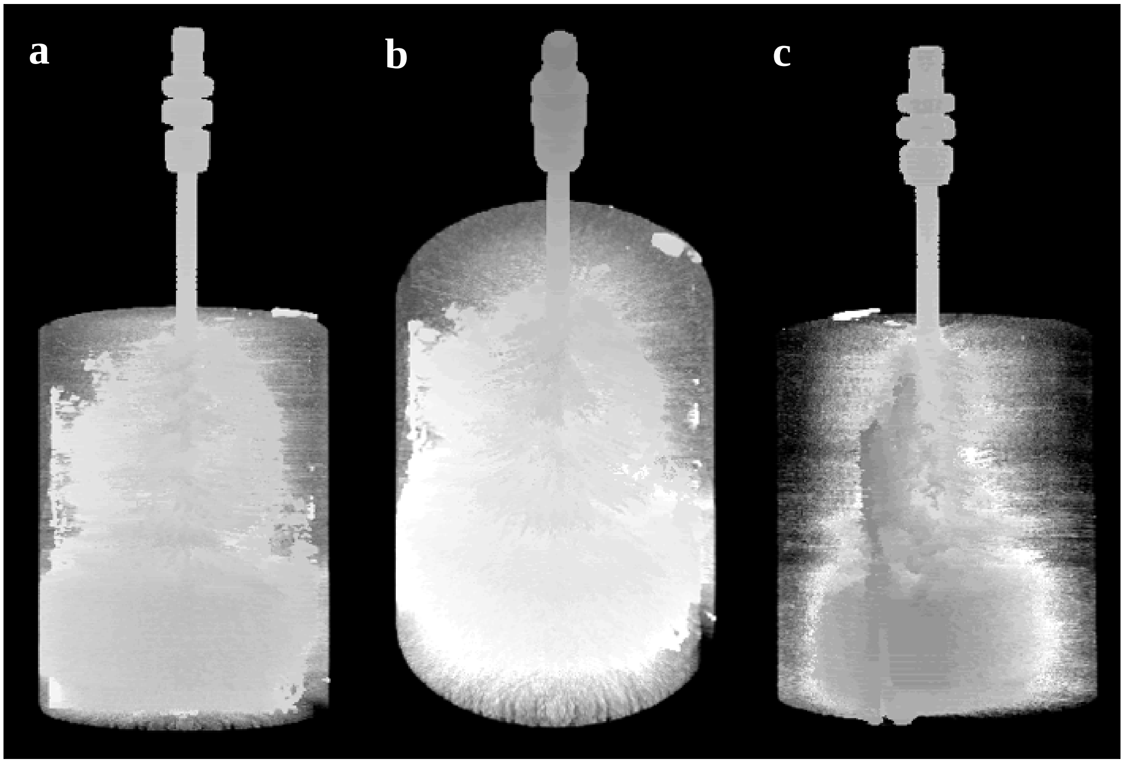

Figure 73: 501 pyrophyllite CT scans stacked together to form a 3-D model. A, B, and C show the same model at three different orientations. The axis of rotation for A, B, and C is the x-axis. A and C are 90º from surface (vertical) and B is rotated 50º from surface. Notice the distribution of metal is much higher than in shale.

4.5.2 SEM Fracture Analysis

The orientation of the SEM mosaics for the pyrophyllite sample is the same as the Marcellus shale. All SEM samples are vertical to fracture. The pyrophyllite core was drilled horizontally and therefore has vertical bedding planes as illustrated by the black lines on top of the core in **Fig. 74**.

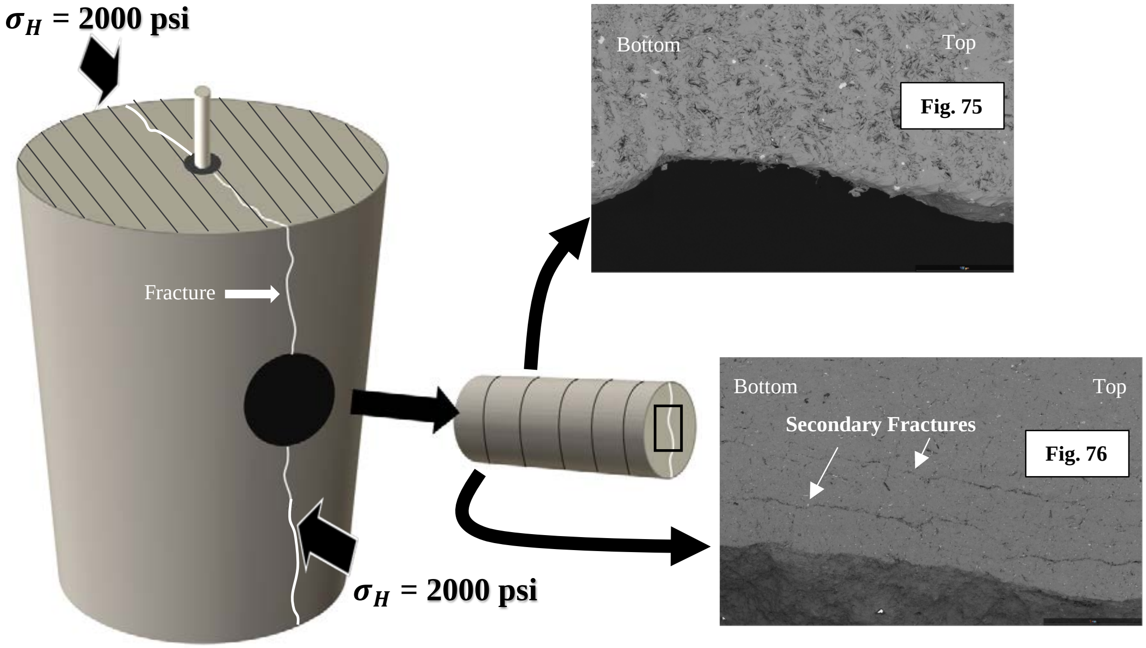

Figure 74: A schematic of the orientation of SEM mosaic images for pyrophyllite. All SEM samples were cut perpendicular to the primary fracture as indicated by the black lines on the plug. Each mosaic was taken in the orientation signified by the black box on the front of the plug. The black parallel lines on top of the core indicate the bedding orientation. This core was drilled horizontally and therefore the bedding planes are running vertically through the core. The uniaxial load was applied parallel to bedding planes.

Fig. 75 shows one side of the primary fracture; there are no secondary or nanofractures along the edge. Unlike the Marcellus shale, a simple fracture face is found throughout the entire length of the fracture. **Fig. 76** illustrates two secondary fractures running parallel to the primary fracture, 1 cm from injection point. These fractures span the length of the 1” sample, so their overall length is greater than 1”. Observing **Fig. 76**, the secondary fracture splits into two separate fractures but link back together within 100 µm. Although the secondary fractures briefly split over the course of 1”, the overall secondary fracture remains uniform, propagating the length of the sample. The secondary fracture closest to the primary fracture is 7.7 ± 4.8 µm wide and the secondary fracture furthest from the primary fracture is 6.3 ± 2.9 µm wide. Therefore, the pyrophyllite shows longer, wider, and fewer fractures than the Marcellus shale, which shows longer, wider, and fewer fractures than the Tennessee sandstone. This illustrates a possible significant difference in fracture morphology based on lithology. Fractures would rather use void space to propagate than extend the preexisting fracture because a lower energy is needed **(Dunn et al., 1973)**, this promotes a large secondary fracture network for high void space rocks such as sandstone. Shales have low void space due to longer sediment transport which produces small (silt-clay), round, and highly sorted grains, allowing for good compaction and the reduction of porosity, permeability, and pore throat sizes. With the addition of their platy crystal habit and strong alignment, fractures would rather extend than branch to start a new fracture because it requires less energy to continue primary fracture propagation.

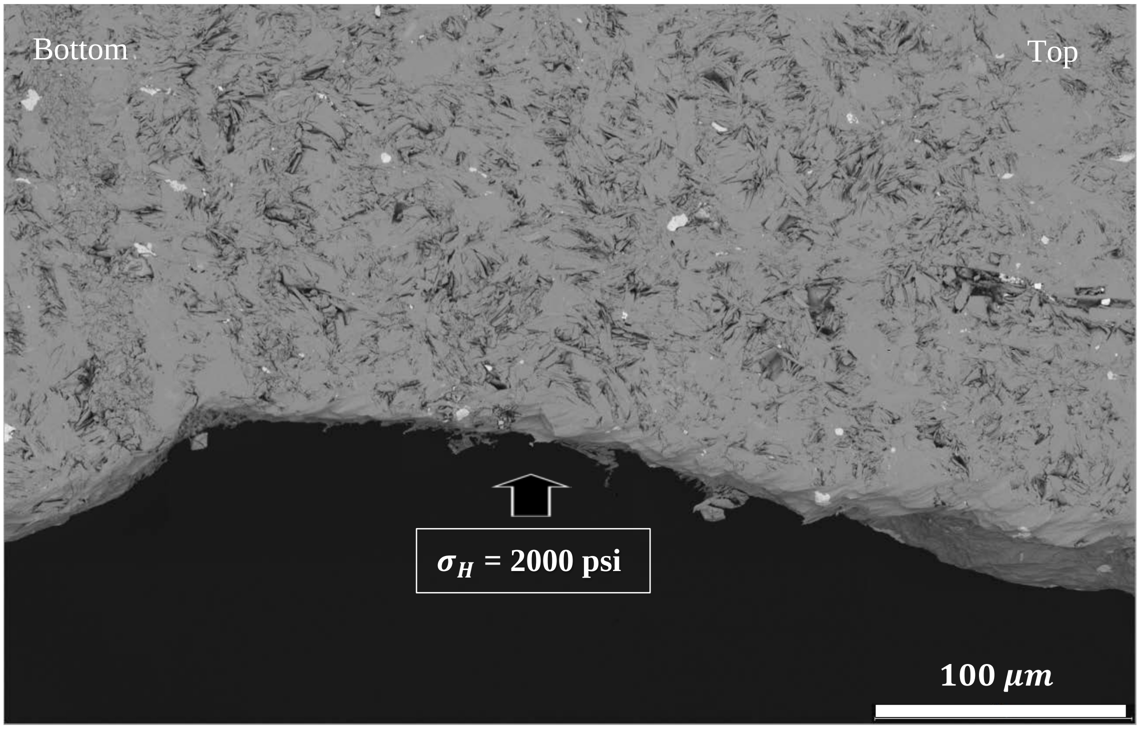

Figure 75: One side of the primary fracture in a pyrophyllite sample. This image is taken about 1 cm from injection point (near wellbore). Black arrow represents the stress orientation and magnitude of the uniaxial experiment.

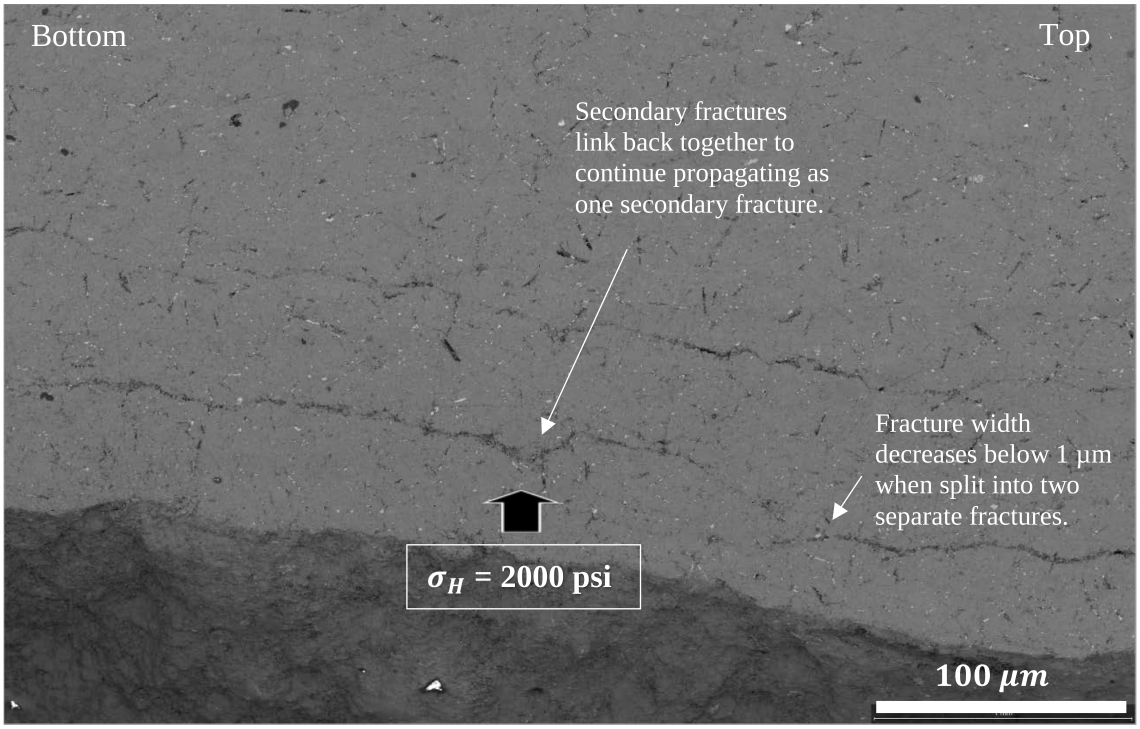

Figure 76: One side of the primary fracture showing secondary fractures running parallel to the primary fracture in pyrophyllite. These fractures are found near the injection point and run parallel to bedding planes. These fractures may be intrinsic and not induced by hydraulic fracturing. A magnified image of these secondary fractures shows no fracture face but only a collection of nanofractures.

Fig. 77 shows the elemental spectrum for the pyrophyllite sample. In similarity to the Marcellus shale, no traces of Field's metal could be found; indicating that Field's metal did not penetrate the formation with the secondary fractures. **Fig. 78** and **79** display 2 of 4 primary fracture surface textures that were analyzed. This analysis was performed to determine whether the fracture surface revealed morphology demonstrating fracture propagation patterns. No unique fracture morphology could be recognized throughout all surface samples. **Raterman et al. (2017)** studied hydraulic fracture surfaces from core and found rocks with higher organic content had smooth fracture surfaces but more calcareous rocks produced surface morphologies such as plumose and arrest lines. The question that arises from this finding is whether the rock with higher organic content is producing a smooth surface, or whether the fracture morphology is too big to be detected by the finite core. The same issue is present in our surface studies, which shows a smooth surface over several 10x10 mm areas, but is possible that the area of study is too small to detect fracture morphologies.

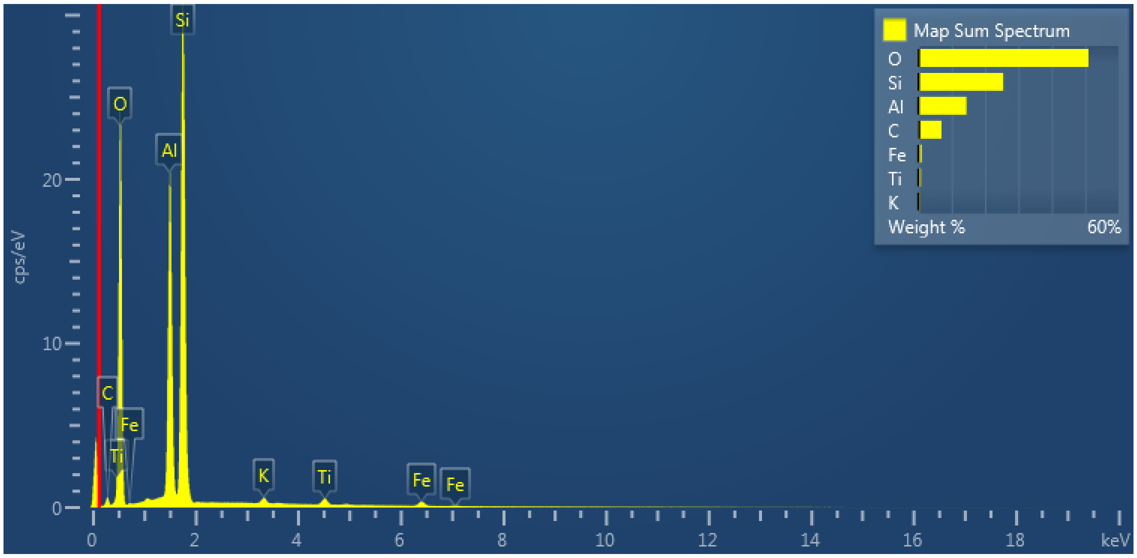

Figure 77: Elemental spectrum of Pyrophyllite. No traces of Field's metal can be seen in the secondary fracture network.

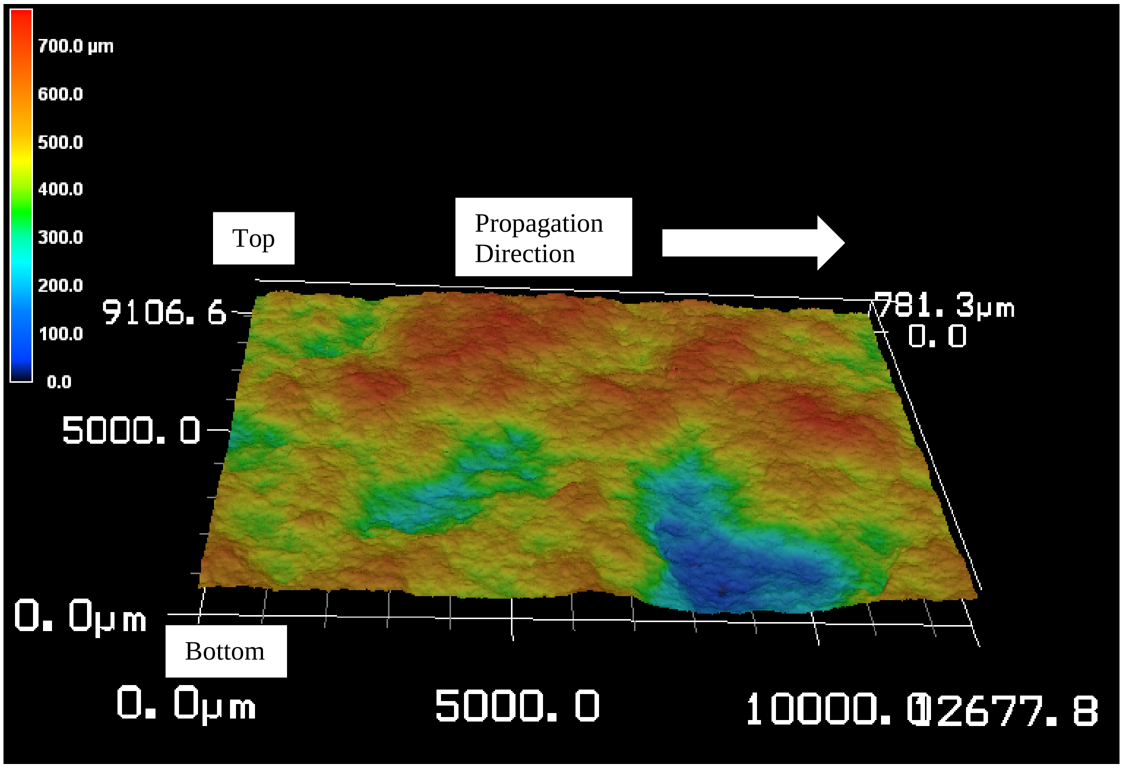

Figure 78: A 10x10 mm Keyence surface scan of the primary fracture RMS roughness. No distinguishable fracture morphologies can be recognized.

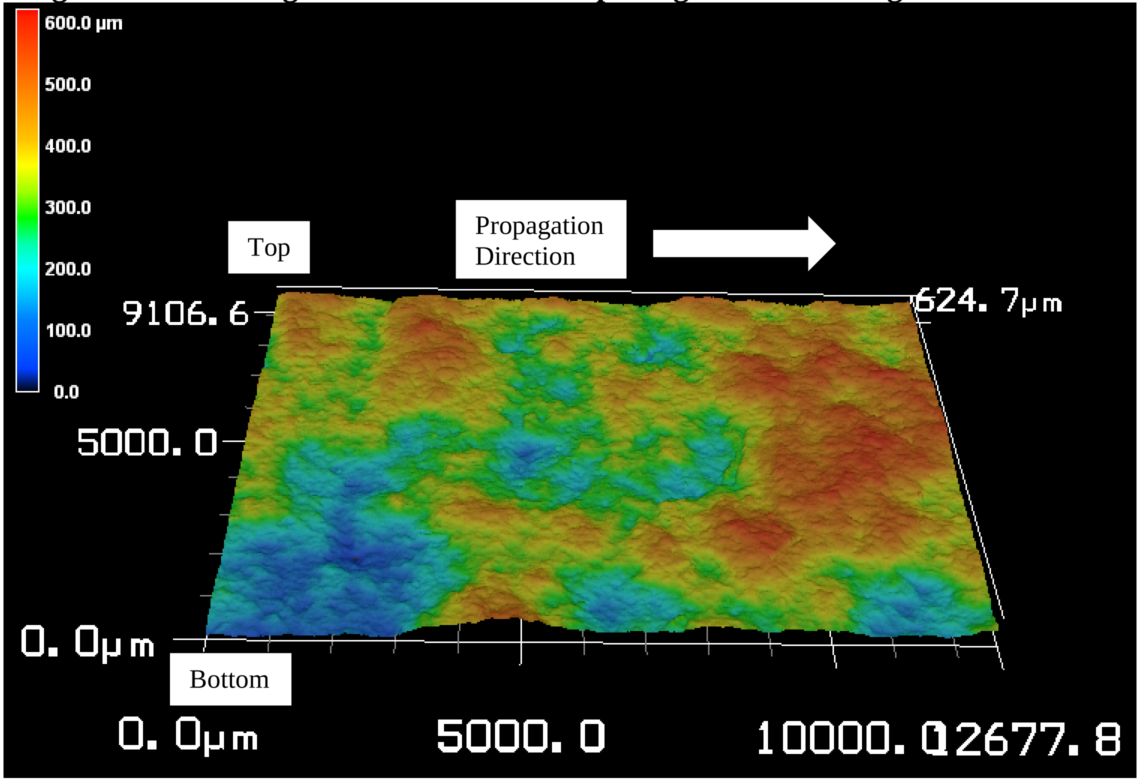

Figure 79: A 10x10 mm Keyence surface scan of the primary fracture RMS roughness. No distinguishable fracture morphologies can be recognized.

Chapter 5: Conclusions

5.1 Summary of Observations for the Tennessee Sandstone (A Triaxial Experiment)

1. Despite following grain boundaries, secondary fractures are primarily oriented 90˚ from the primary fracture.
2. The primary fracture does not propagate with a uniform velocity but rather propagates episodically. This is due to the build-up and release of stored energy as new volumes are created and pressure drops. The results can be seen in the modulated geometry of the process zone, fracture width, and intragranular fracture densities.
3. The size of incremental propagation in the primary fracture is controlled by the amount of energy (fluid) stored. Close to the injection point, the fracture travels much further before stopping and building energy again as opposed to near the termination point, where the build and release of energy occurs more frequently. This affects the pressure distribution into the secondary fracture network, causing the SRV to fluctuate with intermittent fracture growth.
4. The majority of SRA in the secondary fracture network comes from connecting pore space (68%) rather than the secondary fractures themselves (32%).
5. The secondary fracture network in the elastic zone increased the total fracture length by 25-fold. This increased the total stimulated porosity by nearly 300%.
6. Primary fracture width did not decrease in a linear manner but in 3 different phases. The zones nearest to the injection point and termination point behave similarly, with comparable negative slopes and length of zones. The middle zone

however, which includes over half the length of the fracture, shows relatively no decline in fracture width; suggesting the greatest loss of energy occurs at the initiation and termination of the fracture.

7. In contrast to observation in 4-point bending experiments, fracture density did not increase around the termination zone.
8. The plastic zone caused a 59% increase in the process zone, which resulted in the number of fractures to increase by 64%, while fracture density remained constant.
9. Hydraulic fracturing was further found to induce Dauphiné twins in quartz crystals while also changing the orientation of grains during fracture propagation. These crystallographic alterations can aid in fracture propagation by causing preferred slip planes. Dauphiné twins can also produce new fracture patterns due to weak twinning planes and increase SRV. These findings were observed in a single sample and more data needs to be collected.
10. A slow fracture propagation velocity creates a larger SRV. For sandstone, a high velocity causes secondary fractures to go through grains, which requires more energy and depletes the stored energy faster, resulting in a smaller process zone. At the fracture’s termination point, velocity is slow, promoting secondary fracturing along grain boundaries, thus conserving energy and allowing the fractures to propagate further into the formation. This increases the process zone and pore connectivity.

5.2 Summary of Observations for the Marcellus Shale and Pyrophyllite (Uniaxial Experiments Parallel to Bedding)

11. The Marcellus shale, vertical samples showed no signs of secondary fractures near injection point, where velocity is high, but secondary and tertiary fractures were found near the edge of the sample, where fracture velocity was low.
12. Different lithologies produce different fracture morphologies.
13. A nonuniform primary fracture in the Marcellus shale, causing the liquid Field's metal to distribute unevenly, raises the idea that instead of having a single, simple primary fracture, there are actually many microfractures linked together to form one macrofracture. The initiation and termination of many linked microfractures would create a non-uniform fracture plane and result in incomplete fluid migration.
14. Secondary fractures are longer in shale and pyrophyllite as compared to Tennessee sandstone. This is due to the smaller grains allowing the fracture to propagate without causing radical fracture misorientations that result in severe energy loss. The primary and secondary fractures in the Marcellus shale and pyrophyllite were propagating in the direction of bedding planes.
15. The fractured shale sample showed a significant number of nanofractures around the primary and secondary fractures. This illustrated that there are damage zones around individual fractures, creating damage zones within damage zones.

5.3 Conclusions

The importance of secondary microfractures can be seen in the SRV of Tennessee sandstone, which increased the total fractured volume by 25-fold and tripled the connected pore space. By propagating in a direction perpendicular to the primary fracture under a triaxial loading system, secondary fractures acted as a means of connecting micropores that were originally isolated. The greatest amount of SRV was found near the fracture termination point, suggesting that the physics between a propagating fracture tip and terminating fracture tip differ. It was further found that primary fractures with low velocities create larger SRV's, suggesting that a start-stop pumping process during hydraulic fracturing would be most beneficial. Grain misorientations and Dauphiné twins were also found in quartz crystals induced by hydraulic fracturing. These crystallographic alterations can aid in fracture propagation and SRV by changing the plane orientation and providing enhanced slip planes. It was further found that secondary fracture networks significantly decrease in the Marcellus shale and pyrophyllite samples but the tertiary fracture network increases, creating much more complex fractures in unconventional rocks. These results show that secondary fractures cannot be ignored when modeling SRV and fracture velocity must be taken into consideration.

5.4 Future Work

One limitation of these studies was the size of cores used. The sandstone and pyrophyllite cores were 4-inches in diameter by 6-inches tall. This only allows 2-inches (1-wing) of a fracture to be studied. Running these experiments on larger cores would allow a greater amount of data to be collected and could potentially find new results that are not limited to finite sample geometry.

Many similarities are shown between the microfracture network in lab experiments and the macrofracture network in outcrop **(Engelder, 1987; Lacazette and Engelder, 1992)**. However, these observations have been poorly applied to stimulated fracture networks induced by hydraulic fracturing. Additional field experiments need to be conducted and analyzed (such as the experiment in **Raterman et al., 2017**) to determine if these same fracture processes are occurring within hydraulically induced reservoirs. If so, these processes will significantly improve SRV modeling.

The injection of Field's metal into unconventional rocks posed difficulty when attempting to fracture the samples. Marcellus shale and pyrophyllite typically fail around 3500 psi when using a wetting brine fracturing fluid. However, when fracturing with nonwetting Field's metal (1.6 cP viscosity at 90˚C), the rock struggled to fail at 7000 psi. This suggests that the Field's metal was solidifying under pressure. Future experiments should take into consideration pressure induced viscosity.

A continuation of finding the best fracture fluid to highlight the fracture network for SEM and CT analysis, while also holding the network together during sample preparation should be continued. Next experiments should try Indium and Gallium for their high atomic number and low melting points.

To aid in the work of artificial intelligence (AI) for fracture counting, a high contrasting injection fluid should be used. A mixture of fluorescent dye in the fracturing fluid would illuminate the fracture networks and allow AI to count fractures more accurately.

Crystallographic studies need to be extended into limestone and shale samples. The ability for calcite to twin is somewhat "easier" (CRSS of 1450 psi) **(Lacombe, 2001)** than quartz and it is thus hypothesized that if hydraulic fracturing can produce twins in quartz, then it should produce twins in calcite. Crystallographic experiments should be conducted on all reservoirs to determine the reservoir’s ability to twin and misorient. The result will give a more accurate prediction of fracture propagation patterns.

Computer modeling in the elastic and plastic zone can be very time consuming but can also present great insight on how the fracture propagates and reacts to its surroundings. Because the fracture networks in these samples have been statistically documented, it would be beneficial to run simulation and evaluate their effect on production.

5.5 Limitations of the Study

1. The use of scanlines to count fracture statistics can create a bias depending on the direction of the scanline. For instance, it has been shown that secondary fractures primarily propagate perpendicular to the primary fracture and tertiary (intragranular) fractures typically propagate perpendicular to the secondary fractures (parallel to the primary fracture). This being so, an implementation of a perpendicular scanline would over estimate tertiary fractures and under estimate secondary fractures due to their orientations. Vice versa, if a horizontal scanline was implemented, one would over estimate secondary fractures and under estimate tertiary fractures. This limitation can be overcome by creating a grid system of perpendicular and parallel scanlines but then some fractures are most certainly being counted multiple times and accuracy decreases. Automated fracture counting software needs to be implemented to take away user and scanline biases. By doing so, the scanline constraint would be overcome, and all fractures would be counted rather than only the fractures that are crossed along a

scanline. This would provide more accurate fracture statistics that are not biased towards fracture orientation.

2. Non-uniform epoxy dispersion near the end of the process zone makes it difficult to determine which fractures are hydraulically induced and which fractures were not. At these locations, some fractures did not contain epoxy, but epoxy was found in the pore behind the fracture and in the pore in front of the fracture. Logically, it could be inferred that the fracture had to have been hydraulically connected to move the epoxy into the next pore. When counting fractures, one cannot just follow a set guideline but must incorporate common sense.
3. The grey scale contrast given by the CBS detector is based on the atomic number of the object being analyzed. Although the contrast between epoxy and quartz is high and easily distinguished, the contrast between epoxy and clay is much less. To the untrained eye, clay inside a pore can be mistaken for epoxy.

References

Anderson, T.L. 2017. *Fracture mechanics: fundamentals and applications*. CRC press.
AOGA. 2018. Facts and figures. https://www.aoga.org/facts-and-figures

Atkinson, B.K. 1979a. Fracture toughness of Tennessee sandstone and Carrara marble using the double torsion testing method. In *International Journal of Rock Mechanics and Mining Sciences & Geomechanics Abstracts*. **16**(1): 49-53.

Atkinson, B.K. 1979b. A fracture mechanics study of subcritical tensile cracking of quartz in wet environments. *Pure and Applied Geophysics*, ***117***(5): 1011-1024.

Atkinson, B.K. 1987. *Fracture Mechanics of Rock.* Elsevier.

Bahat, D. 1991. Tectonofractography. In *Tectonofractography:* 239-324. Springer, Berlin, Heidelberg.

Bahat, D., Rabinovitch, A., and Frid, V. 2009. Tensile fracturing in rocks: tectonofractographic and electromagnetic radiation methods. Berlin: Springer.

Barenblatt, G.I. 1959. The formation of equilibrium cracks during brittle fracture. General ideas and hypotheses. Axially – symmetric cracks. *Journal of Applied Mathematics and Mechanics*. **23**(3): 622-636. doi:10.1016/0021-8928(59)90157-1

Bertagnolli, E., Kittinger, E., and Tichý, J. 1979. Ferrobielastic hysteresis in α-quartz. *Journal of Applied Physics, **50***(10): 6267-6271.

Bhagat, A. 2012. Analysis of hydraulic fracture in Lyons sandstone using SEM. Presented at the Unconventional Shale Consortium. University of Oklahoma, Norman. June 14-15.

Biot, M.A., Masse, L., and Medlin, W. L. 1986. A two-dimensional theory of fracture propagation. *Society of Petroleum Engineers*. SPE-11067-PA. doi:10.2118/11067-PA

Blochwitz, C., Brechbühl, J., and Tirschler, W. 1995. Misorientation measurement near grain boundary cracks after fatigue tests. *Strength of Materials*, **27**(3): 11-25. doi:10.1007/BF02206406

Bocangel, W. 2013. Acoustic and topological characterization of organic matter in shales. Master’s Thesis. University of Oklahoma, Norman.

Brace, W. F., and Bombolakis, E. G. 1963. A note on brittle crack growth in compression. *Journal of Geophysical Research*, ***68***(12): 3709-3713.

Brace, W.F. 1977. Permeability from resistivity and pore shape. *Journal of Geophysical Research*, ***82***(23): 3343-3349.

Broberg, K.B. 1999. *Cracks and fracture*. San Diego, CA: Academic Press.

Budiansky, B., and O'Connell, R.J. 1976. Elastic moduli of a cracked solid. *International Journal of Solids and Structures*, ***12***(2), 81-97. doi.org/10.1016/0020-7683(76)90044-5

Byerlee, J. 1978. Friction of rocks. In *Rock friction and earthquake prediction*. pp. 615-626. Birkhäuser, Basel.

Carpinteri, A. 1984. Size effects in material strength due to crack growth and material non-linearity, *Theoretical and Applied Fracture Mechanics*, **2**(1): 39-45.

Carpinteri, A. 1985. Interpretation of the Griffith instability as a bifurcation of the global equilibrium. *Application of Fracture Mechanics to Cementitious Composites*. NATO ASI Series (Series E: Applied Sciences), **94**. Springer, Dordrecht.

Carpinteri, A., Cornetti, P., Barpi, F., and Valente, S. 2003. Cohesive crack model description of ductile to brittle size-scale transition: Dimensional analysis vs. renormalization group theory. *Engineering Fracture Mechanics*, ***70***(14): 1809-1839.

Carpinteri, A., Cornetti, P., Pugno, N., Sapora, A., and Taylor, D. 2009. Generalized fracture toughness for specimens with re-entrant corners: Experiments vs. theoretical predictions. *Structural Engineering Mech*anics, ***32***(5): 609-620.

Ceriolo, L., and Di Tommaso, A. 1998. Fracture mechanics of brittle materials: A historical point of view. Venice University Institute of Architecture. Venezia, Italia

Chesnutt, J.C., and Spurling, R.A. 1977. Fracture topography—microstructure correlations in the SEM. *Metallurgical Transactions A*, ***8***(1): 216-218. doi:10.1007/BF02677289

Curtis, M.E., Sondergeld, C.H., and Rai, C.S. 2013a. Investigation of the microstructure of shales in the oil window. *URTec, Denver, CO, Aug. 12-14.* SPE-168815/URTeC-1581844.

Curtis, M.E., Sondergeld, C.H., and Rai, C.S. 2013b. Relationship between organic shale microstructure and hydrocarbon generation. *Society of Petroleum Engineers*. SPE-164540-MS.

Curtis, M.E., Goergen, E.T., Jernigen, J.D., Sondergeld, C.H., Ambrose, R.J., and Rai, C.S. 2014. Mapping of organic matter distribution on the centimeter scale with nanometer resolution. *Unconventional Resources Technology Conference, Denver, CO, Aug. 25-27*. SPE-1922757.

Curtis, M.E. 2017. Lecture 1 (introduction to microscopy and SEM), 2 (vacuum, power, and environmental requirements in SEM), and 5 (beam-specimen interactions). Presented at the University of Oklahoma, Norman, OK.

Damani, A., Sharma, A., Sondergeld, C.H., and Rai, C.S. 2012. Acoustic emission and SEM analyses of hydraulic fractures under triaxial stress conditions. *Society of Exploration Geophysicists*. SEG-2012-1585

Damani, A. 2013. Acoustic mapping and fractography of laboratory induced hydraulic fractures. Master's Thesis. University of Oklahoma, Norman.

Dapples, E., and Rominger, J. F. 1945. Orientation analysis of fine-grained clastic sediments: A report of progress. *The Journal of Geology*, ***53***(4): 246-261.

Dieter, G.E. 1988. *Mechanical Metallurgy*, 3rd Edition. London: Mcgraw hill

Dong, Y., and de Pater, C.J. 2008. Observation and modeling of the hydraulic fracture tip in sand. In *The 42nd US Rock Mechanics Symposium (USRMS)*. American Rock Mechanics Association.

Dugdale, D.S. 1960. Yielding of steel sheets containing slits. Journal of the Mechanics and Physics of Solids. **8**(2): 100-104. doi.org/10.1016/0022-5096(60)90013-2

Dunn, D.E., LaFountain, L.J., and Jackson, R.E. 1973. Porosity dependence and mechanism of brittle fracture in sandstones. *Journal of Geophysical Research*, ***78***(14): 2403-2417.

Dunn, K.J., Bergman, D.J., and LaTorraca, G.A. 2002. Nuclear magnetic resonance: Petrophysical and logging applications. *Seismic Exploration*, **32.** Elsevier.

EIA. 2008. Maps: Exploration, Resource, Reserve, and Production. https://www.eia.gov/maps/images/field_maps/AK_NorthSlope_BOE.pdf

EIA. 2010. Maps: Exploration, Resource, Reserves, and Production. https://www.eia.gov/maps/maps.htm.

EIA. 2016. Maps: Exploration, Resource, Reserves, and Production. https://www.eia.gov/maps/maps.htm. 6 June.

EIA. 2018. Frequently Asked Questions. https://www.eia.gov/tools/faqs/faq.php?id=907&t=8

El-Monier, I. 2016. Evaluation of rock damage and fracture propagation on microcracks development and stimulation quality of tight formations: Quantitative and statistical characterization. *URTec, San Antonio, TX, Aug. 1-3. URTEC-2460196-MS*

Engelder, T. 1987. Joints and shear fractures in rock. *Fracture mechanics of rock*, 27-69.

Entov, V., Chekhonin, E.M., Detournay, E., and Thiercelin, M.J. 2007. Fracture propagation in high-permeability rocks: The key influence of fracture tip behavior. *Society of Petroleum Engineers*, SPE-106225-MS. doi:10.2118/106225-MS

Field's Metal [Digital image]. (n.d.). Retrieved from https://www.reade.com/products/wood-s-metal-alloy

Friedman, M., and Johnson, B. 1978. Thermal cracks in unconfined Sioux quartzite. Proc. 19th U.S. Symp. Rock Mechanics, Reno. Nev., pp. 423-430.

Friedman, M., Handin, J., and Bauer. S.J. 1982. Deformation mechanisms in granodiorite at effective pressures to 100 MPa and temperatures to partial melting. Proc. 23rd U.S. Symp. Rock Mechanics, Berkeley, Calif., pp. 279-289.

Goergen, E.T., Curtis, M., Jernigen, J., Sondergeld, C.H., and Rai, C.S. 2014. Integrated petrophysical properties and multi-scaled SEM microstructural characterization. *Unconventional Resources Technology Conference (URTEC).*

Goldstein, J.I., Newbury, D.E., Michael, J.R., Ritchie, N.W., Scott, J.H.J., and Joy, D.C. 2017. *Scanning electron microscopy and X-ray microanalysis*. 4th Edition. Springer.

Griffiths, J.C. 1950. Directional permeability and dimensional orientation in Bradford sand. *Producers Monthly*, ***14***(8), 26-32.

Hadley, K. 1976. Comparison of calculated and observed crack densities and seismic velocities in Westerly granite. *Journal of Geophysical Research*, ***81***(20): 3484-3494.

Hallbauer, D.K., Wagner, H.N.G.W., and Cook, N.G.W. 1973. Some observations concerning the microscopic and mechanical behaviour of quartzite specimens in stiff, triaxial compression tests. *International Journal of Rock Mechanics and Mining Sciences & Geomechanics Abstracts*, **10**(6): 713-726

Heidelbach, F., Kunze, K., and Wenk, H.R. 2000. Texture analysis of a recrystallized quartzite using electron diffraction in the scanning electron microscope. *Journal of Structural Geology*, ***22***(1), 91-104.

Hillerborg, A., Modéer, E., and Petersson, P.E. 1976. Analysis of crack formation and crack growth in concrete by means of fracture mechanics and finite elements. *Cement and Concrete Research*, **6**(6): 773-781. doi.org/10.1016/0008-8846(76)90007-7

Jacobs, T. 2014. Renewing mature shale wells through refracturing. *Journal of Petroleum Technology*, **66**(4): 52-60. SPE-0414-0044-JPT. doi:10.2118/0414-0044-JPT

Jacobs, T. 2015. Changing the equation: Refracturing shale oil wells. *Journal of Petroleum Technology*, **67**(4): 44-49. SPE-0415-0044-JPT. doi:10.2118/0415-0044-JPT

Janssen, C., Wagner, F., Zang, A., and Dresen, G. 2001. Fracture process zone in granite: A microstructural analysis. *International Journal of Earth Sciences*, ***90***(1): 46-59.

Jarvie, D.M., and Tobey, M.H. 1999. TOC, rock-eval and SR analyzer interpretive guidelines. In *Application Note 99-4*. Humble Instruments and Services, Inc. Geochemical services Division Texas.

Jones, R.W. 1984. Comparison of carbonate and shale source rocks. *Petroleum Geochemistry and Source Rock Potential of Carbonate Rocks: AAPG Studies in Geology*, 18: 163-180.

Kalihari, V., Tadmor, E.B., Haugstad, G., and Frisbie, C.D. 2008. Grain orientation mapping of polycrystalline organic semiconductor films by transverse shear microscopy. *Advanced Materials*, ***20***(21): 4033-4039.

Kassis, S., and Sondergeld, C.H. 2010. Fracture permeability of gas shale: Effect of roughness, fracture offset, proppant, and effective stress. In *International Oil and Gas Conference and Exhibition in China*. Society of Petroleum Engineers. SPE-131376-MS

Ko, L.T., Loucks, R.G., Ruppel, S.C., Zhang, T., and Peng, S. 2017. Origin and characterization of Eagle Ford pore networks in the south Texas Upper Cretaceous shelf, AAPG BULL., **101**(3): 387-418.

Kranz, R.L. 1979. Crack growth and development during creep of Barre granite. In *International Journal of Rock Mechanics and Mining Sciences & Geomechanics Abstracts*, **16**(1): 23-35.

Kranz, R.L. 1983. Microcracks in rocks: A review. *Tectonophysics,* **100**(1-3), 449-480. doi:10.1016/0040-1951(83)90198-1

Kulander, B. R., Barton, C. C., and Dean, S. L. 1979. *Application of fractography to core and outcrop fracture investigations* (No. METC/SP-79/3). Department of Energy, Morgantown, WV (USA). Morgantown Energy Research Center.

Lacazette, A., and Engelder, T. 1992. Fluid-driven cyclic propagation of a joint in the Ithaca siltstone, Appalachian Basin, New York. In *International Geophysics*. **51**: 297-323. Academic Press.

Lacombe, O. 2001. Paleostress magnitudes associated with development of mountain belts: Insights from tectonic analyses of calcite twins in the Taiwan Foothills. *Tectonics*, ***20***(6): 834-849.

Lemmens, H.J., Butcher, A.R., and Botha, P.W.S.K. 2011. FIB/SEM and SEM/EDX: a new dawn for the SEM in the Core Lab?. *Petrophysics*, ***52***(06): 452-456. SPWLA-V52N6A4

Liao, Y. 2006. Practical electron microscopy and database. www.globalsino.com/EM/.

Lindgren, P., Price, M.C., Lee, M.R., and Burchell, M.J. 2013. Constraining the pressure threshold of impact induced calcite twinning: implications for the deformation history of aqueously altered carbonaceous chondrite parent bodies. *Earth and Planetary Science Letters*, *384*: 71-80.

Lindley J.R. 2011. Hydraulic Fracturing. *National Energy Technology Laboratory*.

Low Viscosity Epoxy [Digital image]. (n.d). Retrieved from http://www.polysciences.com/default/embed-it-low-viscosity-epoxy-kit

Mayerhofer, M.J., Lolon, E., Warpinski, N.R., Cipolla, C.L., Walser, D.W., and Rightmire, C.M. 2010. What is stimulated reservoir volume? *Society of Petroleum Engineers*. SPE-119890-PA. doi:10.2118/119890-PA

McMeeking, R.M. 1977. Finite deformation analysis of crack-tip opening in elastic-plastic materials and implications for fracture. *Journal of the Mechanics and Physics of Solids*, ***25***(5): 357-381.

Mikhailov, D.N., Economides, M.J., and Nikolaevskiy, V.N. 2011. Fluid leak off determines hydraulic fracture dimensions: Approximate solution for non-Newtonian fracturing fluid. *International Journal of Engineering Science*, **49**(9): 809-822.

Mogi, K. 1962. Study of elastic shocks caused by the fracture of heterogeneous materials and its relation to earthquake phenomena. *Bull. Earthq. Res. Inst., Univ. Tokyo*, *40*: 125-173.

Mogi, K. 1963. The Fracture of a semi-infinite body cased by an inner stress origin and its relation to the earthquake phenomena. *Bull. Earthq. Res. Inst., 41*: 615-658.

Montgomery, S. 2017. Large-scale fracking comes to the Arctic in a new Alaska oil boom. *The Conversation*. 12, April. http://theconversation.com/large-scale-fracking-comes-to-the-arctic-in-a-new-alaska-oil-boom-75683

Nasseri, M.H.B., Mohanty, B., and Young, R.P. 2006. Fracture toughness measurements and acoustic emission activity in brittle rocks. *Pure and Applied Geophysics*, **163**(5-6): 917-945.

Nemati, K.M. 1997. Fracture analysis of concrete using scanning electron microscopy. *SCANNING*, ***19***(6): 426-430.

Nohava, J., Haušild, P., Karlık, M., and Bompard, P. 2002. Electron backscattering diffraction analysis of secondary cleavage cracks in a reactor pressure vessel steel. *Materials Characterization*, **49**(3): 211-217. doi:10.1016/S1044-5803(02)00360-1

Odusina, E.O. 2011. An NMR study of shale wettability. Master's Thesis, University of Oklahoma, Norman.

Ortega, O.J., Marrett, R.A., and Laubach, S.E. 2006. A scale-independent approach to fracture intensity and average spacing measurement. *AAPG bulletin*, **90**(2): 193-208.

Padin, A., Tutuncu, A.N., and Sonnenberg, S. 2014. On the mechanisms of shale microfracture propagation. In *SPE Hydraulic Fracturing Technology Conference*. Society of Petroleum Engineers. doi:10.2118/168624-MS

Paris, P.C. 1961. A rational analytic theory of fatigue. *Trends Engin*, *13*, 9-14.

Paris, P., and Erdogan, F. 1963. A critical analysis of crack propagation laws. *Journal of basic engineering*, ***85***(4): 528-533.

Perez, N. 2004. *Fracture Mechanics*. Norwell, MA: Kluwer Academic.

Peng, S., and Johnson, A.M. 1972. Crack growth and faulting in cylindrical specimens of Chelmsford granite. In *International Journal of Rock Mechanics and Mining Sciences & Geomechanics Abstracts*, **9**(1): 37-86.

Pouya, A., Nguyen, V.L., and Ghabezloo, S. 2014. Hydraulic fracture propagation under steady state flow. In *48th US Rock Mechanics/Geomechanics Symposium*. American Rock Mechanics Association.

Prasad, M. 2002. Mapping impedance microstructures in rocks with acoustic microscopy. *The landing Edge*, **20**(2): 172-179.

Prasad, M., and Milliken, K. 2015. Pore types and pore-size distributions across thermal maturity, Eagle Ford formation, southern Texas. *AAPG Bulletin*, **99**(9): 1713-1744.

Quorum Technologies. N.d. Sputter coating technical brief. Document Number TB-Sputter. **2**(01/02). http://www.iitk.ac.in/meesa/SEM/coater_manual_technical.pdf

Rahl, J.M., McGrew, A.J., Fox, J.A., Latham, J.R., and Gabrielson, T. 2018. Rhomb-dominated crystallographic preferred orientations in incipiently deformed quartz sandstones: A potential paleostress indicator for quartz-rich rocks. *Geology*.

Rahman, M.M. and Rahman, M.K. 2010. A review of hydraulic fracture models and development of an improved pseudo-3D model for stimulating tight oil/gas sand. *Energy Sources. Part A: Recovery, Utilization, and Environmental Effects*, **32**(15): 1416-1436. doi:10.1080/15567030903060523

Rho, S., Noynaert, S., Bunger, A.P., Zolfaghari, N., Xing, P., Abell, B., and Suarez-Rivera, R. 2017. Finite-element simulations of hydraulic fracture height growth on layered mudstones with weak interfaces. In *51st US Rock Mechanics/Geomechanics Symposium*. American Rock Mechanics Association.

Roylance, D. 2001. Introduction to fracture mechanics. *Massachusetts Institute of Technology, Cambridge, 1*.

Saxena, A. 1998. *Nonlinear fracture mechanics for engineers*. Boca Raton, Fla.: CRC Press.

Scholz, C.H. 1968a. Microfractures, aftershocks, and seismicity. *Bulletin of the Seismological Society of America*, ***58***(3): 1117-1130.

Scholz, C. H. 1968b. Microfracturing and the inelastic deformation of rock in compression. *Journal of Geophysical Research*, ***73***(4): 1417-1432.

Schubnikov, A. and Zinserling, K. 1932, Ueber die Schlag- und Druckfiguren und ueber die mechanischen Quarzzwillinge. *Z. Kristallogr*, 83: 243-264

Schwarzacher, W. 1951. Grain orientation in sands and sandstones. *Journal of Sedimentary Research*, ***21***(3): 162-172.

Simmons, G., and Richter, D. 1976. Microcracks in rocks. *The Physics and Chemistry of Minerals and Rocks*, 105-137.

Sondergeld, C.H., Ambrose, R.J., Rai, C.S., and Moncrieff, J. 2010. Micro-structural studies of gas shales. In *SPE Unconventional Gas Conference*. Society of Petroleum Engineers. SPE-131771-MS

Sondergeld, C.H., and Estey, L.H. 1981. Acoustic emission study of microfracturing during the cyclic loading of Westerly granite. *Journal of Geophysical Research: Solid Earth*, ***86***(B4): 2915-2924.

Sprunt, E.S., and Brace, W.F. 1974. Direct observation of microcavities in crystalline rocks. In *International Journal of Rock Mechanics and Mining Sciences & Geomechanics Abstracts*, **11**(4): 139-150.

Spurr, A.R. 1969. A low-viscosity epoxy resin embedding medium for electron microscopy. *Journal of Ultrastructure Research*, ***26***(1-2): 31-43.

Strother, D., Valadares, R., Nakhwa, A.D., and Pither, J. L. 2013. Challenges of refracturing horizontal wells in unconventional and tight reservoirs. *Society of Petroleum Engineers*. SPE-167000-MS. Doi:10.2118/167000-MS.

Suri, Y. 2011. Predicting petrophysical properties using SEM Image. In *SPE Reservoir Characterisation and Simulation Conference and Exhibition*. Society of Petroleum Engineers. SPE-144434-MS

Swanson, P.L., and Spetzler, H. 1979. Stress corrosion of single cracks in flat plates of rock. *Trans. Am. Geophys. Union, EOS, **60***(380).

Tapponnier, P., and Brace, W.F. 1976. Development of stress-induced microcracks in Westerly granite. In *International Journal of Rock Mechanics and Mining Sciences & Geomechanics Abstracts*, **13**(4): 103-112.

Tran, N.H., and Rahman, S.S. 2006. Modelling discrete fracture networks using neuro-fractal-stochastic simulation. *Journal of Engineering and Applied Sciences*, ***1***(2): 154-160.

Tullis, J. 1970. Quartz: preferred orientation in rocks produced by Dauphine twinning. *Science* 168: 1342-1344.

Tullis, J., and Tullis, T. 1972. Preferred orientation of quartz produced by mechanical Dauphiné twinning: thermodynamics and axial experiments. *Flow and Fracture of Rocks*, 67-82.

Varfolomeev, I., Yakimchuk, I., Denisenko, A., Khasanov, I., Osinceva, N., and Rahmattulina, A. 2016. Integrated study of thin sections: optical petrography and electron microscopy. *Society of Petroleum Engineers*. SPE-182071-MS. doi:10.2118/182071-MS

Warpinski, N. R. 1985. Measurement of width and pressure in a propagating hydraulic fracture. *Society of Petroleum Engineers*. SPE-11648-PA. doi:10.2118/11648-PA

Warpinski, N.R., Mayerhofer, M.J., Vincent, M.C., Cipolla, C.L., and Lolon, E.P. 2009. Stimulating unconventional reservoirs: Maximizing network growth while optimizing fracture conductivity. *Society of Petroleum Engineers*. SPE-114173-PA. doi:10.2118/114173-PA

Wawersik, W.R., and Brace, W.F. 1971. Post-failure behavior of a granite and diabase. *Rock mechanics*, ***3***(2): 61-85.

Wenk, H.R., Rybacki, E., Dresen, G., Lonardelli, I., Barton, N., Franz, H., and Gonzalez, G. 2006. Dauphiné twinning and texture memory in polycrystalline quartz. Part 1: experimental deformation of novaculite. *Physics and Chemistry of Minerals*, ***33***(10): 667.

Wenk, H.R., Bortolotti, M., Barton, N., Oliver, E., and Brown, D. 2007. Dauphiné twinning and texture memory in polycrystalline quartz. Part 2: In Situ neutron diffraction compression experiments. *Physics and Chemistry of Minerals*, ***34***(9): 599-607.

Wenk, H.R., Janssen, C., Kenkmann, T., and Dresen, G. 2011. Mechanical twinning in quartz: shock experiments, impact, pseudotachylites and fault breccias. *Tectonophysics*, ***510***(1-2): 69-79.

Wilkinson, R. 2017. Oil search to buy assets in Alaska's North Slope. Oil & Gas Journal. Presented in Melbourne, Australia, 1 November. http://www.ogj.com/articles/2017/11/oil-search-to-buy-assets-in-alaska-s-north-slope.html

Wong, T.F., Fredrich, J.T., and Gwanmesia, G.D. 1989. Crack aperture statistics and pore space fractal geometry of Westerly granite and Rutland quartzite: Implications for an elastic contact model of rock compressibility, *J. Geophys. Res.*, **94**(B8): 10267–10278, doi:10.1029/JB094iB08p10267.

Yaw, pitch, and roll illustration [Digital image]. 2017. Retrieved from www.mechscience.com/pitch-yaw-and-roll-aircraft-design-aeronautical-engineering-basics-concept-of-tail-plane-aircraft-motion-controls/

Yew, C.H., and Weng, X. 2014. *Mechanics of Hydraulic Fracturing*. 2nd Edition. Gulf Professional Publishing, Houston, TX.

Zang, A., Wagner, F.C., Stanchits, S., Janssen, C., and Dresen, G. 2000. Fracture process zone in granite. *Journal of Geophysical Research: Solid Earth*, ***105***(B10): 23651-23661. Doi:10.1029/2000JB900239

Zang, A. and Stephansson, O. 2010. *Stress Field of the Earth's Crust*, Springer. doi:10.1007/978-1-4020-8444-7

Zhang, W. and Liu Y. 2014. In-situ SEM testing for transient fatigue crack growth behavior investigation subjected to a single tensile overload. Proceedings of the *ASME 2014 International Mechanical Engineering Congress & Exposition*, November 14-20, Montreal, Quebec, Canada.

Zhou, W., Apkarian, R., Wang, Z.L., and Joy, D. 2006. Fundamentals of scanning electron microscopy (SEM). In *Scanning microscopy for nanotechnology*, pp. 1-40. Springer New York.

Zimmerle, W., and Bonham, L.C. 1962. Rapid methods for dimensional grain orientation measurements. *Journal of Sedimentary Research*, ***32***(4): 751-763.

Appendix A: Terminology

1. Secondary Fracture: A fracture that is derived from the primary fracture.
2. Tertiary Fracture: A fracture that is derived from the secondary fracture.
3. Intergranular Fracture: A fracture that follows grain boundaries. This is a low energy fracture.
4. Intragranular Fracture: A fracture that travels through grains. This is a high energy fracture. The primary fracture is almost always an intragranular fracture.
5. Secondary Fracture Orientation (Azimuth): The angle at which the secondary fracture propagates in regard to the primary fracture. A 90˚ azimuth is perpendicular to the primary fracture and a 0˚ or 180˚ azimuth is parallel to the primary fracture.
6. Fracture Density: The quantity of fractures in a given distance.
7. Process Zone: The area that the secondary fracture network extends into the formation. This is determined by finding the length of secondary fracture intrusion and multiplying by the study area length.
8. Orientation: The rotation of the crystal lattice structure with respect to some reference frame.
9. Crystal Lattice: The symmetrical arrangement of atoms inside a crystal.
10. Misorientation: The orientation of one crystal lattice with respect to another. Sometimes termed the orientation difference or next neighbors.
11. Euler Angles: The rotation(s) needed to bring the sample reference frame into coincidence with the crystal reference frame. Noted as ϕ, ϕ_1, and ϕ_2.
12. Fracture Face: The primary void space that is created by the fracture

13. Simple Fracture: A fracture that has a small secondary fracture density branching from it.
14. Complex Fracture: A fracture that has a high secondary fracture density branching from it.
15. Damage Zone: The immediate area around a fracture that contains secondary or tertiary fractures.

Appendix B: The Fundamentals of SEM

B1: Resolution and Abbe's Equation

SEM permits imaging below the resolution of visible light **(Curtis, 2017)**. To do so, magnification and resolution need to be considered. Resolution is defined by the minimum distance two objects can be separated and still appear as two distinct objects **(Zhou et al., 2006)**. This resolution for an SEM will depend on the wavelength propagating from the electron source and the limitation of the imaging system (i.e. the electron optics). Because levels of interference occur during wave propagation, the light wave cannot concentrate at a specific point but instead gradually fades from the light beam midpoint. The circle of light that is produced is called the Airy disk (**Fig. B1)**. When two or more Airy disks have separated greater than the radius of the disk, then two objects are said to have a high enough resolution to be distinguished from one another **(Zhou et al., 2006)**. In a perfect imaging system, the resolution is expressed by Abbe's equation:

$$d = \frac{.612\lambda}{n * \sin(\alpha)} \qquad (2.1)$$

Where:

d = Resolution

λ = wavelength of incident light

$n * \sin(\alpha)$ = Numerical Aperture.

a = half the aperture angle in radians

n = Index of refraction between the lens and sample surface

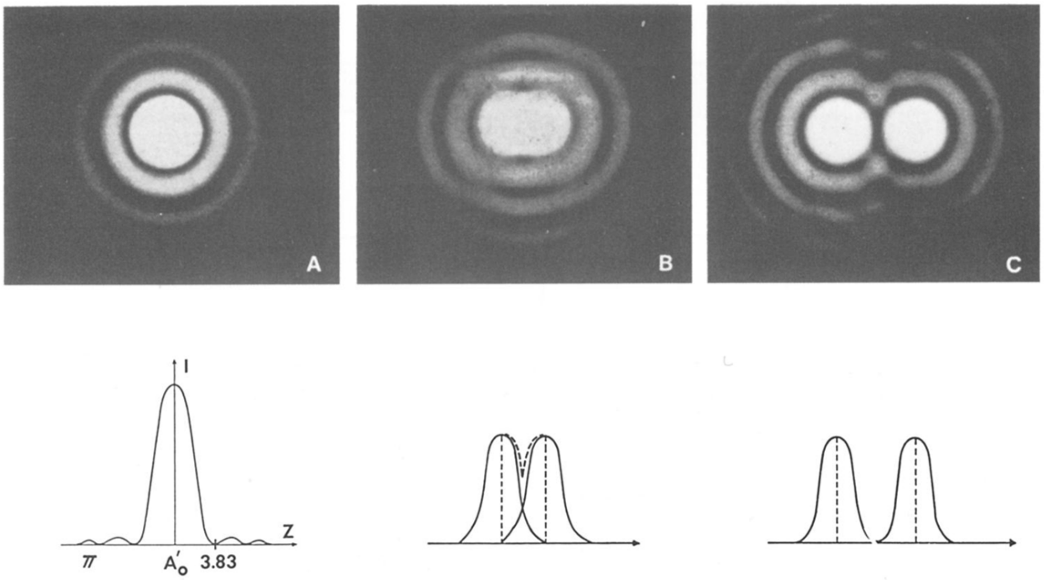

Fig. B1: Illustration of an optical microscope. As two Airy disks separate, the resolution increases and two objects can be distinguished from each other (Liao, 2013).

B2: Electron Source and Signals

The interaction between the electron beam and sample surface is the foundation of SEM imaging. The process can be divided into two main categories, elastic and inelastic electron interactions. Elastic interactions involve the deflection of electrons by colliding with the specimen's atomic nucleus and is therefore dependent on an atomic number **(Goldstein et al., 2017)**. It is important to note that most of the energy of the electron is conserved under these conditions. The reflection of the conserved electrons yields an important signal comprised of backscattered electrons (BSE), which is used for surface analysis. Inelastic scattering takes place under similar circumstances only the kinetic energy of the electron is not conserved **(Zhou et al., 2006)**. The result is a signal known as secondary electrons. Unlike elastic interactions, these electrons lose most of their energy on contact with the surface and are defined as containing less than 50 eV (**Curtis, 2017)**. Although low energy, this signal is a fundamental source for surface analysis. **Fig. B2** shows the different signals that are produced when the electron beam collides with the sample surface, including cathodoluminescence, Auger electrons, and X-rays. However, BSE and secondary electrons are the primary sources analyzed for this experiment.

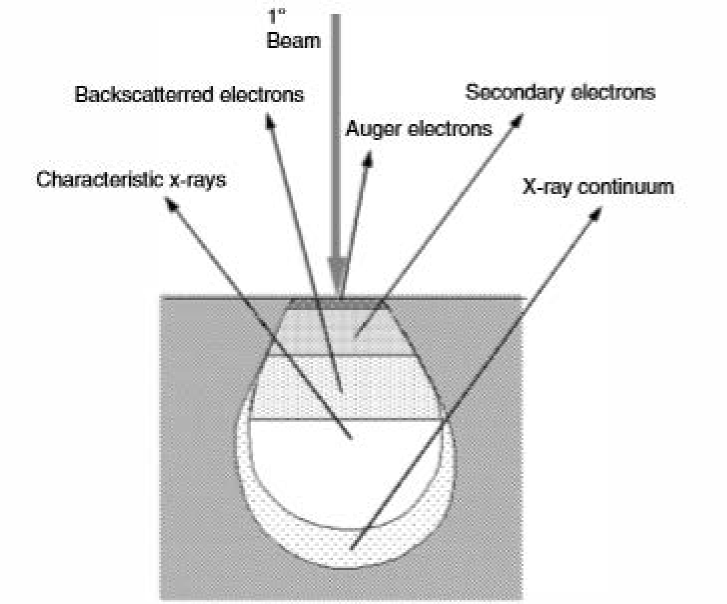

Fig. B2: Illustrations of different types of signals produced when an electron beam interacts with a sample surface. A teardrop zone is formed below the surface indicating the level of penetration controlled by the accelerating voltage and atomic number. A higher atomic number will stop the number of electrons that can penetrate the sample. Vice versa, a high voltage will allow a stronger penetration but could cause a loss of surface detail due to an over electron excitation (Zhou et al., 2006)

Appendix C: Additional Crystallography Data

C1: Native Tennessee Sandstone Sample #2

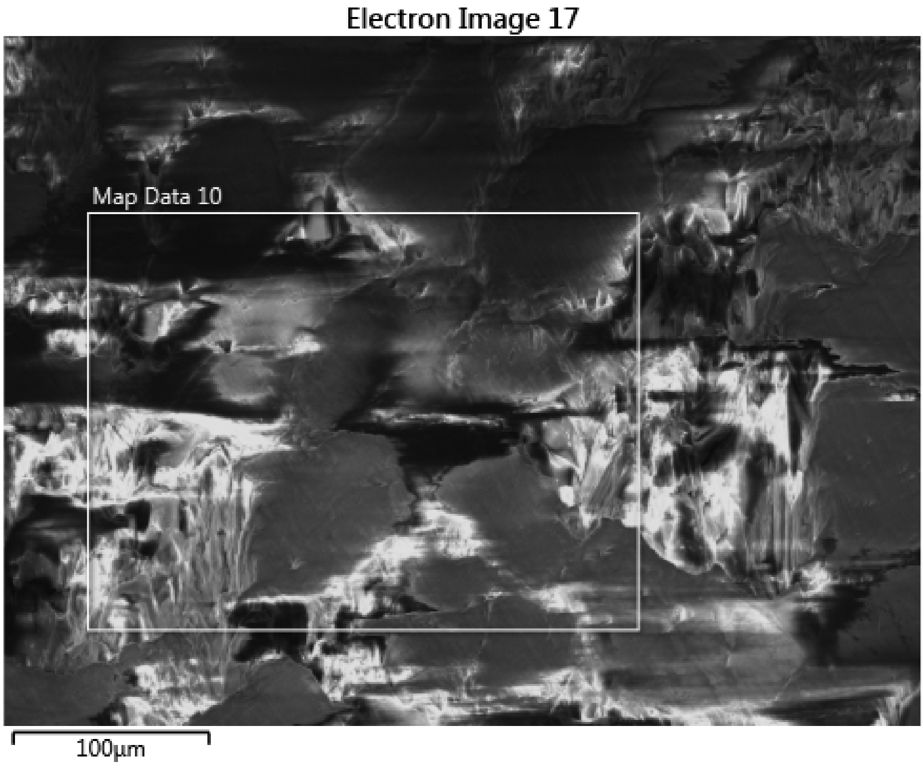

Figure C1: Area of study for the second native sample.

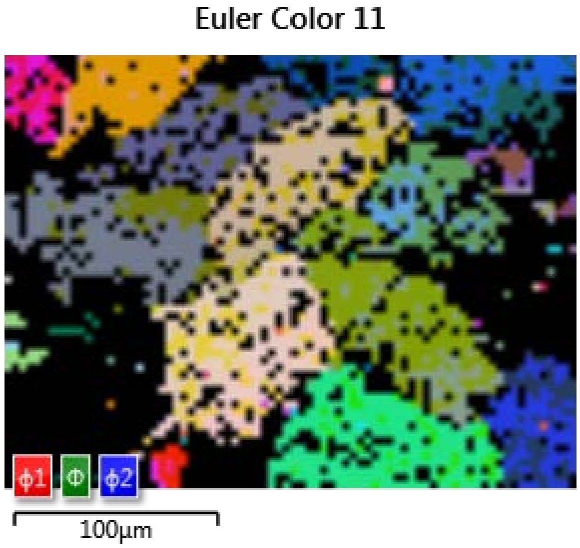

Figure C2: Complete Euler map showing the orientation of the crystals and the amount of data collected. Approximately 58% of diffraction patterns could be recognized.

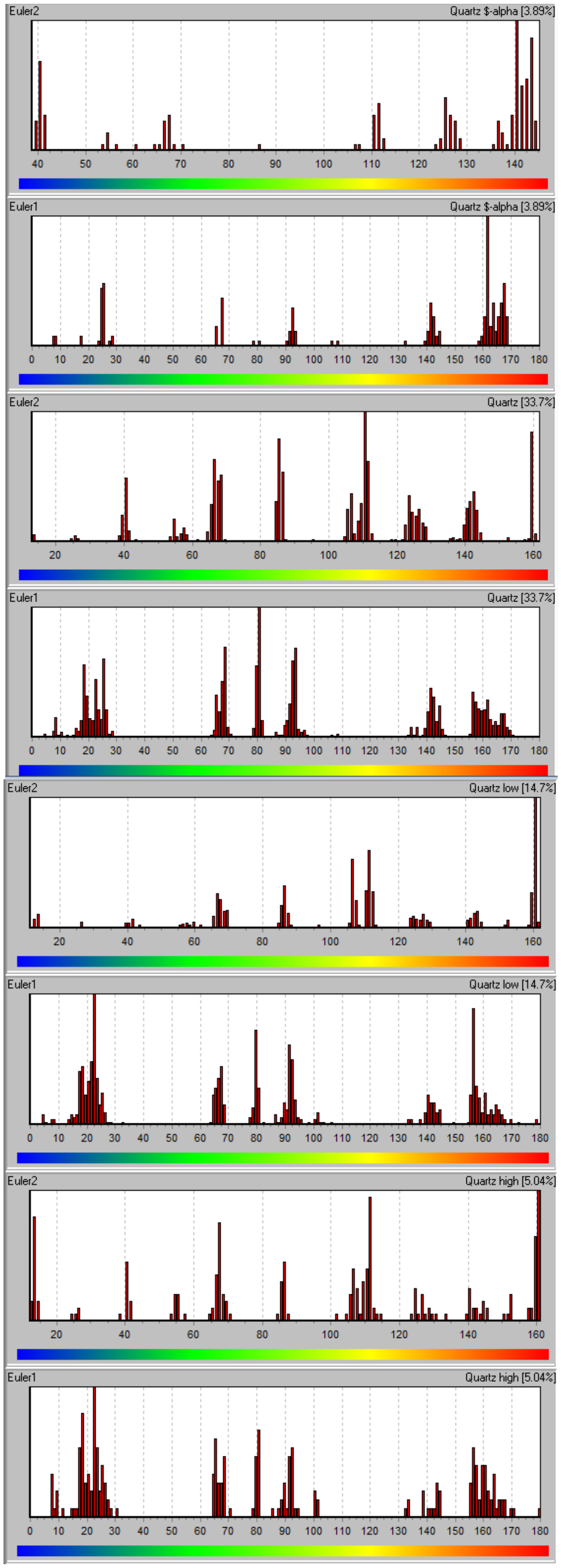

Figure C3: Histograms representing the $\emptyset$ and $\emptyset_1$ comparison for the second native sample. Many correlations can be seen, satisfying condition 1.

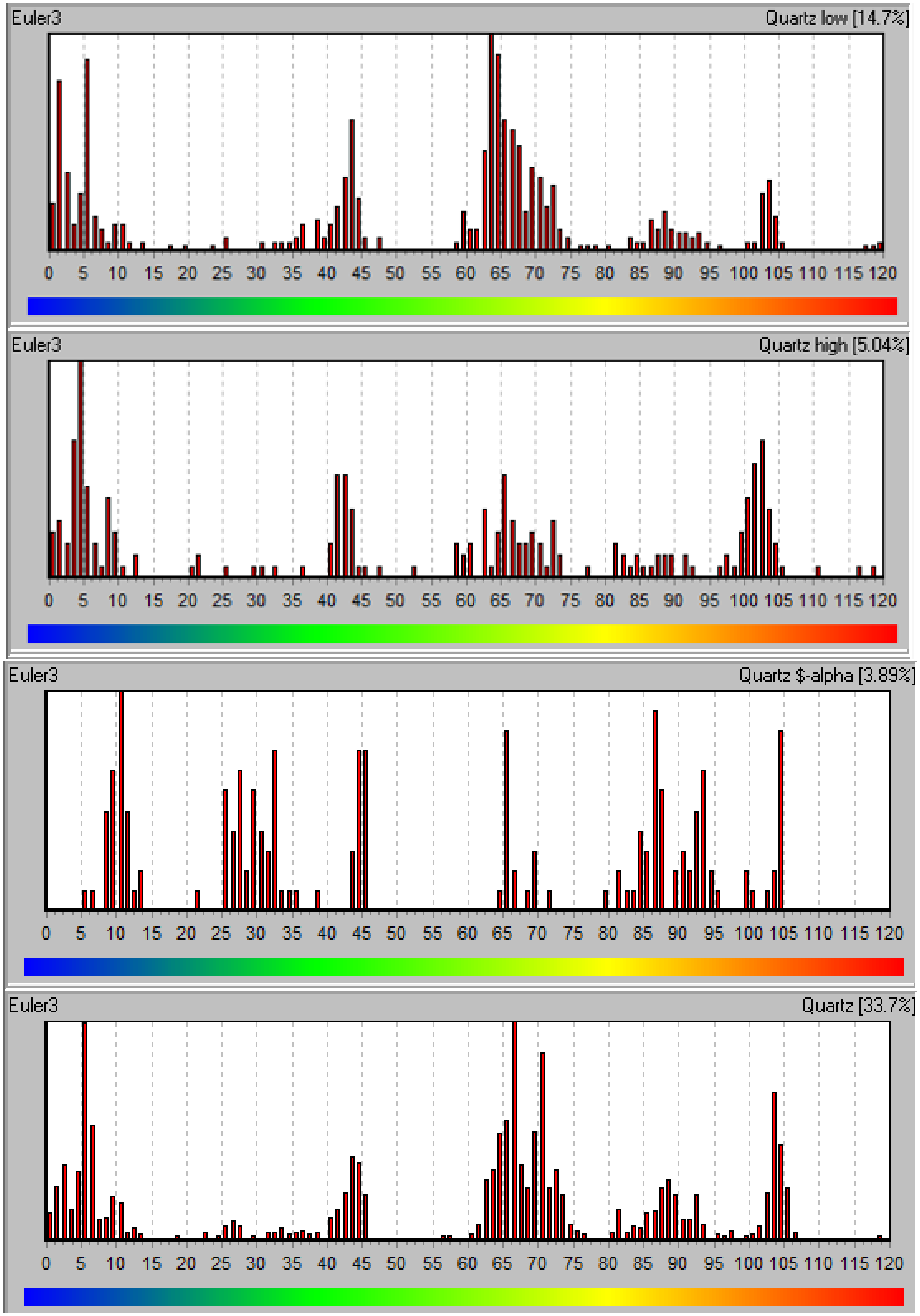

Figure C4: Histograms representing the rotations around the z-axis ($\varnothing_2$). Notice there are some 60° rotations prior to fracturing.

D2: Native Tennessee Sandstone Sample #3

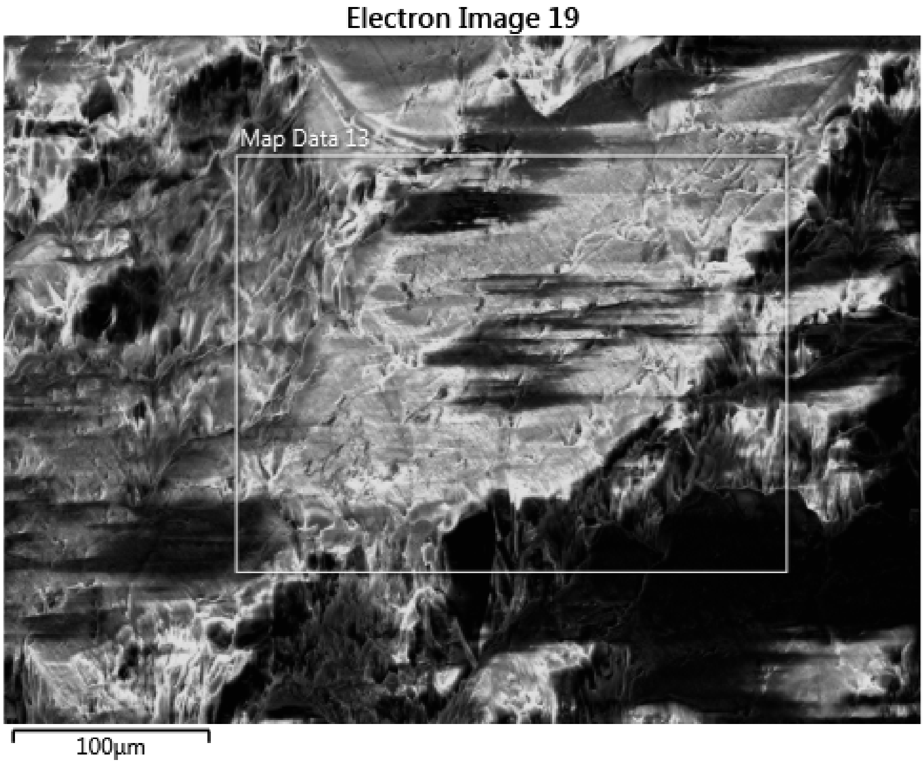

Figure C5: Area of study for the third native Tennessee sandstone experiment.

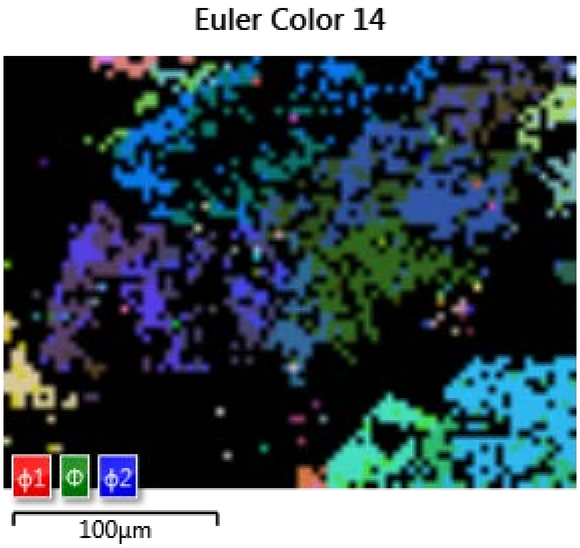

Figure C6: Complete Euler map showing the orientation of the crystals and the amount of data collected. Approximately 34% of diffraction patterns could be recognized.

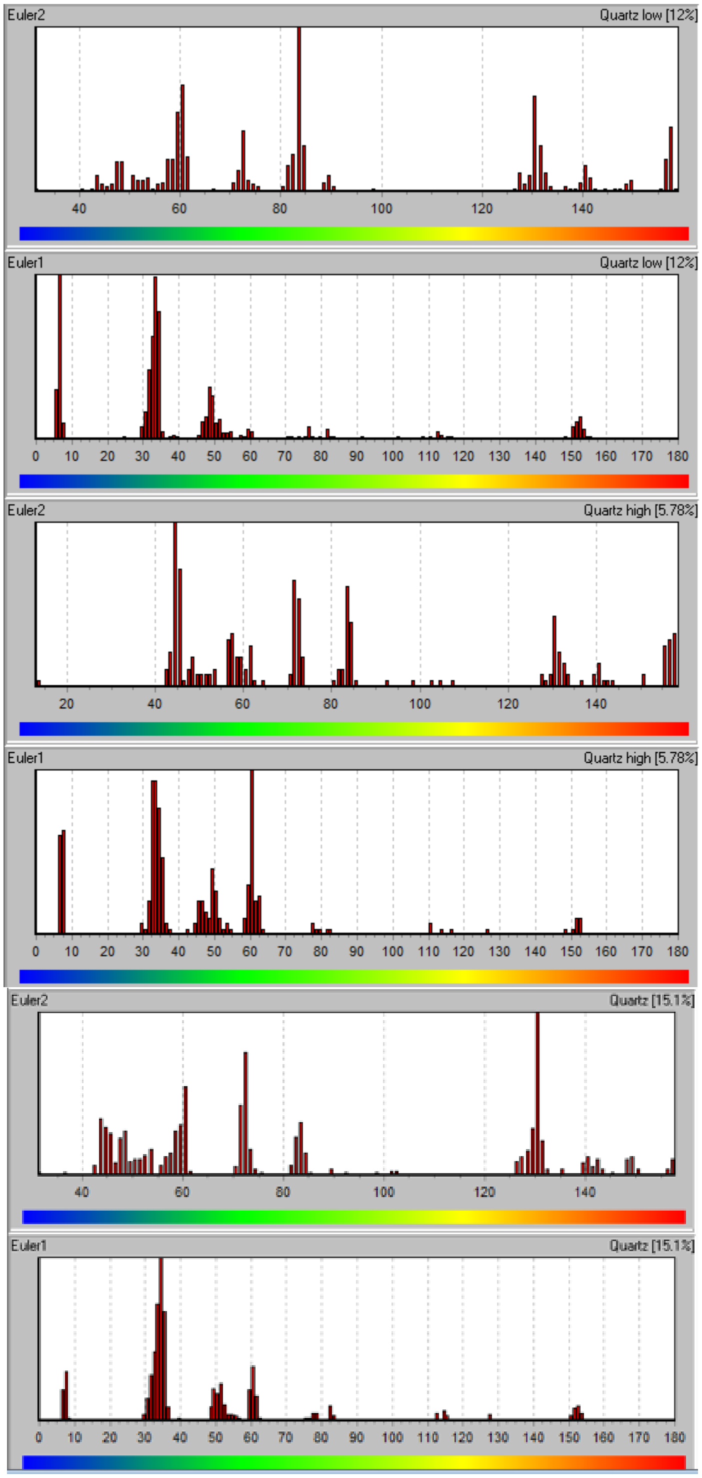

Figure C7: Histograms representing the $\emptyset$ and $\emptyset_1$ comparison for the third native sample. Correlations can be seen between the two Euler angles.

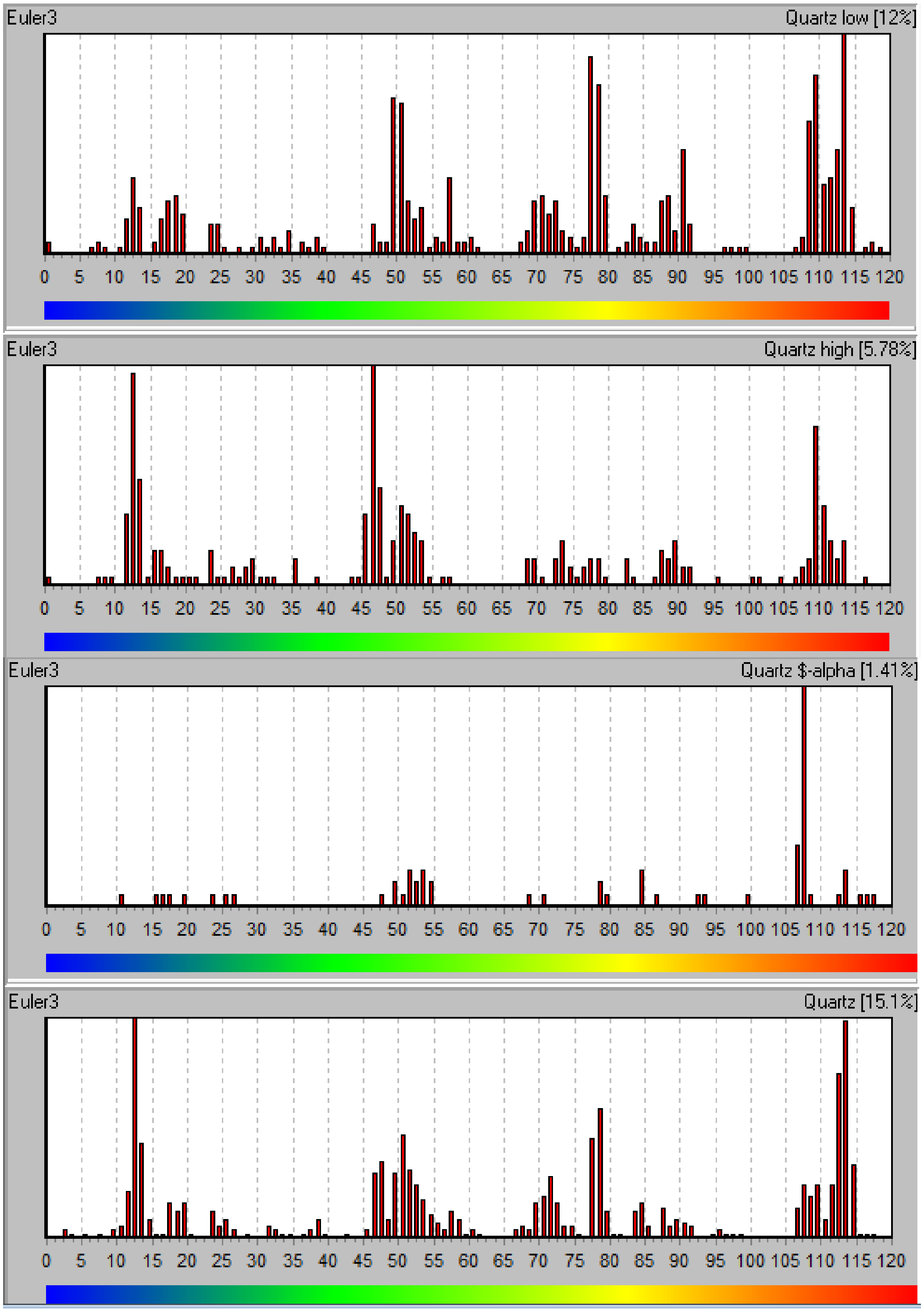

Figure C8: Histograms representing the rotations around the z-axis ($\emptyset_2$). Notice there are few 60° rotations prior to fracturing.

D3: Fracture Tip Sample

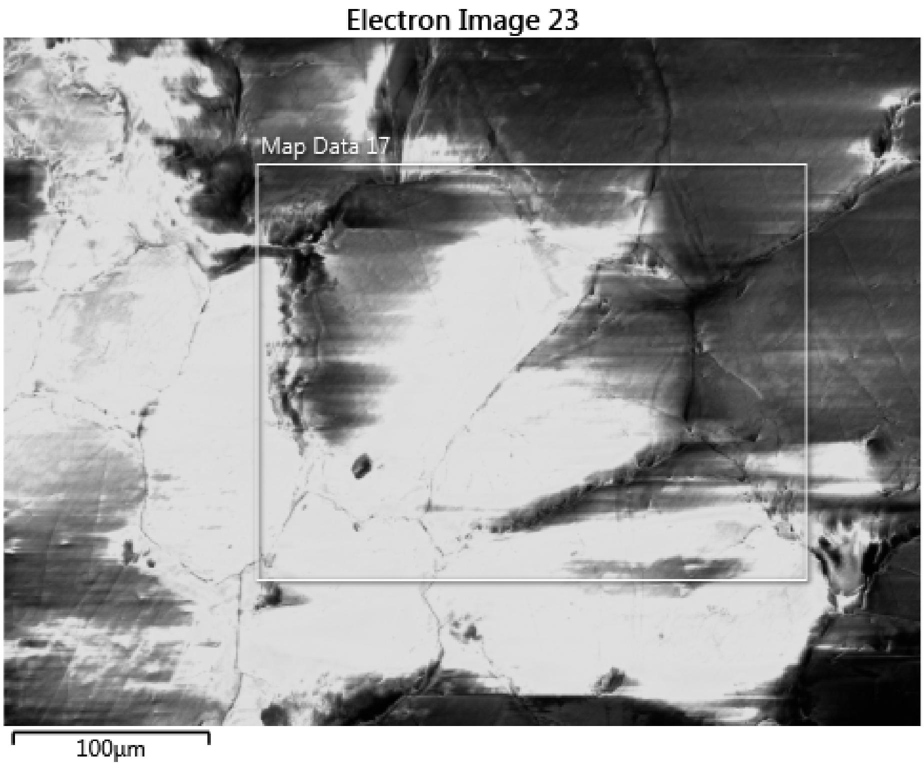

Figure C9: Area of study for a hydraulically fractured Tennessee sandstone sample. Analysis was taken 1.8 mm in front of the fracture tip, well within the plastic region.

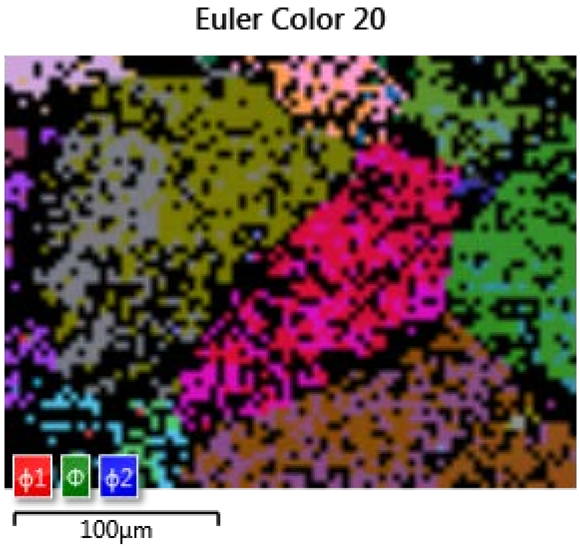

Figure C10: Complete Euler map showing the orientation of the crystals and the amount of data collected. Approximately 58% of diffraction patterns could be recognized.

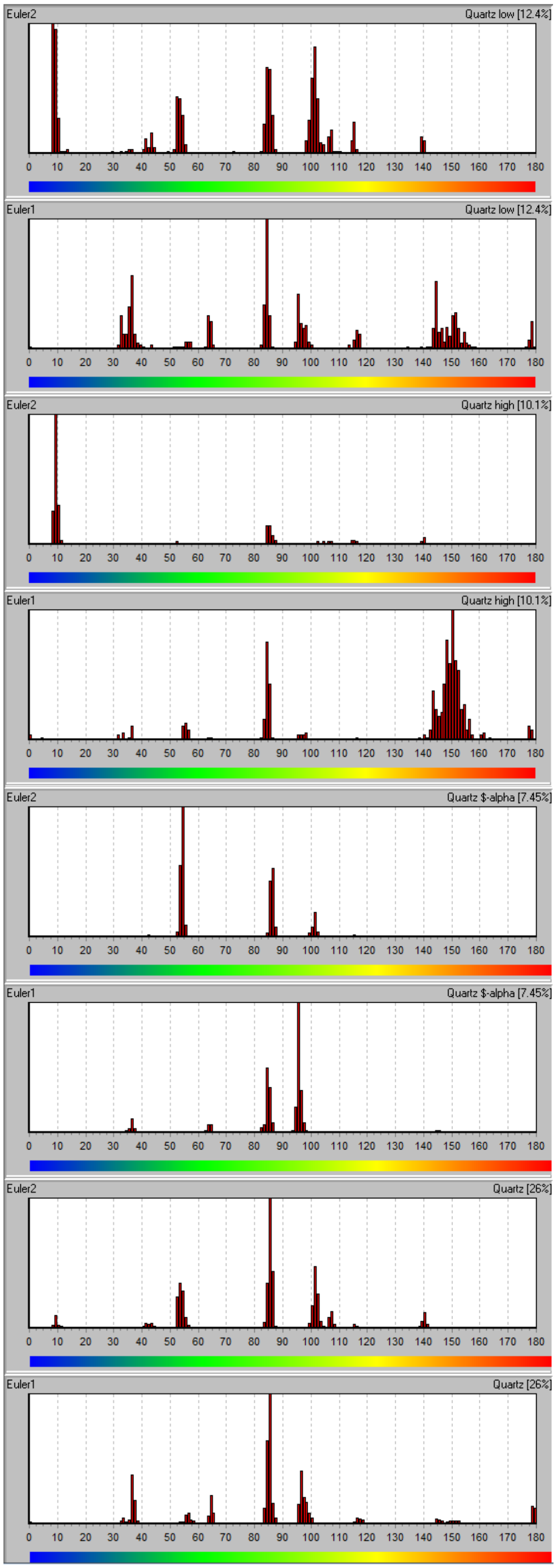

Figure C11: Histograms representing the $\emptyset$ and $\emptyset_1$ comparison for the fracture tip sample. A significant amount of correlation is found, satisfying condition 1.

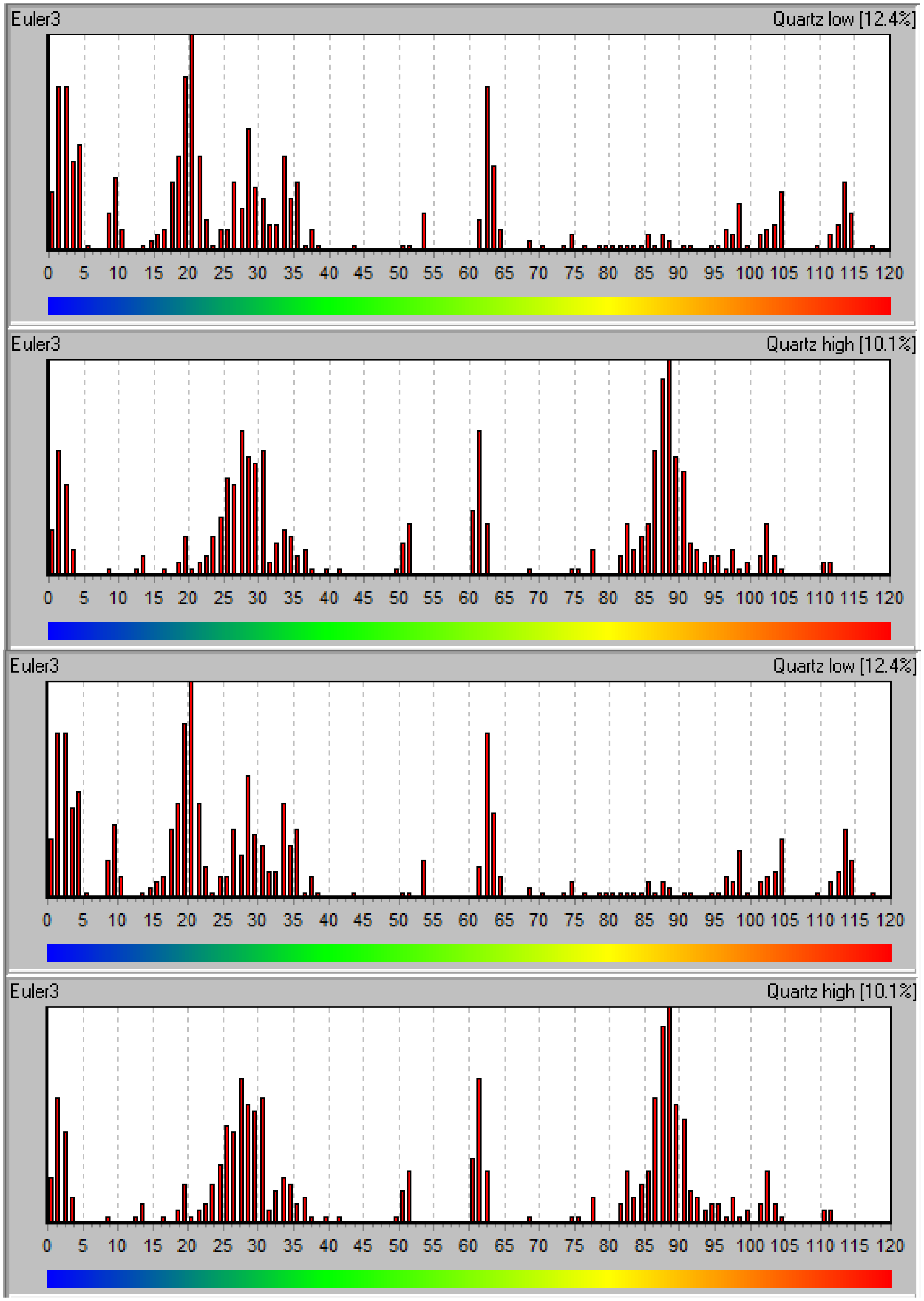

Figure C12: Histograms representing the rotations around the z-axis ($\emptyset_2$) for the fracture tip. Notice a spike in 60º rotations around the z-axis after fracturing. Significantly more 60º rotations are found at the fracture tip in comparison to the native samples, satisfying condition 2.